Spectral Energy Balance in Convective Boundary Layers

by

James Sandham

A thesis
presented to the University of Waterloo
in fulfillment of the
thesis requirement for the degree of
Master of Mathematics
in
Applied Mathematics

Waterloo, Ontario, Canada, 2014

Author's Declaration

I hereby declare that I am the sole author of this thesis. This is a true copy of the thesis, including any required final revisions, as accepted by my examiners.

I understand that my thesis may be made electronically available to the public.

Abstract

In his pioneering 1941 papers, Kolmogorov derived that the energy spectrum follows a universial form within a range of wavenumbers removed from both the forcing and dissipation and depending only on the wavenumber and the rate of dissipation. Analysis of the spectral kinetic energy budget can help explain the dynamics of the energy spectrum. Each term in this budget, representing nonlinear transfer, external forcing, and viscous dissipation, have been extensively studied in the idealised triply periodic case. In this thesis we apply these ideas to the study of convective boundary layer turbulence for both the dry and moist cases. To this end, the large-eddy simulation technique is employed to numerically integrate the anelastic Navier-Stokes equations. Each term in the spectral budget is computed and dependence on surface heating and water vapour flux, grid resolution, and domain size is investigated. It is found that the buoyancy term acts as a relatively large-scale forcing, i.e. horizontal scales of the boundary layer thickness. Energy at large-scales is then transfered to small scales by the nonlinear term where it is then removed through dissipation. This down-scale energy transfer is consistent with three-dimensional turbulence theory. It is also found however that the forcing term, while peaked at large-scales, actually extends all the way to the small scales. Also, despite increases in resolution, the transfer spectrum exhibited no range of constant spectral flux. Both of these results indicate that the convective boundary layer setup differs from the assumptions used in deriving the -5/3 inertial range scaling. Indeed, the kinetic energy spectrum itself did not exhibit an exact -5/3 scaling in the present study. Instead the spectrum was found to follow a shallower power law closer to -4/3, likely as a result of the broad spectrum of buoyancy flux.

Acknowledgements

I would like to thank my supervisor Dr. Michael Waite for his continual support and guidance throughout my thesis.

Dedication

To my family who has supported me throughout my academic career

Table of Contents

List of Tables

List of Figures

Chapter 1

Introduction and Background

"When I meet God, I am going to ask him two
questions: Why relativity? And why turbulence? I
really believe he will have an answer for the first."
— Werner Heisenberg

The atmosphere is divided up into a number of different layers: the troposphere occupying
the bottom 10-15 km, then the stratosphere ranging from 12-50 km, followed by the mesosphere,
thermosphere, and exosphere, which have approximate ranges 50-80 km, 80-500 km, 500-10000
km respectively [74]. We will only be concerned with a lower subset of the troposphere occu-
pying a region between the ground and 2-3 km where convective boundary layers form. In the
atmosphere, a convective boundary layer develops when heat flux dominates shear. Typically the
air is stably stratified in the morning, i.e. the potential temperature increases with height. The
Sun rises and begins to heat the ground, which causes hotter, less dense, air near the surface to
rise and mix with the overlying colder, denser air. It is precisely this mixing that expands the
boundary layer thickness through the process of entrainment. The boundary layer will continue
to expand until surface heating is turned off, i.e. when the Sun sets, at which point the boundary
layer will collapse [21, 67]. This evolution is shown graphically in Figure 1.1.

As shown in Figure 1.1, the convective boundary layer is typically divided into four regions:
the surface layer, mixing layer, entrainment zone, and the stable layer [67]. The first of these
regions, the surface layer, occupies only a few meters between the surface and the mixing layer.
Here, there is a fairly rapid temperature adjustment between the hotter surface potential tempera-
ture (from the heating via the Sun) and the cooler potential temperature found in the mixing layer.
The mixing layer, usually extending from just above the surface up to 0.5-2 km, is characterized

1
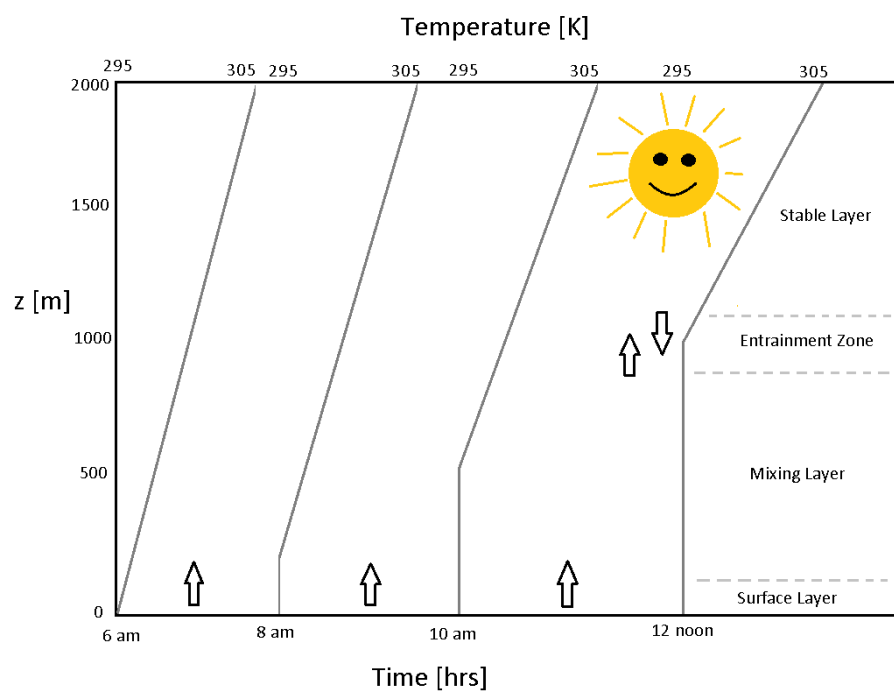
Figure 1.1: A typical dry convective boundary layer evolution through the day following [67].

by strong thermal plumes and eddies ranging in size from under one meter up to the mixing layer thickness. Because of the large amount of mixing that occurs within this layer, the potential temperature is much more homogeneous and on average constant with vertical height. Above the mixing layer the atmosphere is again stably stratified and hence is referred to as the stable layer, which extends through the rest of the troposphere. The interface between the mixing layer and the stable layer is called the entrainment zone and it is here where overlying air is pulled (or entrained) into the mixing layer causing the continual growth of the mixing layer depth [67].

In trying to model this convective boundary layer, we need an equation that advances the three velocities (u, v, and w) and additional equations for the pressure, temperature, and density, which are the relevant quantities in a dry atmospheric simulation. The velocities are described by the Navier-Stokes equations. Additional equations of state, continuity, and energy conservation, link the three variable of pressure, temperature, and density with momentum. Moisture will be represented by the mixing ratio (ratio of the density of liquid water and water vapour to dry air) and follows a similar equation as temperature along with terms to account for changes of state. Ideally this set of equations would be solved such that all scales are resolved fully, however as is well known for three dimensional fluid simulations, this would require computational resources in excess of what is currently available. Thus we will employ a numerical technique called Large-eddy Simulation (LES) that resolves the large-scale energy containing eddies, while only parameterizing the effect of the unresolved small scales on the larger scales.

This thesis is structured as follows. The equations of motion, background on large eddy simulation, and additional topics on how the momentum fluxes are parameterized at the surface, how cloud formation is handled, and an overview of turbulence theory, are covered in the chapter Introduction and Background. In the Methodology chapter we provide details on the code used as well as the dry and moist model setups. In the Results chapter we present our findings in computing the spectral kinetic energy budget for both dry and moist convective boundary layers, which for the dry experiments have been submitted for publication in the Journal of Turbulence [63]. Finally we summarize our results in the Conclusions chapter.

1.1 Equations of Motion

1.1.1 Boussinesq Approximation

Consider the incompressible Navier-Stokes equations [40]:

$$\rho(\frac{\partial u_i}{\partial t} + u_j \frac{\partial u_i}{\partial x_j}) = -\frac{\partial p}{\partial x_i} + \rho g \delta_{i3} + \mu \frac{\partial^2 u_i}{\partial x_j{}^2}.$$

3

Let us decompose the density into a constant background state and a perturbation and similarly decompose pressure into a basic state dependent on height and a perturbation, i.e. let $\rho = \rho_0 + \rho'$ and $p = p_0(z) + p'$. Substituting this into the momentum equation, dividing through by ρ_0, and making the assumption that the background flow is in hydrostatic balance, i.e. $\partial p/\partial z = \rho_0 g$, results in [40]:

$$(1 + \frac{\rho'}{\rho_0})(\frac{\partial u_i}{\partial t} + u_j \frac{\partial u_i}{\partial x_j}) = -\frac{1}{\rho_0}\frac{\partial p'}{\partial x_i} + \frac{\rho'}{\rho_0}g\delta_{i3} + \nu\frac{\partial^2 u_i}{\partial x_j{}^2}.$$

If we assume $\rho'/\rho_0 \ll 1$ then $(1 + \rho'/\rho_0) \approx 1$. The buoyancy term however is very important in causing vertical accelerations and so is retained. In the above incompressible equations we implicitly assumed $(1/\rho)D\rho/Dt$ is small which thus replaces the continuity equation [40]:

$$D\rho/Dt + \rho\frac{\partial u_i}{\partial x_i} = 0,$$

with

$$\frac{\partial u_i}{\partial x_i} = 0.$$

This assumption is valid when the flow speeds are much less than the Mach number, and when the vertical variation in density is not too large [40]. In the atmosphere this is appropriate for heights less than 10 km. Finally we prescribe a temperature equation [40]:

$$\frac{\partial T}{\partial t} + u_j\frac{\partial T}{\partial x_j} = \kappa\frac{\partial^2 T}{\partial x_j{}^2}.$$

Thus we arrive at the complete set of equations for the Boussinesq approximation [40]:

$$(\frac{\partial u_i}{\partial t} + u_j\frac{\partial u_i}{\partial x_j}) = -\frac{1}{\rho_0}\frac{\partial p'}{\partial x_i} + \frac{\rho'}{\rho_0}g\delta_{i3} + \nu\frac{\partial^2 u_i}{\partial x_j{}^2},$$

$$\frac{\partial u_i}{\partial x_i} = 0,$$

$$\frac{\partial T}{\partial t} + u_j\frac{\partial T}{\partial x_j} = \kappa\frac{\partial^2 T}{\partial x_j{}^2},$$

$$\rho' = -\alpha\rho_0(T - T_0),$$

which assumes a linear equation of state.

4

1.1.2 Anelastic Approximation

The Boussinesq approximation outlined above is actually a simplification of the anelastic approximation, which accounts for some compressibility in the vertical and thus relaxes some of the height restriction that exists in the Boussinesq approximation and is a more accurate approximation for atmospheric flows [55, 71, 20]. The derivation for the anelastic momentum equation follows that of the Boussinesq approximation where we again assume $\rho'/\rho_0 \ll 1$. Important differences may exist however in the continuity equation. With this in mind, let us perform a scale analysis with a vertically dependent reference density. Writing out the continuity equation with the $\rho = \rho_0(z) + \rho'$ substitution and with horizontal and vertical derivatives written out explicitly results in [59]:

$$\frac{\partial \rho'}{\partial t} + \rho_0 (\frac{\partial u}{\partial x} + \frac{\partial v}{\partial y}) + \rho_0 \frac{\partial w}{\partial z} + (u \frac{\partial \rho'}{\partial x} + v \frac{\partial \rho'}{\partial y}) + w \frac{\partial \rho'}{\partial z} + w \frac{\partial \rho_0}{\partial z} = 0. \tag{1.1}$$

Now define L_H to be a horizontal length scale and L_V to be a vertical length scale. Also define

$$L_\rho = \left| \frac{1}{\rho_0} \frac{\partial \rho_0}{\partial z} \right|^{-1},$$

which is about 10 km in the atmosphere [59]. Comparing the first term in the above continuity equation (1.1) with $\rho_0 \partial w/\partial z$ tells us [59]:

$$\frac{\frac{\partial \rho'}{\partial t}}{\rho_0 \frac{\partial w}{\partial z}} \sim \frac{\rho'}{\rho_0} \ll 1.$$

Here we have assumed an advective time scale $T \sim W/L_z$. From [7] an additional condition on the flow is that

$$\frac{n^2 L_z^2}{c^2} \ll 1,$$

where n is the dominant frequency of the flow and c is the speed of sound (in air for the atmosphere). This condition comes from the fact that for compressible flows:

$$\left| \frac{1}{\rho c^2} \frac{\partial p}{\partial t} \right| << \frac{W}{L_z},$$

5

where W and L_z are typical velocity and length scales of the flow [7]. Again assuming that the advective time scale is representative of n^{-1}, then this reduces to the Mach number condition [7]:

$$\frac{W^2}{c^2} \ll 1,$$

which in the case of convective boundary layers is clearly satisfied as $W \sim 1$ m/s while $c \sim 340$ m/s [7]. Comparing the remaining terms (1.1) with $\rho_0 \partial w / \partial z$ gives:

$$\frac{u \frac{\partial \rho'}{\partial x} + v \frac{\partial \rho'}{\partial y}}{\rho_0 \frac{\partial w}{\partial z}} \sim \frac{L_V}{L_H} \frac{\rho'}{\rho_0} \ll 1 \quad \text{provided} \quad \frac{L_V}{L_H} \leq 1,$$

$$\frac{w \frac{\partial \rho'}{\partial z}}{\rho_0 \frac{\partial w}{\partial z}} \sim \frac{\rho'}{\rho_0} \ll 1,$$

$$\frac{w \frac{\partial \rho_0}{\partial z}}{\rho_0 \frac{\partial w}{\partial z}} \sim \frac{L_V}{L_\rho}.$$

It is clear from this last term that in situations where $L_V/L_\rho \sim 1$ the vertical dependence of the density will become important [59]. In these situations we must retain the vertical dependence on the density which then results in a slightly more complicated version of the continuity equation from what was seen in the Boussinesq approximation. The momentum and continuity equation (1.1) are now [59]:

$$\left(\frac{\partial u_i}{\partial t} + u_j \frac{\partial u_i}{\partial x_j}\right) = -\frac{1}{\rho_0} \frac{\partial p'}{\partial x_i} + \frac{\rho'}{\rho_0} g \delta_{i3} + \nu \frac{\partial^2 u_i}{\partial x_j^2},$$

$$\frac{\partial}{\partial x_i}(\rho_0 u_i) = 0. \tag{1.2}$$

The Boussinesq energy equation is not valid over significant depths of the atmosphere. Instead, atmospheric scientists often use a different quantity called the potential temperature which we define as [61]:

$$\theta = T\left(\frac{p_0}{p}\right)^{\frac{R}{c_p}}. \tag{1.3}$$

6

We can say that the potential temperature is the temperature a parcel of fluid would have if adiabatically (i.e. no heat exchange with its surroundings) brought to a reference pressure. If we take the logarithm of (1.3) and use the ideal gas law, $p = \rho R T$, we get [71]:

$$\log(\theta) = \frac{1}{\gamma}\log(p) - \log(\rho) + \text{constant}, \tag{1.4}$$

where $\gamma = c_p/c_v$. Calculating the differential of (1.4) (we assume here that these differentials are representative of the perturbations of their respective functions, i.e. $d\theta \approx \theta'$) and finding the derivative with respect to z, we get [71]:

$$\frac{1}{\theta_0}\theta' = \frac{1}{\gamma}\frac{p'}{p} - \frac{\rho'}{\rho} \approx \frac{1}{\gamma}\frac{p'}{p_0} - \frac{\rho'}{\rho_0} \quad \text{and} \quad \frac{d}{dz}\log\theta_0 = -\frac{g}{\gamma}\frac{\rho_0}{p_0} - \frac{1}{\rho_0}\frac{d\rho_0}{dz}. \tag{1.5}$$

We can re-write the momentum equation in (1.2) [71],

$$\frac{\partial u_i}{\partial t} + u_j\frac{\partial u_i}{\partial x_j} = -\frac{\partial}{\partial x_i}\left(\frac{p'}{\rho_0}\right) - \frac{p'}{\rho_0^2}\frac{\partial\rho_0}{\partial z}\delta_{i3} - \frac{\rho'}{\rho_o}g\delta_{i3} + \nu\frac{\partial^2 u_i}{\partial x_j^2}.$$

Now using (1.5) [71],

$$\frac{\partial u_i}{\partial t} + u_j\frac{\partial u_i}{\partial x_j} = -\frac{\partial}{\partial x_i}\left(\frac{p'}{\rho_0}\right) - \frac{p'}{\rho_0^2}\frac{\partial\rho_0}{\partial z}\delta_{i3} - \frac{g}{\gamma}\frac{p'}{p_0}\delta_{i3} + \frac{\theta'}{\theta_o}g\delta_{i3} + \nu\frac{\partial^2 u_i}{\partial x_j^2},$$

$$= -\frac{\partial}{\partial x_i}\left(\frac{p'}{\rho_0}\right) + \frac{p'}{\rho_0}\frac{d}{dz}(\log\theta_0)\delta_{i3} + \frac{\theta'}{\theta_o}g\delta_{i3} + \nu\frac{\partial^2 u_i}{\partial x_j^2},$$

$$= -\frac{\partial}{\partial x_i}\left(\frac{p'}{\rho_0}\right) + \frac{p'}{\rho_0}\left(\frac{1}{\theta_0}\frac{d\theta_0}{dz}\right)\delta_{i3} + \frac{\theta'}{\theta_o}g\delta_{i3} + \nu\frac{\partial^2 u_i}{\partial x_j^2}.$$

Consider the first two terms on the rhs of the above equation. We expect p'/ρ_0 to be small, however, $-\partial/\partial x_i(p'/\rho_0)$ may be quite large as p' is a perturbation and may have large derivatives despite being small in magnitude itself. The $(1/\theta_0)d\theta_0/dz$ is small as we do not expect the potential temperature to change by a large amount over a vertical height of a couple kilometers. For example typical values of θ_0 would be around 300 K and might change by at most 10 K over 2000 m which would give this term a magnitude of around 6×10^{-4}. Compare this to the

7

buoyancy term which might have a magnitude around $O(1 \text{ m/s}^2)$. In fact while the density may change by around 20% over 2 km, the temperature will only change by around 2%. Therefore with this in mind we retain the z dependence in $\rho_0(z)$ while approximating θ_0 as a constant, Θ_0. Thus we may neglect the second term from the equations and we are therefore left with [71, 20]:

$$\frac{\partial u_i}{\partial t} + u_j \frac{\partial u_i}{\partial x_j} = -\frac{\partial}{\partial x_i}(\frac{p'}{\rho_0}) + \frac{\theta'}{\theta_o}g\delta_{i3} + \nu \frac{\partial^2 u_i}{\partial x_j^2}. \tag{1.6}$$

It is common to rewrite the pressure in terms of the Exner (or dynamic pressure) function [71, 20],

$$\pi = (\frac{p}{p_{00}})^{\frac{R}{c_p}}.$$

From this we see that [71, 20]:

$$\begin{aligned}
c_p\theta\frac{\partial \pi}{\partial x_i} &= c_p\theta(\frac{R}{c_p}(\frac{p}{p_{00}})^{\frac{R}{c_p}-1}\frac{1}{p_{00}}\frac{\partial p}{\partial x_i}) \\
&= \frac{TR}{p_{00}}(\frac{p}{p_{00}})^{-1}\frac{\partial p}{\partial x_i} \\
&= \frac{TR\rho}{p}\frac{1}{\rho}\frac{\partial p}{\partial x_i} \\
&= \frac{1}{\rho}\frac{\partial p}{\partial x_i}, \quad \text{where we have used the ideal gas law } p = \rho RT.
\end{aligned}$$

Substituting in $p = p_0 + p'$, $\pi = \pi_0 + \pi'$, and $\theta = \Theta_0 + \theta'$, into the above equation we get the approximation [71, 20]:

$$\frac{p'}{p_0} = c_p\Theta_0\pi'.$$

Putting this into 1.6 we arrive at the momentum equation written in terms of potential temperature and the pressure Exner function [71, 20]:

$$\frac{\partial u_i}{\partial t} + u_j \frac{\partial u_i}{\partial x_j} = -c_p\Theta_0\frac{\partial \pi'}{\partial x_i} + \frac{\theta'}{\Theta_o}g\delta_{i3} + \nu \frac{\partial^2 u_i}{\partial x_j^2}. \tag{1.7}$$

Above we derived the anelastic Navier-Stokes momentum equation. Here we look at the corresponding equation for scalar advection, for example for potential temperature. We clearly need such an equation since potential temperature appears in the above momentum equation and we need to know how it is advected and changed by the flow. Depending on the complexity of our model we could include such scalars as liquid water potential temperature θ_l and total water mixing ratio q_t, however for the purpose of simplicity we only derive the scalar equation for potential temperature as the scalar equations have the same form regardless. We begin with the conservation of heat energy (first law of thermodynamics) [7, 71]:

$$\rho c_p \frac{DT}{Dt} - \alpha T \frac{Dp}{Dt} = 0,$$

where c_p is the specific heat. We note that the dimensions of $[c_p] \sim J/$ kg Kelvin and so the quantity $[\rho c_p T] \sim J/m^3$ is the thermal energy per unit mass. Also the coefficient of thermal expansion, α, is given by [7]:

$$\begin{aligned}
\alpha &= -\frac{1}{\rho}(\frac{\partial \rho}{\partial T})_p, \\
&= \frac{1}{\rho}(\frac{\rho}{T})_p, \\
&= \frac{1}{T}, \qquad \text{using ideal gas law.}
\end{aligned}$$

We are then left with:

$$\rho c_p \frac{DT}{Dt} - \frac{Dp}{Dt} = 0.$$

We want an equation for potential temperature θ, not temperature T, and so we plug in our previously defined potential temperature to get the following [71]:

$$\rho c_p \frac{D\theta}{Dt}\left(\frac{p}{p_0}\right)^{\frac{R}{c_p}} + \rho c_p \theta \frac{R}{c_p}\left(\frac{p}{p_0}\right)^{\frac{R}{c_p}-1}\frac{1}{p_0}\frac{Dp}{Dt} - \frac{Dp}{Dt} = 0,$$

$$\rho c_p \frac{D\theta}{Dt} + \rho\theta R\frac{1}{p}\frac{Dp}{Dt} - \left(\frac{p_0}{p}\right)^R c_p \frac{Dp}{Dt} = 0,$$

$$\rho c_p \frac{D\theta}{Dt} + \frac{\theta}{T}\frac{Dp}{Dt} - \frac{\theta}{T}\frac{Dp}{Dt} = 0,$$

$$\rho\frac{D\theta}{Dt} = 0.$$

Now by introducing $\rho = \rho_0 + \rho'$ and $\theta = \Theta_0 + \theta'$ as before and dividing by ρ_0 we can approximate the above equation as:

$$\frac{\partial\theta'}{\partial t} = -u_i\frac{\partial\theta'}{\partial x_i}. \tag{1.8}$$

There are two terms left to add to this equation: subsidence and radiative cooling. Subsidence occurs when cooler, denser air from above sinks. As this happens adiabatic warming occurs. All this sinking air results in high pressures and diverging winds and appears as a linear advection term in the potential temperature equation [67].

$$\frac{\partial\theta'}{\partial t} = -w_s\frac{\partial\theta'}{\partial z}. \tag{1.9}$$

Radiative cooling occurs when the atmosphere loses heat from thermal radiation. This is accounted for in the potential temperature equation as [67]:

$$\frac{\partial\theta'}{\partial t} = -Q. \tag{1.10}$$

Combining (1.8), (1.9), and (1.10):

$$\frac{\partial\theta'}{\partial t} = -u_i\frac{\partial\theta'}{\partial x_i} + \frac{\partial F_\theta}{\partial x_i}\delta_{i3} - w_s\frac{\partial\theta'}{\partial z}.$$

1.2 Large-eddy Simulation

We would ideally solve the anelastic Navier-Stokes equations using direct numerical simulation (DNS), which means using sufficient resolution to resolve all scales of motion down to the molecular dissipation scale [57], limited computational resources prevents this method from being a viable option for all but the most restrictive domain sizes. For example, in the atmosphere molecular viscosity acts at scales of $O(1)$ mm which on even a modest $5 \times 5 \times 2$ km domain would require 5 million points in both horizontal directions and 2 million points in the vertical! Currently on the fastest supercomputers, simulations of around 4096^3-8192^3, i.e. [35, 12], have been performed meaning that DNS of even a relatively small section of the atmosphere will be impossible for some time. In fact we can illuminate the problem even more explicitly by considering the number of grid points that would be required to resolve a fluid flow in terms of Reynolds number. A reasonable criteria for sufficient resolution is $k_{max}\eta \approx 1$, where $k_{max} = \pi/\Delta x$ is the maximum wavenumber and η is the dissipation length scale [57]. For a domain size of L and $\Delta x = N/L$,

$$\frac{\pi\eta}{\Delta x} \approx 1 \Rightarrow N \approx \frac{L}{\pi\eta} \Rightarrow N \approx \frac{1}{\pi}Re^{\frac{3}{4}},$$

where we have used $\eta = (\mu^3/\varepsilon)^{1/4}$ and $\varepsilon \approx U^3/L$ (ε is the rate of dissipation of kinetic energy) [43, 11]. Given the high Reynolds numbers found in atmospheric flows, this gives us a prohibitive increase in the number of grid points needed for DNS. An alternative is to perform a large-eddy simulation (LES), in which large-scale turbulent eddies are resolved but small scales eddies are parameterized [57, 3]. An overview of LES is presented in the following pages.

The central idea of LES is to separate the flow variables into resolved and unresolved parts through the action of a spatial filter. Specifically, we define $u_i = \bar{u}_i + u_i^r$ where $(^-)$ indicates a filtered field and (r) is a residual field [1], sometimes called a sub-grid field. The filtering is defined by [57]:

$$\bar{u}_i(\mathbf{x}) = \iiint G(\mathbf{x} - \mathbf{x}^r)u_i(\mathbf{x}^r)d\mathbf{x}^r,$$

where G is a spatial filter. If we take the Fourier transform of the filtered velocities $\bar{u}_i$ and use the convolution theorem we get [57]:

---

[1] Often the residual fields will be represented with a prime notation, i.e. u', however we are already using primes to denote perturbations about a basic state
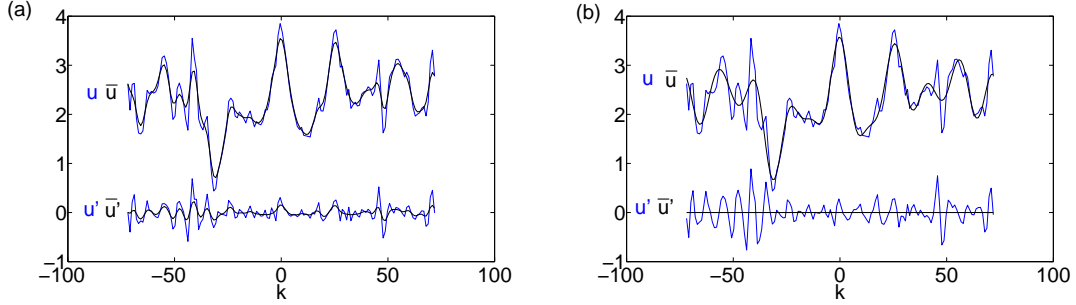
Figure 1.2: Total velocity, filtered velocity, sub-grid velocity, and filtered sub-grid velocity for (a) Gaussian filter and (b) sharp filter following [57]. In the case of the sharp filter all motions smaller than the cut-off wavenumber $k_c = \pi/\Delta$, i.e. the residual motions, are removed by the filter.

$$\hat{\bar{u}}_i(k) = \hat{G}(k)\hat{u}_i(k).$$

As can be seen, the filter G essentially removes the effects of the residual motions from the total field. In choosing a filter we require that $\hat{G}(0) = 1$ and that $\hat{G}$ be symmetric about $k = 0$ [57]. The most common choices of filter function are [57]:

$$\text{Sharp:} \quad \hat{G}(k) = H(k_c - |k|) \quad \text{where } k_c = \frac{\pi}{\Delta},$$

$$\text{Box:} \quad \hat{G}(k) = \frac{\sin(\frac{1}{2}k\Delta)}{\frac{1}{2}k\Delta},$$

$$\text{Gaussian:} \quad \hat{G}(k) = e^{-\frac{k^2\Delta^2}{24}}.$$

An important property of the sharp cut-off filter is that the filtered residual motions are zero, i.e. $\overline{u^r} = 0$. This is not true of all filters as is shown in 1.2, which plots the Gaussian and sharp filters applied to the total velocity, u, and the residual velocity, u^r. In the case of the sharp filter the residual motions are all smaller than the cut-off, $k_c = \pi/\Delta$, and are thus removed by the filter. On the other hand the Gaussian filter influences all scales and so the filtered residual field is not zero. Applying the sharp filter to the anelastic Navier-Stokes equations results in:

12

$$\frac{\partial \bar{u}_i}{\partial t} + \frac{1}{\rho_0}\frac{\partial}{\partial x_j}(\rho_0 \overline{u_i u_j}) = -c_p \Theta_0 \frac{\partial \bar{\pi}'}{\partial x_i} + \frac{\bar{\theta}'}{\Theta_0} g \delta_{i3} + \nu \frac{\partial^2 \bar{u}_i}{\partial x_j{}^2},$$

$$\frac{\partial}{\partial x_i}(\rho_0 \bar{u}_i) = 0,$$

$$\frac{\partial \bar{\theta}'}{\partial t} + \frac{1}{\rho_0}\frac{\partial}{\partial x_j}(\rho_0 \overline{u_j \theta'}) = \frac{\partial \bar{F}_\theta}{\partial x_i}\delta_{i3} - w_s \frac{\partial \bar{\theta}'}{\partial z}.$$

Now, we define [57]:

$$\bar{\tau}_{ij} = \overline{u_i u_j} - \bar{u}_i \bar{u}_j \quad \text{and} \quad \bar{\gamma}_{\theta j} = \overline{\theta u_j} - \bar{\theta}\bar{u}_j.$$

Because we are modelling the atmosphere within the O(10 km) range, with grid sizes O(10 m) and thus much larger than the dissipation range where molecular diffusion dominates, we do not need to include the effect of molecular viscosity. Instead all effects smaller then our grid size will be modelled. The updated filtered equations then become:

$$\frac{\partial \bar{u}_i}{\partial t} = -\bar{u}_j \frac{\partial \bar{u}_i}{\partial x_j} - c_p \Theta_0 \frac{\partial \bar{\pi}'}{\partial x_i} + \frac{\bar{\theta}'}{\Theta_0} g \delta_{i3} + \frac{1}{\rho_o}\frac{\partial(\rho_o \bar{\tau}_{ij})}{\partial x_j},$$

$$\frac{\partial(\rho_o \bar{u}_i)}{\partial x_i} = 0, \tag{1.11}$$

$$\frac{\partial \bar{\theta}'}{\partial t} = -\bar{u}_j \frac{\partial \bar{\theta}'}{\partial x_j} + \frac{1}{\rho_0}\frac{\partial(\rho_0 \bar{\gamma}_{\theta j})}{\partial x_j} + \frac{\partial \bar{F}_\theta}{\partial x_j}\delta_{j3} - w_s \frac{\partial \theta'}{\partial z}.$$

It is clear that the above equations are not closed. Instead we must model $\bar{\tau}_{ij}$ and $\bar{\gamma}_{\theta j}$ in terms of the filtered fields $\bar{u}$, $\bar{v}$, $\bar{w}$, and $\bar{\theta}'$. The most popular and simplest choice is to use an eddy-viscosity model [43, 57].

$$\bar{\tau}_{ij} = -2K_m S_{ij} \quad \text{and} \quad \bar{\gamma}_{\theta j} = -\frac{K_m}{Pr}\frac{\partial \bar{\theta}'}{\partial x_j},$$

where Pr is the Prandtl number and K_m is the eddy viscosity and where different choices of K_m define different LES eddy-viscosity models.

1.2.1 Smagorinsky-Lilly model

One of the simplest models for the eddy-viscosity is the Smagorinsky-Lilly model [45, 65, 46]:

$$K_m = (C_s l)^2 S \sqrt{1 - \frac{Ri}{Pr}},$$

where the resolved rate of strain tensor, S_{ij}, is defined by [57]:

$$S_{ij} = \frac{1}{2}\left(\frac{\partial \bar{u}_i}{\partial x_j} + \frac{\partial \bar{u}_j}{\partial x_i}\right).$$

The calculation of the Richardson number, Ri, is given by [46]:

$$Ri = \frac{N^2}{S^2} \quad \text{where} \quad N^2 = \frac{g}{\Theta_0}\frac{\partial \bar{\theta}'}{\partial z},$$

and S^2 is defined as [57]:

$$S^2 = 2S_{ij}S_{ij}.$$

This model is a modification of the original Smagorinsky eddy viscosity parameterization in that the added square root term ensures that when the atmosphere is stably stratified the eddy viscosity goes to zero, which is what we want. The eddy viscosity, K_m, is chosen so that it has the correct dimensions of viscosity, i.e. L^2/L, and $C_s l$ is the mixing length. With this model for the sub-grid fluxes $\bar{\tau}_{ij}$ and $\bar{\gamma}_{ij}$, our equations are now closed and a solution can be found in terms of the filtered variables. In particular no explicit choice of filter G is required in the above equations and so we say that this filter is only conceptually applied [57].

1.2.2 Turbulent Kinetic Energy model

In the turbulent kinetic energy (TKE) model [17, 56, 3], the sub-grid fluxes are parameterized by solving a prognostic equation for the unresolved TKE, which itself is parameterized using the resolved velocities. As a result the TKE model is often referred to as a 1.5 order closure model. Here we choose [17, 21, 56]

$$K_m = c_m l \sqrt{e} \quad \text{and} \quad K_h = c_h l \sqrt{e}, \tag{1.12}$$

where $e = \overline{u_i^r u_i^r}/2$ is the turbulent kinetic energy [17, 21], i.e. the kinetic energy of the unresolved turbulence. Notice that this gives the correct dimensions for K_m. To close the system we need to formulate an equation for e. To do this let us first recall the total field momentum equation and the filtered momentum equation:

$$\frac{\partial u_i}{\partial t} + \frac{1}{\rho_0}\frac{\partial}{\partial x_j}(\rho_0 u_i u_j) = -c_p\Theta_0\frac{\partial \pi'}{\partial x_i} + \frac{g}{\Theta_0}\theta'\delta_{i3} + \nu\frac{\partial^2 u_i}{\partial x_j{}^2}, \tag{1.13}$$

and,

$$\frac{\partial \bar{u}_i}{\partial t} + \frac{1}{\rho_0}\frac{\partial}{\partial x_j}(\rho_0 \bar{u}_i \bar{u}_j) = -c_p\Theta_0\frac{\partial \bar{\pi}'}{\partial x_i} + \frac{\bar{\theta}'}{\theta_o}g\delta_{i3} + \nu\frac{\partial^2 \bar{u}_i}{\partial x_j{}^2} - \frac{1}{\rho_o}\frac{\partial(\rho_o\overline{u_i^r u_j^r})}{\partial x_j}. \tag{1.14}$$

Now subtracting 1.13 − 1.14 and then multiplying by u_i^r results in [21, 3]:

$$\frac{\partial}{\partial t}\left(\frac{1}{2}\overline{u_i^r u_i^r}\right) = -\frac{1}{\rho_0}\overline{u_i^r\frac{\partial}{\partial x_j}(\rho_0(u_i u_j - \bar{u}_i\bar{u}_j - u_i^r u_j^r))} - c_p\Theta\frac{\partial}{\partial x_i}(\overline{\pi''u_i^r}) + \frac{g}{\Theta}\overline{u_i^r\theta''}\delta_{i3} + \overline{\nu u_i^r\frac{\partial^2 u_i^r}{\partial x_j{}^2}},$$

$$= \frac{1}{\rho_0}\overline{u_i^r\frac{\partial}{\partial x_j}(\rho_0(\bar{u}_i u_j^r + u_i^r\bar{u}_j))} - c_p\Theta\frac{\partial}{\partial x_i}(\overline{\pi''u_i^r}) + \frac{g}{\Theta}\overline{u_i^r\theta''}\delta_{i3} + \frac{\partial}{\partial x_j}(\nu\frac{\partial}{\partial x_j}\frac{1}{2}\overline{u_i^r u_i^r}) - \nu\overline{\frac{\partial u_i^r}{\partial x_j}}^2,$$

$$= -\frac{1}{\rho_0}\frac{\partial}{\partial x_j}(\rho_0\bar{u}_j\frac{1}{2}\overline{u_i^r u_i^r}) + \frac{\partial}{\partial x_j}(\frac{1}{2}\overline{u_j^r u_i^r u_i^r}) - \overline{u_j^r u_i^r}\frac{\partial \bar{u}_i}{\partial x_j} - c_p\Theta\frac{\partial}{\partial x_i}(\overline{\pi''u_i^r}) + \frac{g}{\Theta}\overline{u_i^r\theta''}\delta_{i3}$$

$$+ \frac{\partial}{\partial x_j}(\nu\frac{\partial}{\partial x_j}\frac{1}{2}\overline{u_i^r u_i^r}) - \nu\overline{\frac{\partial u_i^r}{\partial x_j}}^2,$$

$$= -\frac{1}{\rho_0}\frac{\partial}{\partial x_j}(\rho_0\bar{u}_j e) + \frac{\partial}{\partial x_j}(\frac{1}{2}\overline{u_j^r u_i^r u_i^r}) - \overline{u_j^r u_i^r}\frac{\partial \bar{u}_i}{\partial x_j} - c_p\Theta\frac{\partial}{\partial x_i}(\overline{\pi''u_i^r}) + \frac{g}{\Theta}\overline{u_i^r\theta''}\delta_{i3}$$

$$+ \frac{\partial}{\partial x_j}(\nu\frac{\partial}{\partial x_j}\frac{1}{2}\overline{u_i^r u_i^r}) - \nu\overline{\frac{\partial u_i^r}{\partial x_j}}^2,$$

$$\frac{\partial e}{\partial t} = -\frac{1}{\rho_0}\frac{\partial}{\partial x_j}(\rho_0\bar{u}_j e) + \frac{\partial}{\partial x_i}(\overline{u_i^r e} - c_p\Theta\overline{\pi''u_i^r} + \nu\frac{\partial e}{\partial x_j}) - \overline{u_j^r u_i^r}\frac{\partial \bar{u}_i}{\partial x_j} + \frac{g}{\Theta}\overline{u_i^r\theta''}\delta_{i3} - \nu\overline{\frac{\partial u_i^r}{\partial x_j}}^2.$$

The following approximations are then made [3]:

15

$$\nu\overline{\frac{\partial u_i^{r\,2}}{\partial x_j}} = c_\varepsilon \frac{e^{3/2}}{l},$$

$$\overline{u_i^r e} - c_p \Theta \overline{\pi''u_i^r} = 2K_m \frac{\partial e}{\partial x_i},$$

resulting in

$$\frac{\partial e}{\partial t} = -\frac{1}{\rho_0}\frac{\partial}{\partial x_j}(\rho_0 \bar{u}_j e) + \frac{\partial}{\partial x_i}(2K_m \frac{\partial e}{\partial x_i} + \nu \frac{\partial e}{\partial x_j}) - \overline{u_j^r u_i^r}\frac{\partial \bar{u}_i}{\partial x_j} + \frac{g}{\Theta}\overline{u_i^r \theta''}\delta_{i3} - c_\varepsilon \frac{e^{3/2}}{l}.$$

We can actually recover the Smagorinsky model by setting the first three terms to zero. These three terms correspond to the time derivative of TKE, the advection of TKE by the resolved flow and dissipation of TKE. We can think of the Smagorinsky model as a simplification of the TKE model. Then substituting in [3]:

$$\overline{u_j^r u_i^r} = -2K_m S_{ij} \quad \text{and} \quad \overline{u_i^r \theta''} = -K_h \frac{\partial \bar{\theta}}{\partial x_i},$$

gives,

$$2K_m S_{ij}\frac{\partial \bar{u}_i}{\partial x_j} - K_h \frac{g}{\Theta}\frac{\partial \bar{\theta}}{\partial x_i}\delta_{i3} - c_\varepsilon \frac{e^{3/2}}{l} = 0.$$

Then using our definitions for the eddy viscosity coefficients 1.12 we get [3]:

$$\sqrt{e}(c_m l S^2 - c_h l N^2 - c_\varepsilon \frac{e}{l}) = 0.$$

One root is [3]:

$$e = \frac{c_m}{c_\varepsilon}(lS)^2(1 - \frac{c_h}{c_m}\frac{N^2}{S^2})$$

$$= \frac{c_m}{c_\varepsilon}(lS)^2(1 - \frac{c_h}{c_m}Ri).$$

16

Using 1.12 again we arrive at the Smagorinsky model [3]:

$$K_m = (C_s l)^2 |S| \sqrt{\left(1 - \frac{Ri}{Pr}\right)}, \quad \text{where} \quad \frac{K_m}{K_h} = Pr = \frac{c_m}{c_\varepsilon}, \quad \text{and} \quad C_s = \left(c_m \sqrt{\frac{c_m}{c_\varepsilon}}\right)^{1/2}.$$

Plugging in $c_m = 0.1$ and $c_\varepsilon = 0.3$ (corresponding to a $Pr = 1/3$) gives $C_s = 0.24$ which is very close to the value of $C_s \sim 0.21$ found by Deardorff [13] for convection dominated flows and our choice of $C_s = 0.23$.

1.3 The Law of the Wall and Monin-Obukhov Theory

1.3.1 The Law of the Wall for Unstratified Boundary Layers

Previously we neglected molecular viscosity as not important [11, 40]. This is appropriate away from the boundary. However, this does not make sense near the surface, where viscous stress becomes important. For example consider the mean momentum equation (regular momentum equation with no buoyancy and written in terms of pressure):

$$\frac{\partial \bar{u}_i}{\partial t} + \bar{u}_j \frac{\partial \bar{u}_i}{\partial x_j} = -\frac{1}{\rho_0} \frac{\partial \bar{p}}{\partial x_i} + \frac{\partial \bar{\tau}_{ij}}{\partial x_j},$$

where

$$\bar{\tau}_{ij} = \mu \frac{\partial \bar{u}_i}{\partial x_j} - \overline{u_i' u_j'}. \tag{1.15}$$

Clearly the total stress, τ_{ij}, is the sum of the viscous stress, $\mu \partial \bar{u}_i / \partial x_j$, and the Reynolds stress, $\overline{u_i' u_j'}$ [11, 40]. Near the boundary the total stress is approximately equal to the viscous stress (where the Reynolds stress goes to zero), while away from the boundary the total stress is approximately equal to the Reynolds stress (where the viscous stress is assumed to be approximately zero), as shown in Figure 1.3 [11, 40].

We want to determine how the velocity should scale as we move away from the wall. To do this we assume that the velocity is only a function of u, ρ, ν, τ_0, and z (where we assume that the total stress near the wall is a constant τ_0). In terms of dimensions:
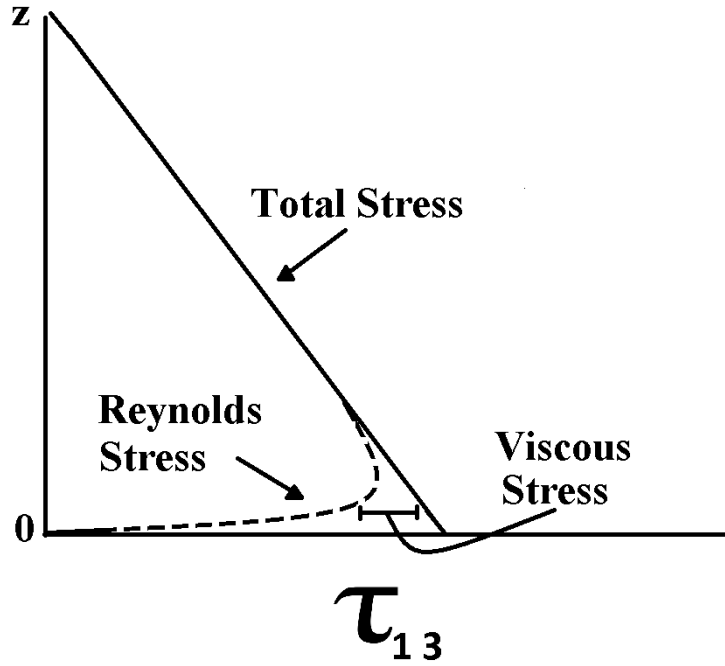
Figure 1.3: Total stress decomposed into Reynolds stress and viscous stress as one approaches a boundary. Near the boundary the viscous stress becomes important while the Reynolds stress disappears. Figure following [40]

$$[u] \sim \frac{L}{T}, \quad [\rho] \sim \frac{M}{L^3}, \quad [\nu] \sim \frac{L^2}{T}, \quad [\tau_0] \sim \frac{M}{LT^2}, \quad [z] \sim L.$$

which from the Buckingham Pi theorem gives [40]:

$$\frac{u}{\sqrt{\frac{\tau_0}{\rho}}} = f(\frac{\sqrt{\frac{\tau_0}{\rho}}z}{\nu}).$$

This is usually written in terms of a *friction velocity* defined as $u_* = \sqrt{\tau_0/\rho}$ [11, 40]. Now referring to equation 1.15 and Figure 1.3 we can conclude that near the wall the total stress is approximately equal to the viscous stress [11, 40]:

18

$$\mu \frac{du}{dz} = \tau_0,$$

which using no-slip boundary conditions gives a solution for u near the boundary as linear (after dividing by ρ to get a solution in terms of u_* and ν) [11, 40]:

$$u = \frac{u_* z}{\nu}.$$

Further from the boundary we might expect that the velocity gradient no longer depends on ν directly. Thus again from dimensional arguments:

$$[\frac{du}{dz}] \sim \frac{L}{T}, \quad [\rho] \sim \frac{M}{L^3}, \quad [\tau_0] \sim \frac{M}{LT^2}, \quad [z] \sim L,$$

which gives [11, 40]:

$$u = \frac{u_*}{\kappa} ln(z),$$

where we have added the dimensionless constant $1/\kappa$ called the von Karman constant [40]. Thus the velocity should scale linearly close to the boundary (this region is often referred to as the viscous sublayer) and logarithmically further away (known as the log-layer). In the case of atmospheric boundary layers it is common to include a surface roughness parameter that modifies the above solution to include effects from non-smooth boundaries. In this case we retain the log-layer solution, but require that at a height z_0 the mean velocity $\bar{u}$ equals 0. This is achieved by writing [11, 40]:

$$\bar{u} = \frac{u_*}{\kappa} ln(\frac{z}{z_0}), \tag{1.16}$$

where z_0 is the roughness parameter and above this roughness height, the solution follows as a log-layer.

1.3.2 Monin-Obukhov Similarity Theory for Stratified Boundary Layers

As we approach the surface the viscosity becomes important and has an affect on the scaling of the mean velocity. We need to determine how to parameterize the surface momentum fluxes

near the surface. It is common to apply Monin-Obukhov similarity theory to determine the temperature and momentum fluxes within the surface layer. These fluxes are parameterized as a function of the dimensionless length parameter above the surface [40]:

$$\zeta = \frac{z}{L},\tag{1.17}$$

where L is the Obukhov length scales defined as [11, 40]:

$$L = -\frac{u_*^3 \bar{\theta}}{\kappa g \overline{w' \theta'}}.\tag{1.18}$$

This length parameter describes the relative importance of shear production of turbulent kinetic energy as compared to buoyancy production of turbulent kinetic energy. Consider the problem of trying to find a parameterization of the eddy viscosity K_M near the wall for the 1-dimensional case. If we assume that the parameterized momentum flux near the wall only depends on u_*, z, and $d\bar{u}/dz$ then by the Buckingham Pi theorem we can find one dimensionless group [11, 40]:

$$\frac{\kappa z}{u_*} \frac{d\bar{u}}{dz} = \phi(\zeta).$$

Now this gives:

$$\frac{(\kappa z)^2}{\phi(\zeta)^2} \frac{d\bar{u}}{dz} = \kappa z \frac{u_*}{\phi(\zeta)}.$$

The l.h.s looks quite similar to the 1-dimensional eddy viscosity given in the Smagorinsky model except now C_s is replaced by $\kappa/\phi(\zeta)$. Thus near the boundary we parameterize the eddy viscosity as:

$$K_M = \kappa z \frac{u_*}{\phi(\zeta)}.\tag{1.19}$$

The dimensionless function $\phi(\zeta)$ must satisfy $\phi(0) = 1$. Notice that this then gives $K_M = 0$ on the boundary surface. Determined largely from experiments (e.g. the Kansas study of 1968 [31]) we choose the following relations [8]:

$$\phi(\zeta) = (1 + 4.8\zeta) \quad \zeta > 0,$$
$$\phi(\zeta) = (1 - 19.3\zeta)^{-1/4} \quad \zeta < 0.$$
(1.20)

Putting this all together we can use (1.16), (1.17), (1.18), and (1.20) to find the momentum fluxes on the lowest level above the ground (1.19).

1.4   Saturation Adjustment Scheme

The LES equations above (1.11) describe a dry CBL. The real atmospheric boundary layer of course includes water vapor and suspended liquid water (i.e. clouds), and thus we need an additional equation that describes this total water content. This is accomplished by including the equation:

$$\frac{\partial \bar{q}_t}{\partial t} = -\bar{u}_j \frac{\partial \bar{q}_t}{\partial x_j} + \frac{1}{\rho_0} \frac{\partial (\rho_0 \bar{\gamma}_{q_t j})}{\partial x_j} + \frac{\partial \bar{F}_{q_t}}{\partial x_j} \delta_{j3} - w_s \frac{\partial \theta'}{\partial z},$$
(1.21)

where q_t is the total mixing ratio, which is the ratio of the density of dry air to water vapor [61, 67]. This quantity is conserved [61, 67] neglecting precipitation and in the above equation we include a possible forcing term and total mixing ratio subsidence analogous to what was done in the potential temperature equation. This section describes how water vapor is converted to liquid water and how this change of state affects the potential temperature.

The condensation of water vapor results in the release of heat (the opposite is true with evaporation which causes cooling) and thus acts as an additional forcing term in the potential temperature budget. To model this phenomenon we use a simple *saturation adjustment scheme* [61, 66]. Simply put this calculates the saturation mixing ratio given the current state variables, and if the mixing ratio is above the saturation level the temperature is adjusted and the liquid water mixing ratio is increased (at the expense of vapour mixing ratio). This model will assume that water can only be in vapour or suspended liquid water form, i.e. we will assume no precipitation, and that changes from vapour to liquid occur instantaneously. Before presenting the details of how this is accomplished, let us first define the important quantities that will be used. The vapour, liquid, and total mixing ratios are defined as [61]:

$$q_v = \frac{\rho_v}{\rho_d} = \frac{\text{density of water vapour}}{\text{density of dry air}},$$

$$q_l = \frac{\rho_l}{\rho_d} = \frac{\text{density of liquid water}}{\text{density of dry air}},$$

$$q_t = \frac{\rho_v + \rho_l}{\rho_d} = \frac{\text{density of liquid water and water vapour}}{\text{density of dry air}} = q_v + q_l.$$

These give the moisture content (whether as vapour or liquid) in dimensionless form, i.e. g/kg. The total mixing ratio is a conserved variable since we do not consider precipitation.

Dalton's' law of partial pressures says the total pressure of a mixture of gases is the sum of the pressures of the individual components [61, 21]. Therefore *vapour pressure* is the pressure exerted by a vapour in thermodynamic equilibrium at a given temperature. We denote *vapour pressure* by e. Now imagine a thermodynamically insulated box that contains both liquid water and dry air. If the temperature of the dry air is hot enough, then water molecules on the surface of the liquid water will become excited enough to evaporate and become water vapour [61]. On the other hand as the temperature cools, water vapour molecules will crash into the liquid water as condensation. Eventually a balance will be achieved where there is no net evaporation-condensation. The vapour (now a mixture of water vapour and dry air) pressure at which this is achieved is called the *saturation vapour pressure* which is denoted by e_s. The saturation mixing ratio is defined as the mass of water vapour at saturation vapour pressure divided by the mass of dry air [61, 21]:

$$q_s = \frac{M_{vs}}{M_d} = \frac{\rho_{vs}}{\rho_d} = \frac{\frac{e_s}{R_v T}}{\frac{p-e_s}{R_d T}} = \varepsilon \frac{e_s}{p - e_s}.$$

where $\varepsilon = \frac{R_v}{R_d}$ and $e_d = p - e_s = \rho_d R_d T \Rightarrow \rho_d = \frac{p-e_s}{R_d T}$. For example 100% relative humidity means that any more water vapour would result in condensation, i.e [61, 21]:

$$RH = 100 \frac{q_v}{q_s} = 100 \frac{e}{e_s}.$$

We will also need the Clausius-Clapeyron equation, which describes the dependence of e_s on T [61, 21]:

$$\frac{de_s}{dT} = \frac{L_v e_s}{R_v T^2},$$

22

where L_v is the latent heat of vaporization. If we assume that the latent heat of vaporization is constant, which to a good approximation in the atmosphere it is, then this differential equation becomes separable and so can be solved [61]:

$$e_s = Ae^{-\frac{L_v}{R_v T}}.$$

An appropriate initial condition, determined from experiments is $e_s(273.16) = 611$ Pa. This gives the equation for saturation vapour pressure to be [61]:

$$e_s(T) = Ae^{-\frac{L_v}{R_v T}} \quad \text{where} \quad A = 2.53 \times 10^{11} \quad \text{kPa}.$$

Finally, we introduce a number of important variables that describe the joint effects of heat and moisture. The virtual potential temperature is defined as [61, 21, 67]:

$$\theta_v = \theta(1 + (\frac{R_v}{R_d} - 1)q_t - (\frac{R_v}{R_d})q_l),$$
$$\approx \theta(1 + 0.6q_v - q_l),$$

where we can also define the virtual temperature as:

$$T_v = T(1 + (\frac{R_v}{R_d} - 1)q_t - (\frac{R_v}{R_d})q_l),$$
$$\approx T(1 + 0.6q_v - q_l).$$

We should point out that water vapour is actually lighter than dry air [2] [67]. Virtual potential temperature is *the temperature that dry air must have to equal the density of moist air at the same pressure* [67]. Because moist air is less dense than dry air, this ensures that the virtual potential temperature of unsaturated moist air is always greater than the potential temperature of dry air. The liquid water potential temperature is defined as [61]:

---

[2]This is because both O_2 and N_2, the primary molecules in the dry atmosphere, both have higher atomic mass than the water molecule H_2O

$$\theta_l = \theta e^{\left(-\frac{q_l L_v}{c_p T}\right)},$$

or the liquid water temperature:

$$T_l = T e^{\left(-\frac{q_l L_v}{c_p T}\right)}.$$

The liquid water potential temperature is conserved in a reversible adiabatic process (along with the total mixing ratio). It is the liquid water potential temperature that we use for our energy equation:

$$\frac{\partial \theta'_l}{\partial t} = -u_i \frac{\partial \theta'_l}{\partial x_i} + \frac{\partial F_\theta}{\partial x_i} \delta_{i3} - w_s \frac{\partial \theta'_l}{\partial z}.$$

which we can see reduces to the potential temperature in the dry case.

How do we use the preceding definitions to determine when clouds (i.e. liquid water suspended in the atmosphere) should form? First we note that total mixing ratio is conserved (clearly the total amount of water, whether in liquid or vapour form, must remain constant by conservation of mass assuming no precipitation). Secondly, consider Figure 1.4 which plots the saturation mixing ratio against temperature. Let us assume that we initially begin with $q_l = 0$ which means that initially $q_v = q_t$ since the total mixing ratio is conserved. Also then $T_l = T$ initially. Let us assume then that in the coarse of integrating our equations forward in time we arrive at the situation where $q_v > q_s$ as shown in the Figure by point (a). Then the air is super-saturated and the excess water vapour will condense into liquid. This results in a decrease in q_v followed by a corresponding increase in q_l. Also the temperature increases so that we return to saturation as shown in the Figure by point (b). Because the total mixing ratio is conserved, the increase in q_l is simply the difference between $q_t - q_s$. The only question then is how to actually find the correct temperature adjustment.

Consider the equation for liquid water temperature. We can write:

$$T_l = T e^{\left(-\frac{q_l L_v}{c_p T}\right)},$$
$$= T e^{\left(-\frac{(q_t - q_s) L_v}{c_p T}\right)},$$
$$0 = T_l - T e^{\left(-\frac{(q_t - q_s) L_v}{c_p T}\right)}.$$

24
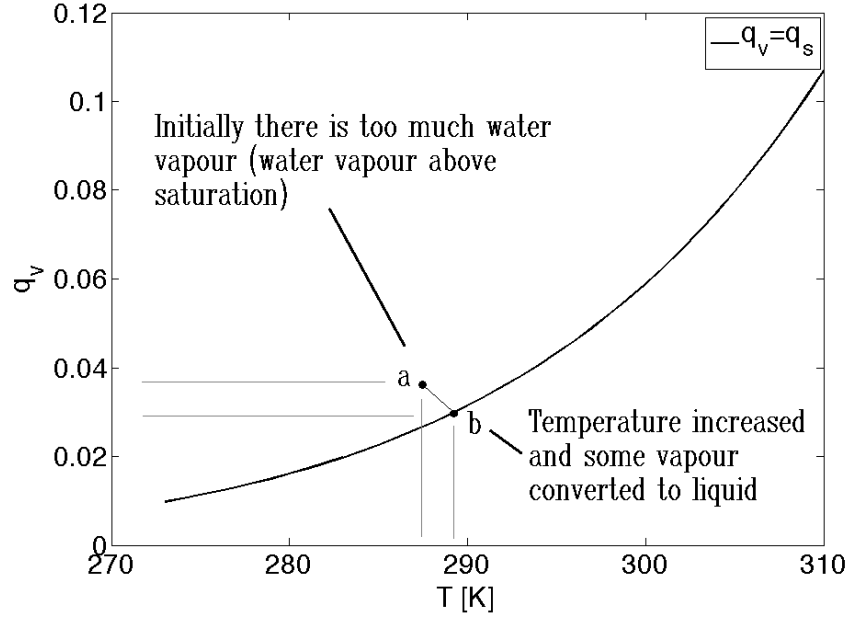
Figure 1.4: Illustration of phase change between vapour and liquid water as well as corresponding temperature increase.

This equation has the form $f(T) = 0$ where $f(T)$ equals the r.h.s. Thus we can solve for T by using Newton's method of root-finding [41, 66].

$$T_{n+1} = T_n - \frac{f(T_n)}{f'(T_n)}, \tag{1.22}$$

where $f'(T)$ equals:

$$f'(T) = e^{\left(-\frac{(q_t - q_s)L_v}{c_p T}\right)} + T e^{\left(-\frac{(q_t - q_s)L_v}{c_p T}\right)} \left[\frac{\frac{dq_s}{dT}L_v c_p T + (q_t - q_s(T))L_v c_p}{c_p^2 T^2} \right].$$

Therefore,

25

$$\frac{f(T)}{f'(T)} = \frac{Te^{\left(-\frac{(q_t-q_s)L_v}{c_pT}\right)} - T_l}{e^{\left(-\frac{(q_t-q_s)L_v}{c_pT}\right)} + Te^{\left(-\frac{(q_t-q_s)L_v}{c_pT}\right)}\left[\frac{\frac{dq_s}{dT}L_vc_pT+(q_t-q_s(T))L_vc_p}{c_p^2T^2}\right]},$$

$$= \frac{T - T_l e^{\left(\frac{(q_t-q_s)L_v}{c_pT}\right)}}{1 + T\left[\frac{\frac{dq_s}{dT}L_vc_pT+(q_t-q_s(T))L_vc_p}{c_p^2T^2}\right]},$$

$$\approx \frac{T - T_l\left[1 + \frac{(q_t-q_s(T))L_v}{c_pT}\right]}{1 + \frac{L_v}{c_pT}\left[T\frac{dq_s}{dT} + (q_t - q_s(T))\right]}. \tag{1.23}$$

We can find an equation for $q_s'(T)$ by using the definition of q_s and the Clausius-Clapeyron equation [66]:

$$\frac{dq_s}{dT} = \varepsilon\left(\frac{\frac{de_s}{dT}(p-e_s) - \frac{de_s}{dT}e_s}{(p-e_s)^2}\right),$$

$$= \frac{L_vq_s}{R_vT^2} - \frac{1}{\varepsilon}\frac{L_vq_s^2}{R_vT^2},$$

$$= \frac{L_vq_s}{R_vT^2} - \frac{L_vq_s^2}{R_dT^2}. \tag{1.24}$$

Thus 1.22, 1.23, and 1.24 give us an iterative method for finding the adjusted temperature.

1.5 Turbulence and Convective Boundary Layers

1.5.1 A Brief History of Turbulence

The study of turbulence dates back to at least the time of da Vinci who referred to the phenomena as "Turbolenza" [50] and hence cemented its modern name. Despite the length of time that turbulence has been investigated and despite, as we shall see, the long list of mathematical and physical titans of their respective times, turbulence remains, to use Richard Feynman's own words, *"the most important unsolved problem of classical physics"*. In fact no universally accepted definition for turbulence even exists. Perhaps the most famous informal description of turbulence comes in the form of a poem by Richardson in 1922 [60, 50]:

Big whorls have little whorls,
which feed on their velocity;
And little whorls have lesser whorls,
And so on to viscosity.

A quote from G.I. Taylor on the definition of turbulence reads [72, 50]:

Turbulence is an irregular motion which in general makes its appearance in fluids, gaseous or liquid, when they flow past solid surfaces or even when neighboring streams of the same fluid flow past or over one another.

Despite the ambiguity found in trying to define precisely what turbulence is, we do know it when we see it. A turbulent flow appears chaotic and irregular. Turbulent flows are also characterized as having vorticity and the formation of eddies at both large and small scales. This vorticity is generated by vortex stretching meaning that turbulence is, strictly speaking, a 3-dimensional phenomena (although many of the same ideas and tools used in turbulence research are also used when investigating 2-dimensional flows).

One difficulty faced in the study of turbulence is that its very underlying equations, i.e the Navier-Stokes equations, do not admit analytical solutions except for the most trivial of cases often accompanied by drastically simplifying assumptions. While finding unique solutions to linear differential equations is relatively easy, doing the same for the Navier-Stokes equations, which are nonlinear, is impossibly hard and so little traction can be found on the analytical front. This is one of the reasons for the prominence of statistical methods in turbulence research.

Some of the most important early work on turbulence was done by Osbourne Reynolds. His famous flowing dye experiments investigating the transition in fluids from laminar to turbulent are well known within the fluids community (1883) [11]. It was Reynolds who first investigated this transition and discovered the non-dimensional number bearing his name that describes the relative importance of the diffusive term to the nonlinear advective term in the Navier-Stokes equations. It was also Reynolds who first decomposed the Navier-Stokes equations into a mean part and a fluctuating perturbation part, similar to what is done in LES by separating the flow field into filtered and unfiltered parts. The notion that turbulence is a random process also dates to the late 19th century, with Reynolds and Poincaré being notable contributors.

One of the first major results of the statistical view of turbulence came from Boussinesq's eddy-viscosity idea and the subsequent work of Prandtl in 1925 who introduced Prandtl's mixing length theory [58]. This theory, actually drawing on ideas from thermodynamics, assumes that

the velocity has a linear profile. For example consider a fluid flowing in the x-direction, where the fluid velocity only depends on the y-direction:

$$u = u(y) \quad v = 0 \quad w = 0.$$

Now consider a small distance away we can approximate the $u(y = l)$ velocity through use of a Taylor expansion [40]:

$$u' = u(y) - u(y - l) \approx l\frac{du}{dy} - \frac{l^2}{2}\frac{d^2u}{dy^2}.$$

Therefore in general we may approximate $u'_i \approx l(\partial u_i \partial x_j)$ which then gives:

$$-\overline{u'_i u'_j} \approx l^2 (\frac{\partial u_i}{\partial x_j})^2.$$

It should be noted that this mixing length idea is far from rigorous - Prandtl himself recognizing that this approximation has limitations. Nonetheless this idea has remained important, for example in the eddy viscosity of LES.

Much of the statistical theory and tools well known to turbulence researchers, such as statistical correlations and power spectra, originates with the work of G.I. Taylor in the 1930's. Taylors' hypothesis [70, 25, 75], which says that the velocity measured at a fixed point within an eddy remains unchanged at a later time except for the effect of being advected by the mean flow, i.e. $u(x,t) = u(x - Ut,t)$ where U is the mean flow speed. Thus it is often said that the turbulence within the passing eddy is frozen. This hypothesis is clearly only valid if the turbulence is relatively weak within the eddy as compared to the background velocity.

Perhaps the most important discovery in the field of turbulence, at least from the point of view of the work presented in this thesis, comes from the Russian mathematician Andrei N. Kolmogorov, in his 1941 papers [36, 37] and his 1962 paper [38]. In these papers Kolmogorov found the form of the kinetic energy spectrum and hence found the distribution of energy as a function of eddy size. We will return to Kolmogorov theory in the subsequent pages and explain it in more detail.

The 1960s ushered in great opportunities for research in turbulence with the advent of better experimental techniques, and perhaps most importantly, with the introduction of the digital computer. For example as early as 1963, Lorenz was performing crude simulations of weather using digital computers. In particular Lorenz noted the sensitivity his system exhibited to initial conditions, often referred to as the butterfly effect.[40].
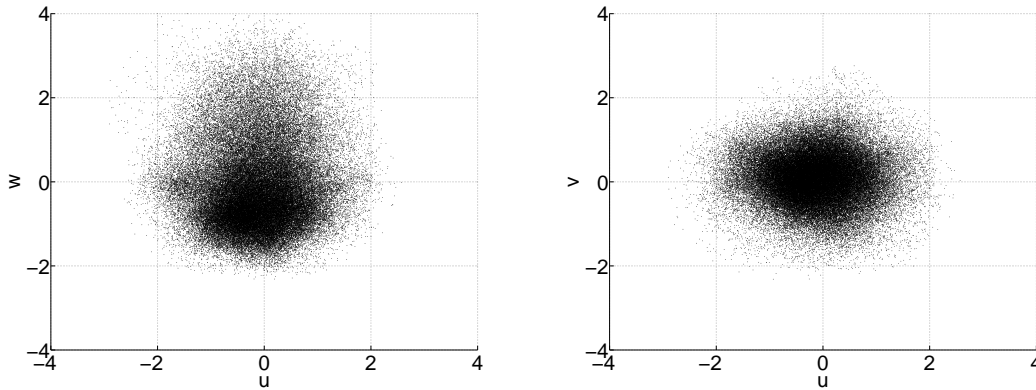
Figure 1.5: Scatter plots of velocities *u* and *w* and velocities *u* and *v*. Clearly there exists more anisotropy in the vertical than there does in the horizontal. The data was taken from a convective boundary simulation.

Despite the great successes of the statistical approach, there remains no universal turbulence theory. Instead we have different theories for different flow types, i.e. boundary layer theory [11]. The problem arises because no closed set of equations that describe the statistical quantities like the mean and variance of a flow exist. This is the problem of closure. It is a great irony that we have equations for the velocities, u_i, which are random, and yet have no equations for statistical quantities like the mean, $\bar{u}_i$, which are well behaved!

1.5.2   The Energy Spectrum

The previous discussion has been somewhat informal; we have introduced some of the big ideas of turbulence theory while at the same time avoiding much of the formal definitions and equations. Let us now present the idea of the energy spectrum and the meaning of isotropy.

A fluid is said to be isotropic if the mean properties of the flow *have reflectional symmetry and are invariant under rotations within the frame of reference* [11]. Likewise a fluid is homogeneous if its properties are *invariant under translation* [11]. One simple and intuitive way to test whether a fluid is isotropic is to look at a scatter plot comparing the *u*, *v*, and *w* velocities (see Figure 1.5. For example the *uu*, *vv*, and *ww* products would show up in a scatter plot as dots evenly distributed around their centre in a circular pattern. For anisotropic flows, these velocity products would result in an elliptical pattern in the scatter plot.

Another related way to think about isotropic turbulence is through the velocity correlation tensor defined as [11]:

$$Q_{ij}(\vec{r}) = \langle u_i(\vec{x})u_j(\vec{x}+\vec{r})\rangle, \tag{1.25}$$

where the angled brackets indicate an average. When $\vec{r} = 0$ for isotropic flows, we would expect that the following holds:

$$\langle u_1 u_1 \rangle = \langle u_2 u_2 \rangle = \langle u_3 u_3 \rangle = U^2,$$

and,

$$\langle u_1 u_2 \rangle = \langle u_1 u_3 \rangle = \langle u_2 u_3 \rangle = 0.$$

For non-zero $\vec{r}$ the above velocity correlation is often referred to as a two-point correlation. In this case we would expect that for large $|\vec{r}|$, the velocity correlations will go to zero. On the other hand, for $|\vec{r}| \to 0$, we get the one-point correlations shown above. If we look at the velocity correlation tensor in the x-direction, based on the above ideas, we might get something like [11, 75]:

$$Q_{11}(r\hat{e_x}) = U^2 f(r) \quad \text{and} \quad Q_{22}(r\hat{e_x}) = U^2 g(r),$$

where $f(r)$ and $g(r)$ are shown in Figure 1.6 and are called the longitudinal and lateral velocity correlation functions respectively [43, 11, 40, 75]. These functions then tell us how well correlated nearby velocities are along the x-axis. Two velocities within an eddy are likely to be well-correlated, while two velocities separated by a larger distance and residing in different eddies are likely to be poorly correlated. This gives us a more formal way of computing the length scale of the largest eddies. We can define the *integral length scale* as [11]:

$$l = \int_0^\infty f(r)dr.$$

We can also take the Fourier transform of the velocity correlation tensor, called the spectral tensor [11, 75]:

$$\phi_{ij}(\vec{k}) = \frac{1}{(2\pi)^3}\int_0^\infty Q_{ij}(\vec{r})e^{-i\vec{k}\vec{r}}d\vec{r}, \tag{1.26}$$

which then defines the velocity correlation tensor as [11, 75]:
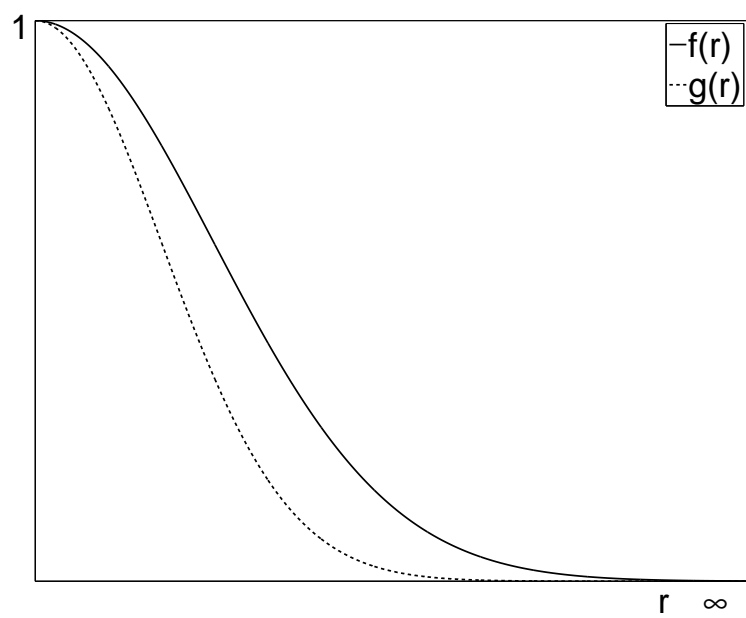
Figure 1.6: Longitudinal (f) and Lateral (g) velocity correlation functions.

$$Q_{ij}(\vec{r}) = \int_{-\infty}^{\infty} \phi_{ij}(\vec{k})e^{i\vec{k}\vec{r}}d\vec{k}. \tag{1.27}$$

Therefore the velocity correlation tensor and the spectral tensor form a Fourier transform pair [11, 75]. For isotropic turbulence it can be shown that ϕ_{ij} must have the form [11]:

$$\phi_{ij} = A(k)k_ik_j + B(k)\delta_{ij}. \tag{1.28}$$

The incompressibility condition implies [11]:

$$k_i\phi_{ij} = k_j\phi_{ij} = 0. \tag{1.29}$$

Combining 1.28 and 1.29 gives [11]:

$$
\begin{aligned}
k_i\phi_{ij} &= A(k)k_i^2k_j + B(k)k_i\delta_{ij} = 0, \\
&= A(k)k^2k_j + B(k)k_j = 0 \quad \text{where} \quad k^2 = k_1^2 + k_2^2 + k_3^2, \\
&= (A(k)k^2 + B(k))k_j = 0, \\
\Rightarrow A(k) &= -\frac{B(k)}{k^2}.
\end{aligned}
$$

Thus ϕ_{ij} has the form [11, 75]:

$$\phi_{ij} = B(k)(\delta_{ij} - \frac{k_ik_j}{k^2}).$$

Then,

$$\frac{1}{2}\phi_{ii} = B(k),$$

where we have summed over i. Now consider: [11]

$$\frac{1}{2}\langle u_i^2 \rangle = \frac{1}{2}\int \phi_{ii}(\vec{k})\vec{d}k,$$

$$= \int_0^\infty 2\pi k^2 \phi_{ii} dk,$$

$$= \int_0^\infty E(k) dk \quad \text{where} \quad E(k) = 2\pi k^2 \phi_{ii}.$$

But since $\frac{1}{2}\phi_{ii} = B(k)$ then,

$$\frac{1}{4}E(k) = \frac{1}{2}\pi k^2 \phi_{ii} = \pi k^2 B(k).$$

Therefore [11, 75],

$$\phi_{ij} = \frac{E(k)}{4\pi k^2}(\delta_{ij} - \frac{k_i k_j}{k^2}). \tag{1.30}$$

In an unbounded domain, the horizontal wavenumber spectra of vertical and horizontal kinetic energy are defined as:

$$E_v(k_h) = \int_0^\infty \int_0^{2\pi} \frac{1}{2}\phi_{33} k_h d\theta dk_z \quad E_h(k_h) = \int_0^\infty \int_0^{2\pi} \frac{1}{2}(\phi_{11} + \phi_{22}) k_h d\theta dk_z, \tag{1.31}$$

where integration is over a cylinder in wavenumber space centred on the k_z axis with radius k_h. We assume the spectral tensor, ϕ_{ij}, has the usual isotropic form (e.g. [57]):

$$\phi_{ij} = \frac{E(k)}{4\pi k^2}\left(\delta_{ij} - \frac{k_i k_j}{k^2}\right), \tag{1.32}$$

where $k = \sqrt{k_x^2 + k_y^2 + k_z^2}$. Substituting (1.32) into (1.31) yields:

$$E_v = \frac{1}{4}\int_0^\infty \frac{E(k)}{k^2}(\frac{k_h^2}{k^2})k_h dk_z \quad E_h = \frac{1}{4}\int_0^\infty \frac{E(k)}{k^2}(\frac{k_h^2 + 2k_z^2}{k^2})k_h dk_z.$$

33

Using $k_z^2 = k^2 - k_h^2$, the substitution $\tau = k/k_h$, and assuming a Kolmogorov energy spectrum $E(k) = \alpha \epsilon^{2/3} k^{-5/3}$, the above integrals can be reduced to:

$$E_v = \frac{1}{4} \alpha \epsilon^{2/3} k_h^{-5/3} \int_1^\infty \frac{\tau^{-14/3}}{\sqrt{\tau^2 - 1}} d\tau$$

$$E_h = \frac{1}{4} \alpha \epsilon^{2/3} k_h^{-5/3} \int_1^\infty \frac{(2\tau^2 - 1)\tau^{-14/3}}{\sqrt{\tau^2 - 1}} d\tau.$$

These integrals can be numerically evaluated to give a vertical-to-horizontal ratio:

$$\frac{E_v}{E_h} \approx \frac{0.611861}{1.07075} \approx 0.5714.$$

Thus we have rudimentary measure for testing whether a flow might be isotropic using 2-dimensional slices of the flow. In the case of one-dimensional spectra, this ratio would be $4/3$ [75].

1.5.3 Kolmogorov Theory

Kolmogorov's 1941 [36, 37, 38] theory of isotropic turbulence ranks as one of the most significant advances in the study of turbulent fluids. In particular, Kolmogorov was able to derive the form of the kinetic energy spectrum thus giving the distribution of energy as a function wavenumber, or eddy size. His ideas of course were not born in a vacuum - drawing instead on earlier works for example Richardsons energy cascade theory [11]. Before deriving this energy spectrum, let us first examine a fundamental difference between inviscid flows and flows with very low viscosity.

Consider a turbulent flow, i.e. the atmospheric convective boundary layer. Let l be a length scale of the largest eddies [3]. These eddies will be at most the thickness of the boundary layer, say ~ 1000 m. Also let U be a velocity scale of the largest eddies. We might expect this to be ~ 1 m/s for example. Thus at the largest scales, we can define the Reynolds number as $Re = Ul/\nu \sim 6 \times 10^7 \gg 1$ (where $\nu \sim 1.5 \times 10^{-5}$ for air). Because $Re \gg 1$, we might expect that the flow would behave as an inviscid flow where viscosity is not important. This turns out to be incorrect however as we shall see. Now let us define a length and velocity scale that

---

[3]We will follow Davidson here and informally define an eddy as a *blob of vorticity and its associated velocity field* [11]

represent small scale motions. Let η be such a scale. Kolmogorov proposed that $\eta = f(\nu, \varepsilon)$ where $\varepsilon = 2\nu S_{ij}S_{ij}$ [11] is the molecular dissipation rate of KE.

We can perform some simple dimensional analysis to determine the function f. We know that $[\nu] = L^2/T$ and $[\varepsilon] = L^2/T^3$. Therefore [43, 11, 75],

$$\eta = (\frac{\nu^3}{\varepsilon})^{\frac{1}{4}}.$$

Thus the effect of decreasing ν is to decrease η to smaller scales. Regardless of how much we decrease ν though, the nonlinear term will always ensure that viscosity becomes important at some scale η. This last statement then highlights the fundamental difference between completely inviscid flows and flows which may seem *nearly* inviscid because of very small viscosity! No matter how small the viscosity (or equivalently how high the Reynolds number) the nonlinear term will ensure that at some scale the viscosity will become important. In the same way we found a small length scale η, we can also use dimensional analysis to find a small time scale, τ, and a small velocity scale v. Doing so gives [43, 11, 75]:

$$\tau = (\frac{\nu}{\varepsilon})^{\frac{1}{2}} \qquad\qquad v = (\nu\varepsilon)^{\frac{1}{4}}.$$

Richardson proposed a theory of energy cascade. The idea is that on average energy transfers from larger eddies to smaller ones in a step by step cascade. If we let k_i be the wavenumber at which energy is injected into the fluid and if we let k_d be the wavenumber where energy is dissipated from the fluid by viscosity, then in between energy moves from small k_i to large k_d in a incremental way. Around k_i the energy is dictated by the forcing, but for $k \gg k_i$ Kolmogorov hypothesized that the turbulence is largely independent of the large scale eddies. In the range $k \gg k_i$, known as the universal equilibrium range, Kolmogorov suggested that the energy spectrum should depend on k, k_d, and ε. With this assumption, he used dimensional analysis to find $E(k)$ [43, 11, 75]:

$$[E(k)] = \frac{L^3}{T^2} \qquad [k] = [k_d] = \frac{1}{L} \qquad [\varepsilon] = \frac{L^2}{T^3}.$$

Buckingham Pi theorem tells us that there are $4 - 2 = 2$ dimensionless groups. Using $\frac{k}{k_d}$ as one group we find that:

$$E(k) = \varepsilon^{\frac{2}{3}} k^{\frac{-5}{3}} f(\frac{k}{k_d}).$$

If we define k_i as the wavenumber at which energy is injected and k_d as the wavenumber at which energy is dissipated, Kolmogorov hypothesized that for the range of k, $k_i \ll k \ll k_d$, $f(\frac{k}{k_d}) = $ constant. This range is known as the inertial range and we get [43, 11, 75]:

$$E(k) = c\varepsilon^{\frac{2}{3}}k^{\frac{-5}{3}}. \tag{1.33}$$

In addition to the above energy spectrum, we can find a similar result for the spectrum of temperature fluctuations. To do so we apply dimensional analysis in the same way as before. We are given three dimensional units: C^o (temperature), meters (length), and seconds (time), and we have six physical variables: γ, ε_T, ε, k, k_d k_T, where $\overline{T'^2} = \int_o^\infty \Gamma(k)\,dk$, and $\varepsilon_T = \kappa\overline{(\partial T'/\partial x_j)^2}$ [5, 6]. Thus again by the Buckingham Pi theorem we expect three dimensionless groups. Two of these dimensionless groups will be k/k_d and k/k_T.

$$[\Gamma] = (C^o)^2 m \qquad [\varepsilon_T] = \frac{(C^o)^2}{s} \qquad [\varepsilon] = \frac{m^2}{s^3} \qquad [k_d] = [k_T] = [k] = \frac{1}{m},$$

$$\frac{\Gamma(k)}{\varepsilon^\alpha \varepsilon_T^\beta k^\gamma} = (C^o)^{2-2\beta} m^{1+\gamma-2\alpha} s^{3\alpha+\beta},$$

$$\Rightarrow \beta = 1 \qquad \alpha = -\frac{1}{3} \qquad \gamma = -\frac{5}{3},$$

$$\Gamma(k) = \varepsilon_T \varepsilon^{-\frac{1}{3}} k^{-\frac{5}{3}} f(\frac{k}{k_d}, \frac{k}{k_T}).$$

This therefore gives a $-5/3$ scaling within the inertial range for the temperature spectrum. We can actually go a step further. When $Pr = (\frac{\nu}{\kappa}) \ll 1$, then $\kappa \gg \nu$. Thus we expect the temperature to be smeared out by thermal diffusivity before the velocity is smeared out by viscosity. Therefore we may consider an additional range, known as the "viscous convective subrange" where thermal diffusivity is strong, but where viscosity is still weak. Batchelor (1959) did this and found that for the case where $\kappa \gg \nu$, the temperature fluctuation spectrum should look like [5, 6]:

$$\Gamma(k) = \varepsilon_T \varepsilon^{\frac{2}{3}} \kappa^{-3} k^{-\frac{17}{3}}. \tag{1.34}$$

1.5.4 The Kinetic Energy Budget

An equation for the kinetic energy budget can be found by multiplying by $\frac{1}{2}\rho_0\hat{\bar{u}}_i^*$, and adding the complex conjugate. The resulting equation is:

$$\frac{\partial E}{\partial t}(\vec{k},z) = T(\vec{k},z) + P(\vec{k},z) + B(\vec{k},z) + D(\vec{k},z), \tag{1.35}$$

where

$$T(\vec{k},z) = -\operatorname{Re}(\hat{\bar{u}}_i^* \mathcal{F}(\frac{\partial}{\partial x_j}(\rho_0\bar{u}_i\bar{u}_j))),$$

$$P(\vec{k},z) = \frac{1}{2}c_p\Theta_0\rho_0\operatorname{Re}(-ik\hat{\bar{u}}^*\hat{\bar{\pi}}' - il\hat{\bar{v}}^*\hat{\bar{\pi}}' - \hat{w}^*\frac{\partial\hat{\bar{\pi}}'}{\partial z}),$$

$$B(\vec{k},z) = \frac{g}{\Theta_0}\operatorname{Re}(\rho_0\hat{w}^*\hat{\bar{\theta}}'),$$

$$D(\vec{k},z) = \operatorname{Re}(\hat{\bar{u}}_i^* \mathcal{F}(\frac{\partial}{\partial x_j}(\rho_0\bar{\tau}_{ij}))).$$

The evolution of $E(\vec{k},z)$ is defined by four terms: the advection or nonlinear transfer $T(\vec{k},z)$, the pressure term $P(\vec{k},z)$, the buoyancy flux or heat flux $B(\vec{k},z)$, and the SGS dissipation $D(\vec{k},z)$. Taking the horizontal Fourier transform of the anelastic continuity equation gives: The pressure term P can be rewritten using the continuity equation,

$$-ik(\rho_0\hat{\bar{u}}^*) - il(\rho_0\hat{\bar{v}}^*) + \frac{\partial}{\partial z}(\rho_0\hat{w}^*) = 0.$$

Multiplying by $\bar{\pi}'$, the pressure term P can be rewritten as:

$$P(\vec{k},z) = -c_p\Theta_0\operatorname{Re}(\frac{\partial}{\partial z}(\rho_0\hat{w}^*\hat{\bar{\pi}}')), \tag{1.36}$$

which implies that it goes to zero when integrated over the depth of the domain. From these quantities, we can compute one-dimensional spectra in terms of the horizontal wavenumber $k_h = \sqrt{k^2 + l^2}$ by binning over k and l in the usual way [73]. It is precisely this budget that we will be

examining for the atmospheric boundary layer. By examining each term, i.e. nonlinear transfer, forcing from buoyancy, and dissipation, we hope to gain insight into the dynamics of the kinetic energy spectrum.

1.5.5   A Brief History of Convective Boundary Layer Research

With the gradual increase in computing power between the 1960's and the present it became feasible to numerically solve the equations of motion for an atmospheric boundary layer. These simulations relevant to the present investigation were first being performed throughout the 1960-1970's, in particular the pioneering work of D.K. Lilly [45] and Deardorff [13, 14] that led to the development of LES. It is LES that appears to hold the most promise in modeling engineering and atmospheric flows, at least for the foreseeable future. In fact a lot of recent work has been dedicated to finding improved models of the parameterized sub-grid scale fluxes, for example dynamical models.

Lilly [45] extended the Smagorinsky eddy viscosity model [65] to include convection and performed one of the first three-dimensional LES experiments [46]. Throughout the early 1970's, Deardorff used different techniques to parameterize the sub-grid scale (SGS) fluxes in a CBL, including the Smagorinsky model [14] and the turbulent kinetic energy (TKE) model [17]. Key differences were found between CBLs simulated with these two SGS models. For example, the Smagorinsky model tended to smooth out gradients in the entrainment zone more than the TKE model. Deardorff [13] found that for flows dominated by thermal convection, a Smagorinsky coefficient near $C_s = 0.21$ is appropriate, while for flows dominated by shear a lower Smagorinsky coefficient around $C_s = 0.13$ should be used.

The kinetic energy budget was measured in physical space by Moeng [52]. In the spectral domain, kinetic energy spectra in the CBL have been found to have a $-5/3$ slope (e.g. [15, 16, 54, 68]). This spectral slope is a necessary condition of isotropic turbulence, and local isotropy has been investigated by considering the spectral ratio of one-dimensional vertical-to-horizontal (transverse to longitudinal) kinetic energy, which should be $4/3$ in isotropic turbulence [75]. Deardorff [13] found ratios that were much larger than this value as did the subsequent studies of Mestayer [51], Moeng & Wyngaard [54], and Schmidt & Schumann [64]. It seems that the pressure perturbations are only strong enough to encourage local isotropy at the smallest scales. Indeed, the wind tunnel experiments [34] have since found ratios that are very close to the theoretical value (only slightly larger) in the small scales.

The heat flux spectrum is an important term in the spectral KE budget, as it corresponds to a source of KE from buoyant production. Results from the LES experiments of Schmidt & Schumann [64] and the observational study of Kaimal et al. [32] indicate that near the surface heat

is transported up by small scale turbulent motions followed by a rapid transfer to larger scales throughout the mixing layer. Significantly, heat appears to be transported within the entrainment region predominantly by the large scale turbulent motions and not small scale motions as is the case near the surface. Similar results were seen in the wind tunnel experiments of Kiaser & Fedorovich [34] throughout the CBL except near the surface where the experiments showed large scale heat transport which was attributed to surface shear effects.

Observational studies have been performed by many authors (e.g. [42, 32, 9, 33, 28]), and these findings have been very useful for validating numerical results. Good agreement has been found between observed and simulated KE and heat flux spectra (for example comparing the computed LES heat flux spectra of Schmidt & Schumann [64] with the observed spectra of Kaimal et al. [32]). Large-scale peaks in the heat flux and kinetic energy spectra have been seen in some studies, possibly caused by coherent structures in the flow [28]. The LES work of Schmidt & Schumann [64] found similar peaks, but cautioned that the coherent structure interpretation is not universally accepted. For example, Deardorff & Willis' [18] water tank study of CBL did not find statistically significant peaks in the spectra corresponding to coherent structures nor were such peaks observed in the overland aircraft measurements of Lenschow [42].

Numerous comparison studies examining differences in sub-grid scale parameterizations [23, 69, 24, 30] and differences between shear and buoyancy driven flows [53] have also been performed. In particular, Niewstadt et al [23] compared four LES codes that were run with similar domain setups but different parameterizations of the sub-grid scale fluxes. Despite these differences, the LES results showed a high level of agreement in both physical space statistics and kinetic energy spectra. In [30] the standard Smagorinsky-Lilly model was compared with the dynamic Smagorinsky parameterization and similar insensitivities were found. The robustness of LES simulations despite differences in the SGS parameterization is partially due to the inherent large scale eddies that develop in convection driven turbulent flows. It is also encouraging that the LES results are reasonably insensitive to the choice of SGS model as it gives confidence in the use of LES as a tool for studying CBL turbulence.

More recent high-resolution LES of the CBL have examined the effects of grid resolution on physical space statistics and kinetic energy spectra [68]. Resolutions of up to 1024^3 grid points (corresponding to $5 \times 5 \times 2$ m grid spacings) were employed. Within the mixing layer ($0.1 < z_i <$ 0.9, where z_i is the inversion height) the variances and vertical heat flux converged (in physical space) for resolutions of 256^3. However, the temperature variance increased with successive resolutions within the entrainment zone. Both horizontal and vertical velocities showed $-5/3$ spectra, however a two-slope character was observed in the horizontal spectra particularly near the surface and the boundary layer height. It was observed that the horizontal spectra were shallower than $-5/3$ in the larger scales followed by a transition to a $-5/3$ slope at smaller scales. The peak vertical velocity spectra also shifted to higher wavenumbers as z/z_i decreased.

Chapter 2

Methodology

> "But I don't want to go among mad people," said
> Alice. "Oh, you can't help that," said the cat.
> "We're all mad here."
> —Lewis Carrol in Alice in Wonderland

In this chapter we present a description of the UCLA LES model [4] that is used to numerically integrate the anelastic equations (1.11). This code was chosen because it allowed for the solution of both dry and moist CBL's using either Smagorinsky or TKE subgrid parameterizations. The code has been used in a number of related studies and includes fairly comprehensive documentation. In the following sections we provide details on how the UCLA LES model integrates the anelastic equations and the model configurations we used.

2.1   Overview of UCLA LES Model

The anelastic LES equations (1.11) are integrated using the UCLA LES model [4]. This model is a finite difference code implemented on a staggered *Arakawa C* grid [20] (see Figure 2.1), which means that all velocities are staggered half a grid point up-grid from the thermal/pressure points. For example, the *w* velocities reside half a grid point above the thermal points, while the *u* velocities are half a grid point to the right of the thermal points.

The model uses fourth order centred finite differences for momentum advection. It is common to choose a fourth order discretization for the advective derivatives not for higher accuracy,

but instead to reduce phase speed errors [20]. Because of the staggering, this involves first interpolating the velocities to the thermal points using the 4th order interpolation scheme:

$$w_{j+1/2} = \frac{7}{12}(w_j + w_{j+1}) - \frac{1}{12}(w_{j-1} + w_{j+2}),$$

followed by a centred difference of two consecutive velocities (now at the thermal points). For example, computing the vertical derivative of w would look like:

$$\begin{aligned}
\frac{\partial w}{\partial z} &= \frac{w_{j+1/2} - w_{j-1/2}}{\Delta z} \\
&= \frac{\frac{7}{12}(w_j + w_{j+1}) - \frac{1}{12}(w_{j-1} + w_{j+2}) - \frac{7}{12}(w_{j-1} + w_j) + \frac{1}{12}(w_{j-2} + w_{j+1})}{\Delta z} \\
&= \frac{w_{j+2} + 8w_{j+1} - 8w_{j-1} + w_{j-2}}{12\Delta z},
\end{aligned}$$

which we can see does work out to a fourth order centred finite difference scheme. The velocities are then marched forward in time using the leapfrog method. Using the leapfrog time discretization for nonlinear differential equations results in a computational mode that can grow in time. To control this computational mode we apply a asselin filter [44, 2, 20]:

$$\bar{\theta}^n = \theta^n + \varepsilon(\theta^{n+1} - 2\theta^n + \theta^{n-1}),$$

where $\varepsilon = 0.1$. The second derivative finite difference term damps the high frequencies. Scalar advection is achieved using the Lax-Wendroff scheme [44, 2, 20]. For example in the case of vertical advection of potential temperature this scheme looks like:

$$\theta_j^{n+1} = \theta_j^n - [w_j(\frac{\Delta t}{2\Delta z})(\theta_{j+1}^n - \theta_{j-1}^n) - w_j^2\frac{\Delta t^2}{2\Delta z^2}(\theta_{j-1}^n - 2\theta_j^n + \theta_{j-1}^n) - \theta_j^n\frac{\Delta t}{\Delta z}(w_j - w_{j-1})].$$

Because the Lax-Wendroff scheme is known to result in oscillations at discontinuities, a flux limiter [44, 2, 20] is applied. This approach allows for second order spatial discretization for most of the domain, only switching to a lower order scheme when gradients become steep.

The pressure solver exploits horizontal periodicity and uses 2D discrete Fourier transforms. Specifically, the pressure is found by the projection method [10] which involves applying continuity to the momentum equation:

$$\frac{\partial}{\partial x_i}(\rho_0 c_p \Theta_0 \frac{\partial \bar{\pi}'}{\partial x_i}) = \left[\frac{\partial}{\partial x_i}\left(-\rho_0 \bar{u}_j \frac{\partial \bar{u}_i}{\partial x_j} + \rho_0 \frac{g\bar{\theta}'}{\Theta_0} + \frac{\partial(\rho_0 \bar{\tau}_{ij})}{\partial x_j}\right)\right]. \tag{2.1}$$

This results in a one dimensional equation for every horizontal wave vector,

$$\frac{d^2\hat{\bar{\pi}}'}{dz^2} - (k^2 + l^2)\hat{\bar{\pi}}' = \hat{f},$$

where $\hat{f}$ is the just the horizontal Fourier transform of the rhs of (2.1), which is evaluated with a tridiagonal solver.

Horizontal boundary conditions are periodic. Vertical boundary conditions are no-normal-flow at the upper and lower boundaries, along with zero Neumann conditions on the scalars, i.e. temperature and total mixing ratio. These boundary conditions are enforced by an odd (no-normal flow) or even (Neumann) extension of the grid. For example, the Neumann condition of the u velocity would look like $u(x,y,-\Delta z/2) = u(x,y,\Delta z/2)$. Because we do not specify the momentum fluxes they are instead determined from Monin-Obukhov similarity theory as described in the previous chapter. This gives the eddy-viscosity on the bottom boundary as:

$$K_M = \kappa z \frac{u_*}{\phi(\zeta)},$$

where the friction velocity, u^* is determined from the law of the wall equation for the mean velocity within the surface layer [11]:

$$U = \frac{u_*}{\kappa} ln(z).$$

This mean velocity, U, is just the mean of $u^2 + v^2$ at the bottom slice of the domain and the dimensionless scaling functions, ϕ, are given by [8]:

$$\phi(\zeta) = (1 + 4.8\zeta) \quad \zeta > 0,$$
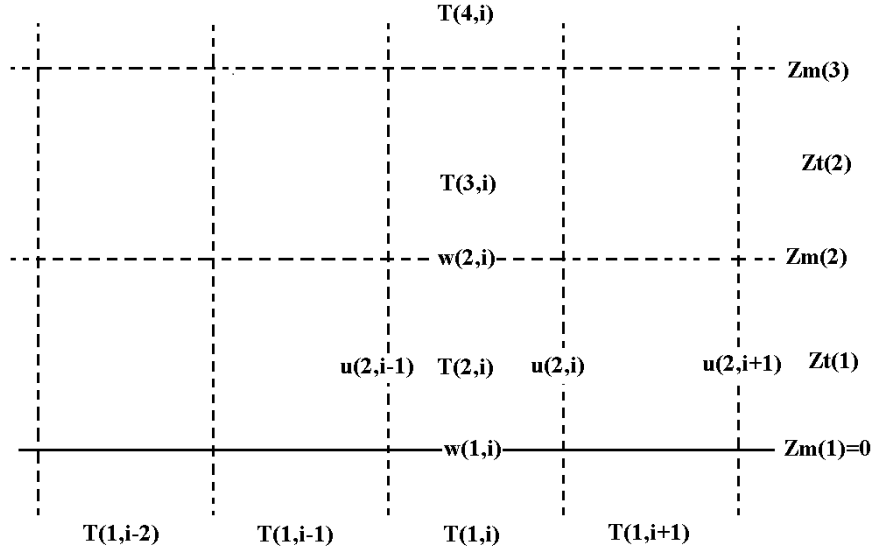$$\phi(\zeta) = (1 - 19.3\zeta)^{-1/4} \quad \zeta < 0.$$

Figure 2.1: Arakawa-C grid

The domain size is $L \times L \times H$, with $n \times n \times m$ grid points. In all simulations, the temperature flux Q_s and moisture flux Q_l are constant and are imposed through the SGS model. Different domain sizes, temperature and moisture fluxes, subsidence profiles, and initial conditions are chosen for the dry and moisture cases (see subsequent sections).

In order to compute profile statistics and spectra, which requires all model fields on a common grid, we use spectral interpolation in the horizontal, i.e. FFT's of $\hat{u}$ and $\hat{v}$ are taken at the staggered points and then corrected by multiplication by $e^{-ik(\frac{\Delta x}{2})}$ and $e^{-il(\frac{\Delta y}{2})}$ respectively. Derivatives in the transfer, dissipation, and pressure spectra are computed from the unstaggered fields spectrally in the horizontal and using fourth order finite differences in the vertical. Thus each term in the budget is calculated at order of accuracy at or above what is used in the underlying numerical model.

The UCLA LES code is written entirely in Fortran and uses the message passing interface (MPI) to accomplish a 2-dimensional parallelization. All simulations were run on the Shared Hierarchical Academic Research Network (SHARCNET), primarily on the orca cluster which is composed of a mixture of 24-core nodes using AMD Opteron @ 2.2GHz and 16-core nodes

Run	(L,H) [m]	(n,m)	(dx,dz) [m]	Q_s [Kms^{-1}]
B40	(5750,1990)	(144,50)	(40.2,40.6)	0.071
B20	(5750,1990)	(288,100)	(20.0,20.1)	0.071
B10	(5750,1990)	(576,200)	(10.0,10.0)	0.071
B5	(5750,1990)	(1152,400)	(5.0,5.0)	0.071
H40	(5750,1990)	(144,50)	(40.2,40.6)	0.142
H20	(5750,1990)	(288,100)	(20.0,20.1)	0.142
H10	(5750,1990)	(576,200)	(10.0,10.0)	0.142
D80	(11500,1990)	(144,50)	(80.4,40.6)	0.071
D40	(11500,1990)	(288,100)	(40.7,20.1)	0.071
D20	(11500,1990)	(576,200)	(20.0,10.0)	0.071

Table 2.1: Domain size, number of grid points, grid spacings, and surface heating strength for each numerical experiment.

using Intel Xeon @ 2.6GHz CPU's. Because the nodes are not dedicated (i.e. resources were shared with other jobs), timing results were not reliable and so were not included.

2.2   Dry and Moist Convective Boundary Layer Simulations

For the dry case we consider domain sizes, resolutions, and constant surface heating strengths shown in Table 2.1. These 10 simulations are separated into three problem configurations: the B* (where * is the approximate grid spacing in meters) represents the base case setup, the H* simulations represent the higher surface heat experiments, while the D* experiments indicate the larger domain setup. The initial potential temperature, subsidence, and radiative cooling profiles are shown in Figure 2.2. A constant $\Theta = 300$ K was also chosen.

Most simulations are run to 12000 s, with outputs every 1000 s. Simulations reach statistical stationarity after approximately 4000 s, and various quantities including the energy spectra and spectral budget terms are averaged from 4000 to 12000 s. The highest-resolution simulation (B5) is only integrated to 7500 s with outputs at 500 s intervals. This high resolution experiment took over one month in simulation time to complete.

For the moist simulations we follow a setup very similar to [22]. We consider domain sizes, resolutions, constant surface heating flux, and constant moisture flux shown in Table 2.2. Here a constant $\Theta_0 = 298.7$ was chosen.
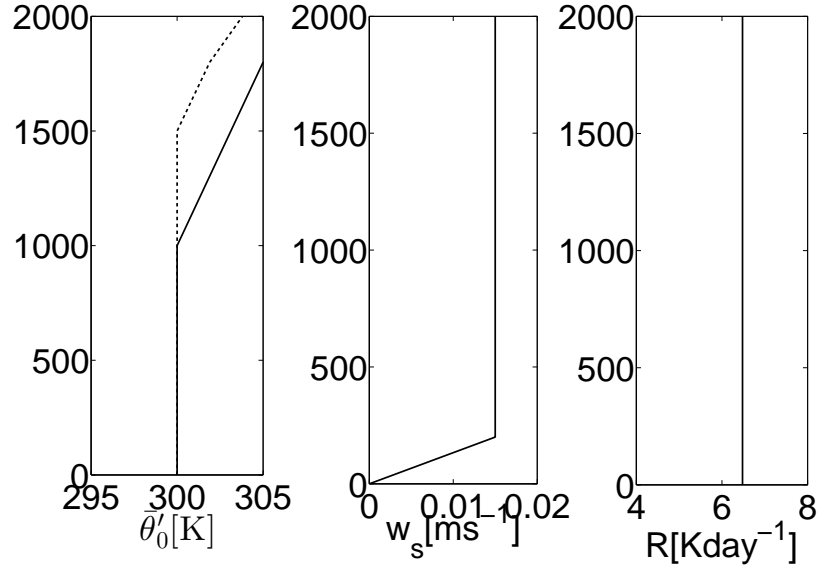
44

Figure 2.2: Initial θ_0, subsidence, and radiative cooling profiles. The dashed line corresponds to experiments with a higher surface heat flux. The vertical axis is in metres. These profiles follow [19]

The subsidence, radiative cooling, and initial potential temperature and initial mixing ratio are shown in Figure 2.3 [22]. The primary difference between the dry and moist cases is the inclusion of the water vapour mixing ratio (see below) as an active scalar. This not only effects the buoyancy, as moist air is less dense than dry air, but it also allows for the possibility of condensation (releasing latent heat) and the formation of clouds. The moist experiments were run up to 30000 s, except for M10 which was only run to 25000 s, and all profiles and spectra were computed by averaging between 21000-30000(25000).

Run	(L,H) [m]	(n,m)	(dx,dz) [m]	Q_s [Kms^{-1}]	Q_l [ms^{-1}]
M80	(5750,3000)	(72,38)	(80.1,81)	0.008	0.000052
M40	(5750,3000)	(144,75)	(40.2,40.6)	0.008	0.000052
M20	(5750,3000)	(288,150)	(20.0,20.1)	0.008	0.000052
M10	(5750,3000)	(576,300)	(10.0,20.1)	0.008	0.000052

Table 2.2: Domain size, number of grid points, grid spacings, surface heating strength, and moisture flux for each numerical experiment.
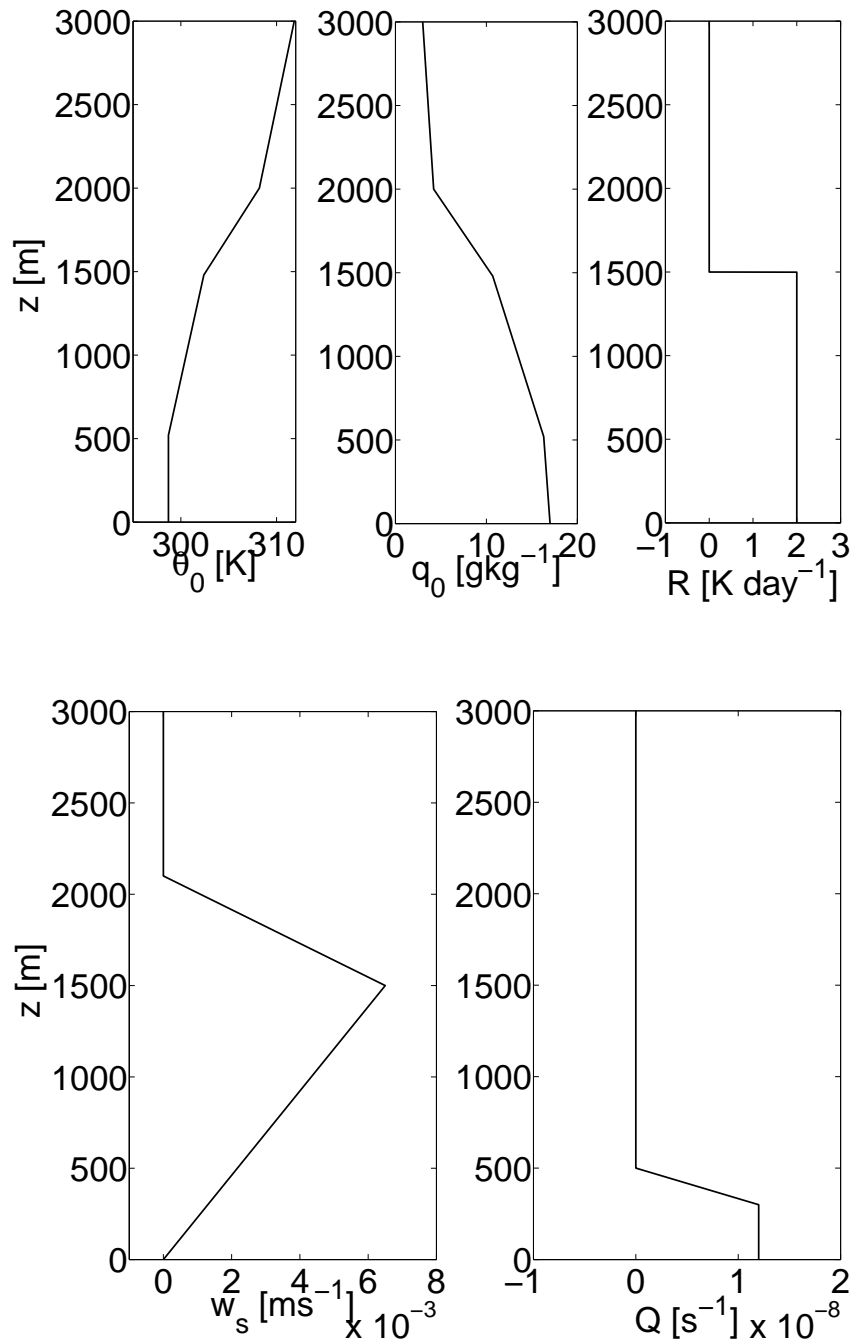
Figure 2.3: Top: initial θ_0, initial total mixing ratio, and radiative cooling profiles. Bottom: subsidence velocity and moisture decrease. These profiles follow [22]

47

Chapter 3

Results

3.1 Dry Boundary Layer Results

3.1.1 Overview

To investigate a spectral kinetic energy budget that is approximately stationary we run each simulation up to statistical stationarity as determined from time series of the volume mean kinetic energy:

$$K = \frac{1}{d} \int_0^d \frac{1}{2} \langle (\bar{u}^2 + \bar{v}^2 + \bar{w}^2) \rangle \, dz,$$

where $\langle \rangle$ denotes horizontal average. The time series for experiments B40-B5 are show in Figure 3.1. The flow has reached approximate stationarity by 4000 s. Vertical profiles of horizontally averaged potential temperature and heat flux are plotted in Figure 3.2(a,b). The results show nearly identical potential temperature profiles, which implies that the equilibrium potential temperature structure is independent of resolution. The heat flux profiles differ between resolutions only in the entrainment layer and the surface layer, where increased resolution causes sharper

48

adjustment between adjacent layers. Velocity variance profiles are shown in Figure 3.2(c,d): the vertical velocity variance is largest within the mixing layer, while the horizontal variance has peaks within the entrainment zone and the surface layer. Interestingly, the horizontal variance shows significant dependence on resolution, not just in the entrainment and surface layers, but also within the mixing layer, but the profiles appear to be converging with increasing resolution. A discrepancy exists in the plots of vertical and horizontal velocity variances where for increasing resolution (runs B40, B20, & B10) the variances increase slightly while for the highest resolution (run B5) there is an unexpected decrease. This may be caused by the fact that the highest resolution was only averaged up to 7500 s instead of the full 12000 s. However, other studies [68, 49] have also shown significant scatter rather than a monotonic increase in the mixing layer velocity variances as resolution is increased.

Overall, a high degree of convergence is seen in all the plots and the shapes of these statistics are consistent with previous studies of dry convective boundary layers [53, 68, 30, 49]. Statistics for the larger domain size and larger surface heat flux experiments have similar profiles are not shown. Potential temperature profiles from the simulations with higher surface heat flux are shown in Figure 3.3. The effect of increased Q_s on the boundary layer thickness from approximately 1100 m and 1600 m is clearly visible.

Figure 3.4 shows vertical slices of the model fields at the final time of the highest resolution run B5. The corresponding heat flux is shown in Figure 3.5. By this time the boundary layer height has reached its equilibrium level and a balance has been achieved between the surface heating, radiative cooling, and subsidence. Several rising plumes can be seen with positive potential temperature perturbations. Additionally, plume cores exhibit strong positive vertical velocity and positive heat flux. Outside these plume cores, but still within the plume structure, there exist regions of positive temperature perturbations and negative vertical velocity corresponding to negative vertical heat flux. These regions of negative heat flux are likely the result of the highly turbulent mixing that the plumes generate, particularly on their outer shell. Often the plumes may extend the entire boundary layer depth and may even penetrate into the stable layer resulting in sharp potential temperature changes at the plume/stable layer interface [64]. To the side of these penetrating plumes near the boundary layer height, warm air is often seen being pulled downward into the mixing layer as is most clearly seen in an animation of the potential temperature perturbation [64]. Well within the mixing layer, the plumes themselves are separated by large regions of sinking air (Figure 3.5). Generally within the mixing layer these regions correspond to cooler sinking air (positive vertical heat flux), but as we approach the entrainment layer there exists regions of hotter sinking air (negative vertical heat flux). Finally both horizontal velocities (*u* and *v*) exhibit equally sized regions of positive and negative velocities. No significant difference is observed between the *u* and *v* velocities which is consistent with the lack of background shear.
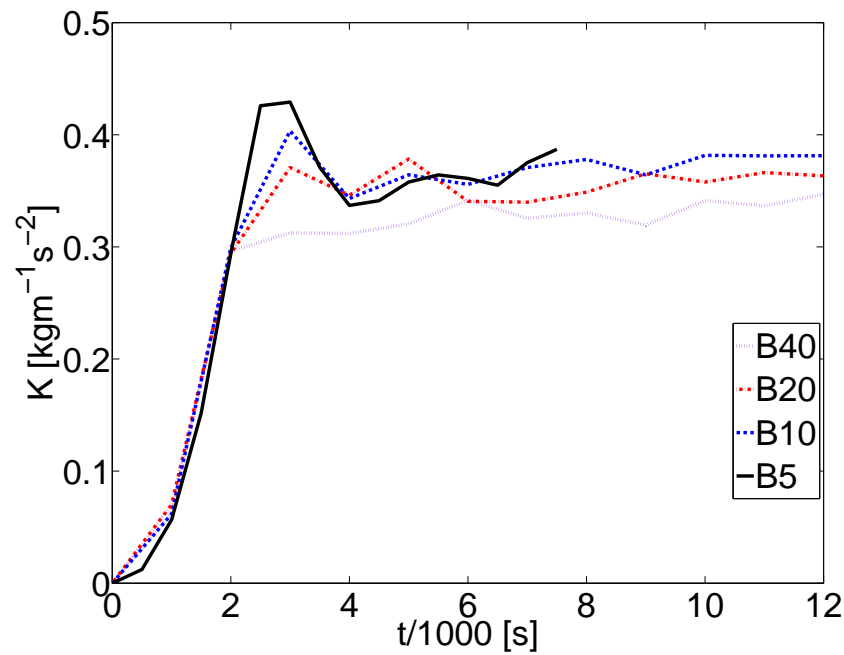
Figure 3.1: Time series of volume mean kinetic energy for experiments B40-B5.

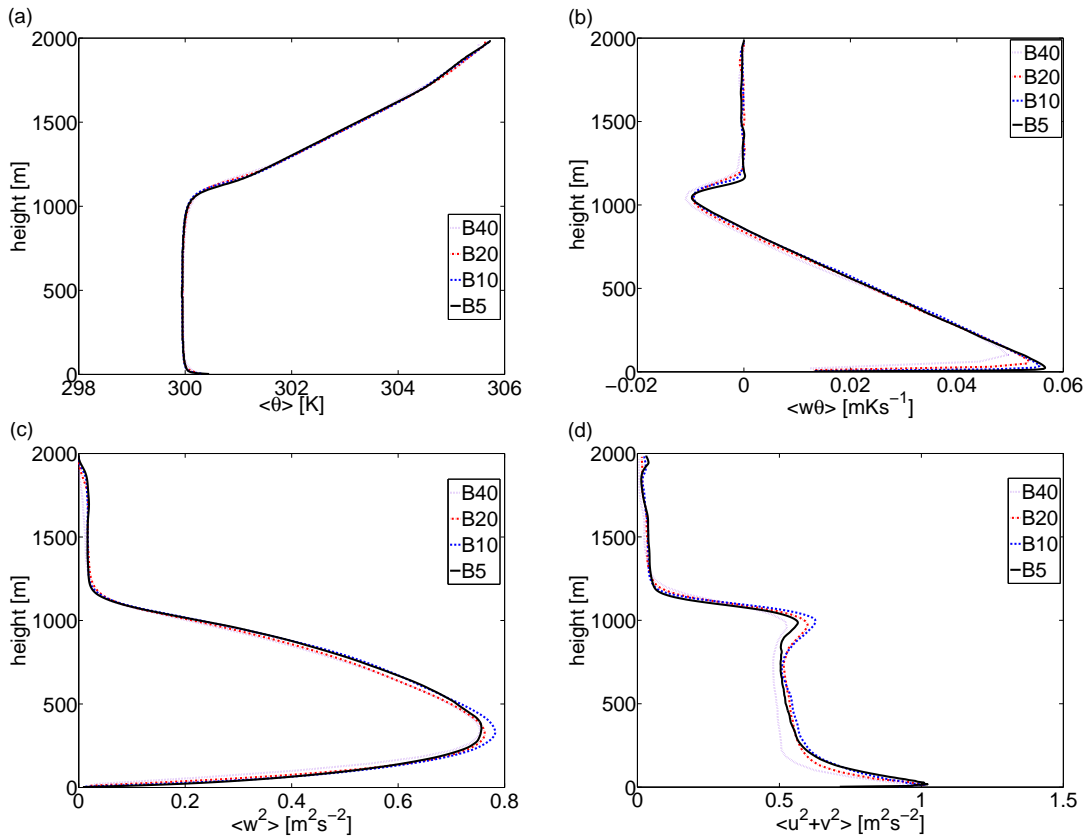Figure 3.2: Horizontally and time averaged (a) potential temperature, (b) heat flux, (c) vertical velocity variance, and (d) horizontal velocity variance for experiments B40-B5.
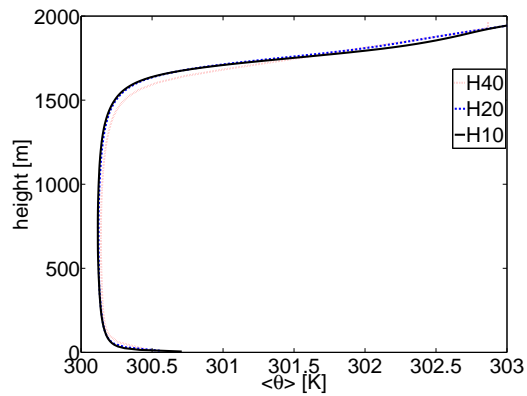

Figure 3.3: Horizontally averaged potential temperature for experiments H40-H10.
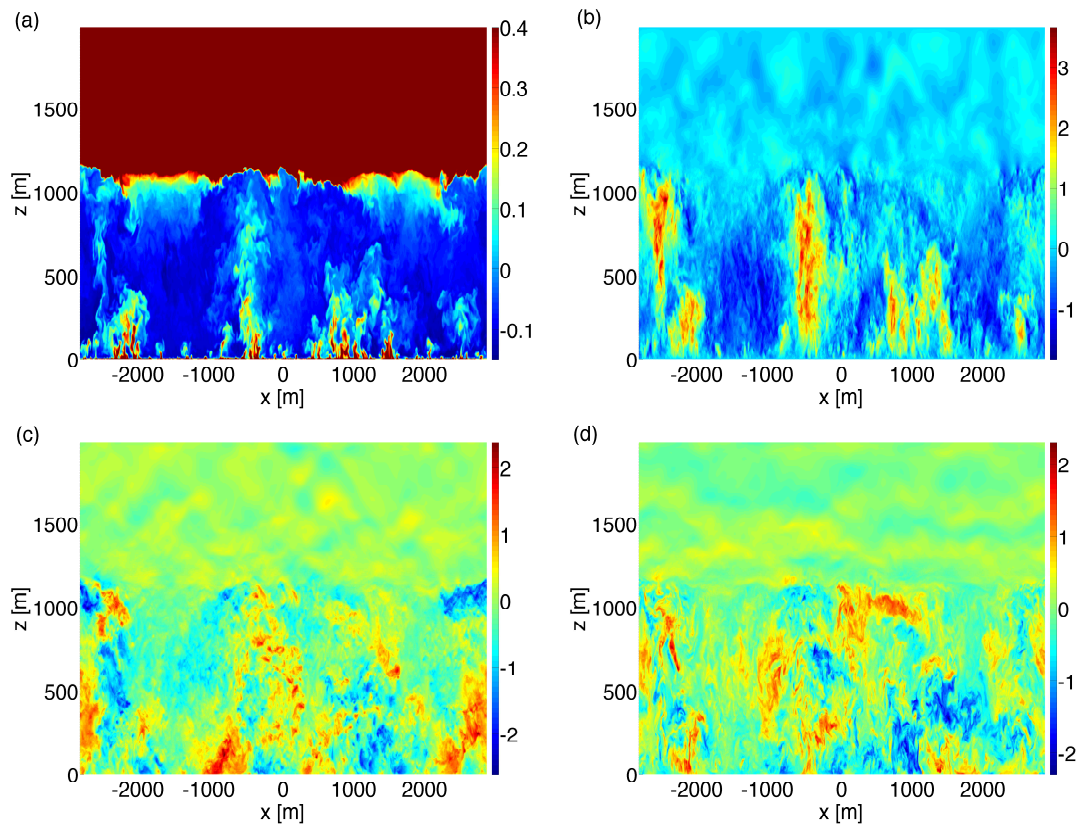
Figure 3.4: Vertical (x-z) slices of (a) θ', (b) w, (c) u, and (d) v taken at $y = 0$ m and time 12000 s for experiment B5.
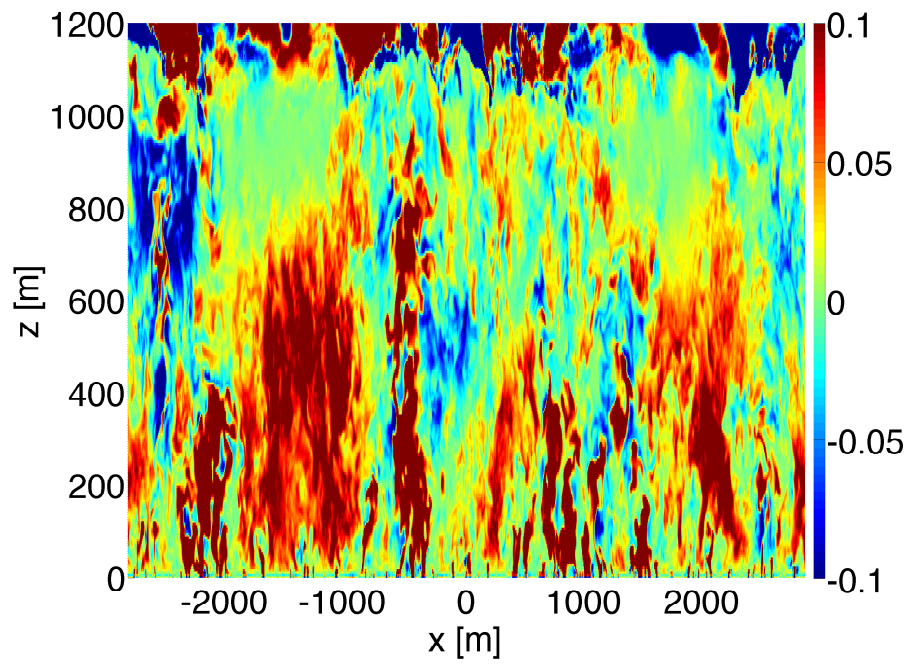
Figure 3.5: x-z slice of vertical heat flux, $w\theta'$, at $y = 0$ m and time 12000 s for run B5

3.1.2 Spectral Budget

Heat Flux

Of the various terms in the spectral KE budget, we consider first the heat flux $B(k,z)$, which plays a key role as the source of KE in the CBL. We have shown above that the averaged physical space statistics, i.e. the velocity variances and heat flux, match what has been seen in numerous other LES studies. In particular the physical space heat flux profile appears to have almost completely converged for run B5 which might mean that run B5 is sufficiently resolved. However, an important question is whether the spectral quantities exhibit similar convergence. Indeed, if the heat flux spectrum has a broad and resolution-dependent contribution from intermediate and small scales, this could have implications for the development of a locally isotropic inertial range.

Heat flux spectra from run B5 at different vertical levels are shown in Figure 3.6 (spectra are labeled with wavelength $\lambda = 2\pi/k$ along the x axis for clarity). As expected the heat flux near the surface is positive and peaked at large wavenumber implying a small scale injection of KE [32, 64, 34]. Moving up through the mixing layer the spectrum remains positive but the peak shifts to larger scales [32, 64, 34]. This transition of the maximum heat flux from smaller scales to larger scales as one moves up through the mixing layer is consistent with horizontal slices of potential temperature and heat flux (Figure 3.7). Near the surface, heating causes the formation of fine filamentary structures reminiscent of the honeycomb patterns seen in Rayleigh-Bernard flows. Well within the mixing layer, however, large-scale thermal plumes have formed with diameters around 100-500 m which are associated with the larger scale heat flux. At higher levels near the entrainment zone strong negative values of the heat flux are obtained at large scales corresponding to the downward movement of warmer stably stratified air being pulled into the mixing layer.

The peaks of positive flux transition from small scales in the surface layer to large scales in the mixing layer. This transition occurs rapidly with increasing height, suggesting that the surface layer occupies only the bottom $O(10)$ m and that the large-scale thermal plumes begin forming at a height relatively close to the surface. This surface layer however is likely not resolved by the Smagorinsky parameterization and its detailed structure requires further fine resolution experiments beyond the scope of the current study. Within the mixing layer, the location of the peak positive flux was found to remain approximately constant around $\lambda \sim 1150$ m for all the base case experiments (B40-B5) and the larger domain sized experiments (D80-D20). There is, however, a shift in the peaks to larger scales for the case of stronger surface heating (runs H40, H20, and H10). This is not surprising as the peak follows the scale of the boundary layer depth and the higher surface heating experiments naturally result in deeper boundary layers. Once the boundary layer height is reached, the peaks in positive flux move to small scales again where
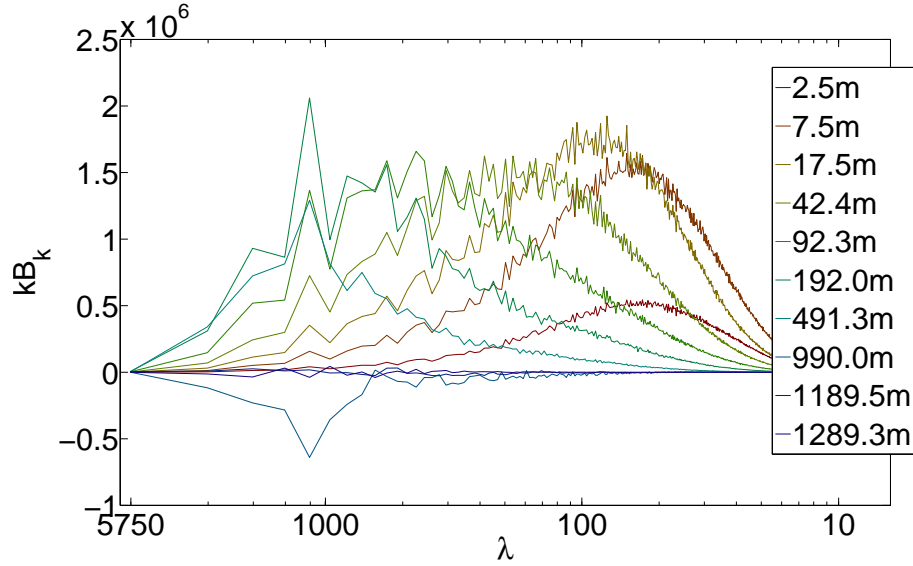
Figure 3.6: Time averaged horizontal heat flux spectra at different height levels for run B5. Spectra have been multiplied by k_h to preserve area on the log-linear plot.

they do not inject a significant amount of energy in the entrainment layer.

While the large scale injection of kinetic energy by positive heat flux appears to remain approximately independent of resolution and domain size and only moves to large scales for the higher surface heating, the contribution from small scales is more sensitive; such small-scale forcing could have implications for the existence of an inertial range removed from the forcing, since it could signify injection of KE over a broad range of scales, possibly down to the LES dissipation scale. In order to compare the heat spectra of different resolutions, we plot them together in Figure 3.8 averaged over the depth of the domain. These spectra are consistently broadening as resolution increases. This broadening also holds for the larger domain experiments as well as the larger surface heating experiments. On the other hand, the large scale contributions appear to remain relatively independent of resolution. These heat flux spectra do appear to exhibit a saw-tooth pattern in the large scales, which seems to be an artifact of the binning over annuli on the k_x-k_y plane.

We also compute the integral of the heat flux spectra as a function of wavenumber:

$$F_B(k) = \int_0^k B_k(k')dk', \tag{3.1}$$

55
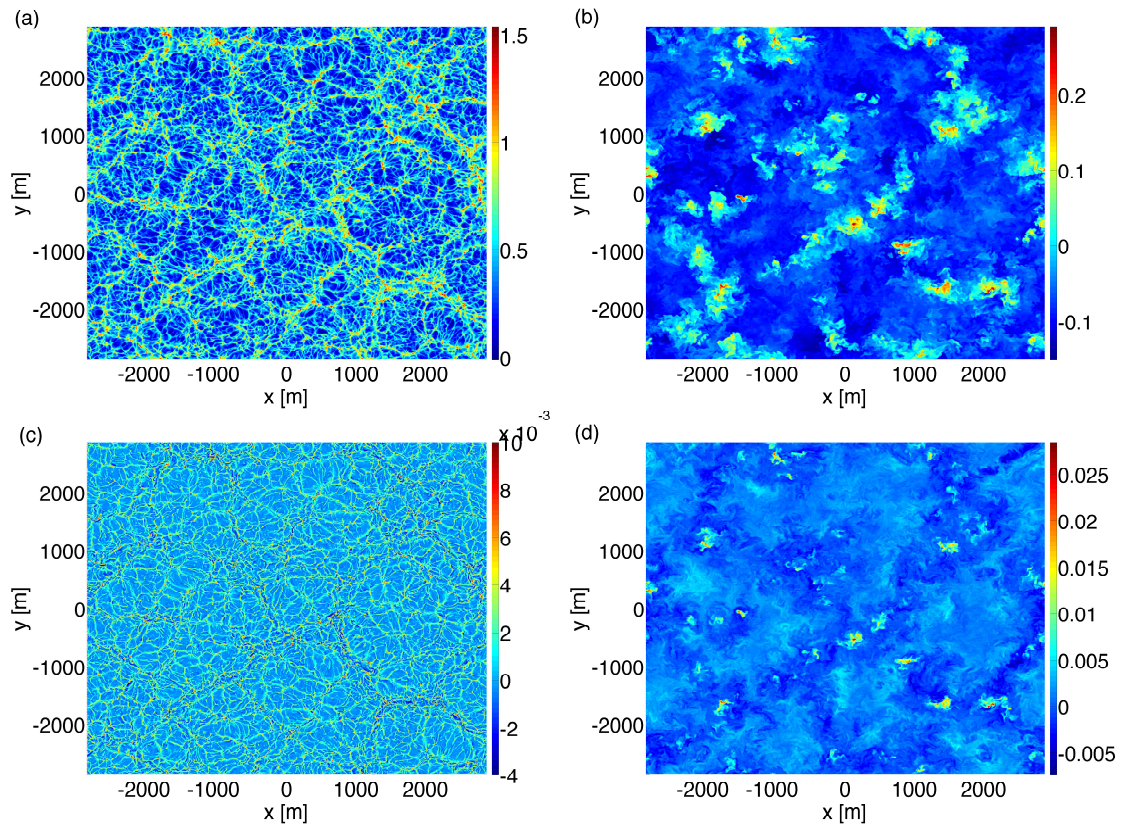
Figure 3.7: Horizontal (x-y) slices of $\bar{\theta}'$ at (a) $z = 2.5$ m, (b) $z = 501$ m, and of $\frac{g}{\Theta_0}\bar{w}\bar{\theta}'$ at (c) $z = 2.5$ m, (d) $z = 501$ m.
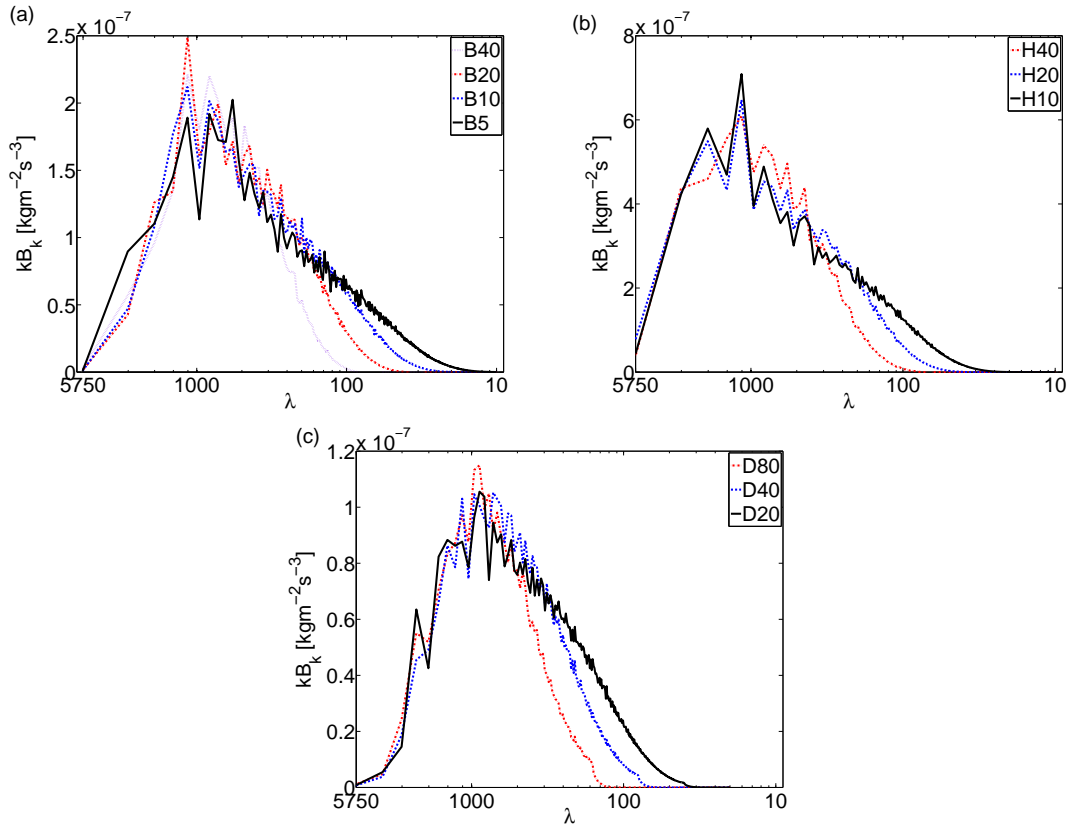
Figure 3.8: Time averaged heat flux spectra averaged over the boundary layer depth for (a) the base runs B40-B5, (b) the enhanced surface heat flux runs H40-H10, and (c) the large domain runs D80-D20. Spectra have been multiplied by k_h to preserve area on the log-linear plot. For the larger domain runs we have restricted the λ axis to 5750 m for better comparison with the base case experiments.

Figure 3.9: Integrated heat flux $F_B(k)$ for all runs. I, II, and, III, mark out the points at which the interated heat flux has converged for successive increases in resolution. Other details are as in Figure 3.8.

58

Figure 3.10: (a) Time-averaged heat flux spectra averaged throughout mixing layer ($z = 200 - 800$ m) for runs B40-B5. Spectra have been multiplied by k_h to preserve area on the log-linear plot. (b) $F_B(k)$ within mixing layer for runs B40-B5.

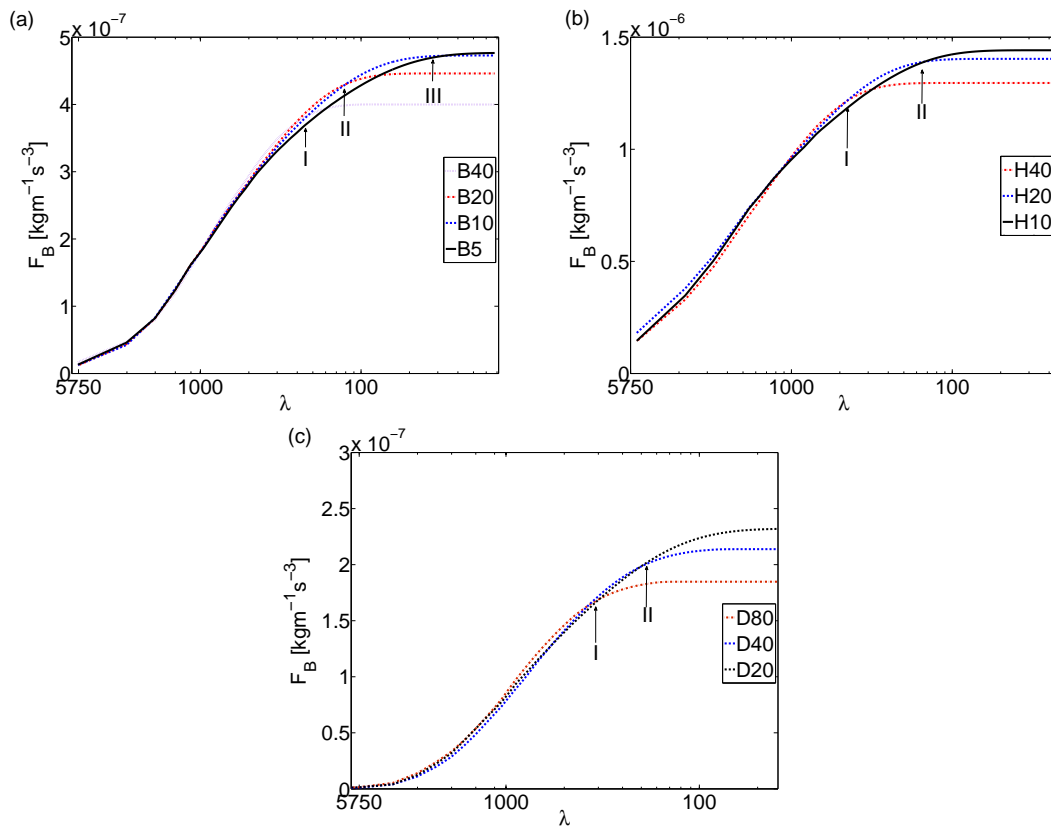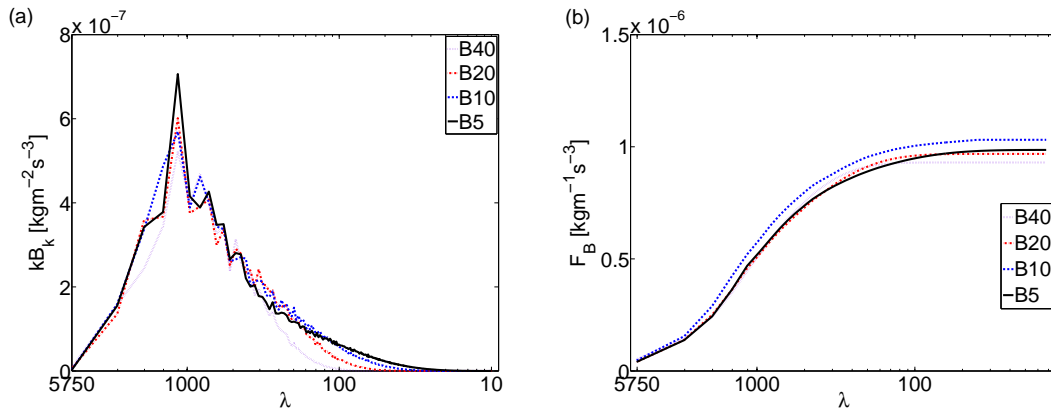which gives the contribution to the total injection rate of KE from heat flux from wavenumbers less than k. The integral of the vertically averaged heat flux spectra is shown in Figure 3.9. As the resolution increases, $F_B(k)$ is seen to converge at small scales. Consider the B runs in Figure 3.9(a): the wavenumber below which $F_B(k)$ has converged with resolution (marked by *I*, *II*, & *III*) moves further to the right as resolution increases. For example, as Δx is decreased from 20 m to 10 m, there is a 6% increase in the total wavenumber-integrated heat flux. Figures 3.8 and 3.9 indicate that the heat flux spectrum, while peaked at large scales, has a positive contribution over a broad range of scales; fine grid spacings of $\Delta x \sim 5$ m are required for the total wavenumber-integrated heat flux to converge.

It is possible that the small-scale heat flux contribution is caused solely by the surface layer where small scale convective motions are most likely to occur, given that most of the contribution to the heat flux spectrum in the surface layer is at small scales (see Figure 3.6). To investigate this, we plot the heat flux spectra averaged over the mixing layer ($z = 200 - 800$ m; see Figure 3.10) and surface layer ($z = 0 - 100$ m; see Figure 3.11). It is clear that a rightward shift in B_k to smaller scales with increased resolution exists for both regions; however, the shift is significantly smaller for the mixing layer than for the surface layer. Near the surface a combination of diffusion and small scale convective motions transports the surface heat into the overlying air. Thus by increasing resolution, we are resolving these features more fully and hence capturing them in the surface layer heat flux spectra. By contrast, the mixing layer heat flux is dominated by larger structures and is more robust to changes in resolution.
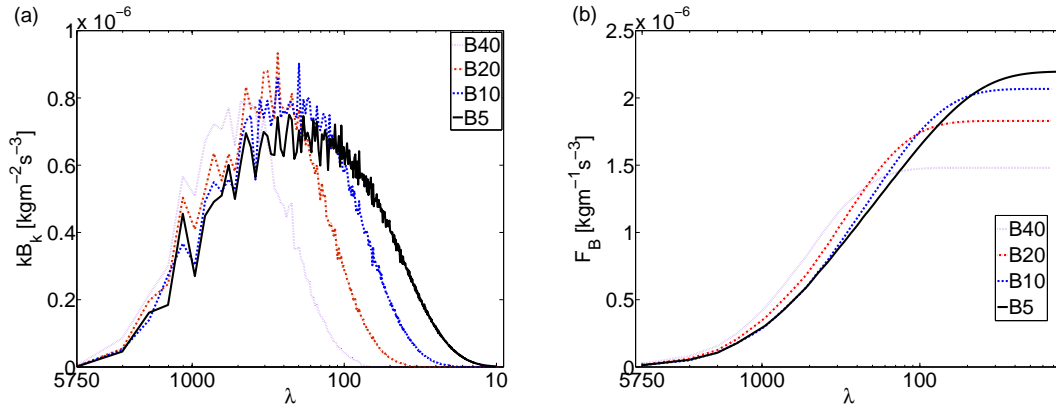
Figure 3.11: (a) Time-averaged heat flux spectra averaged throughout surface layer ($z = 0 - 100$ m) for runs B40-B5. Spectra have been multiplied by k_h to preserve area on the log-linear plot. (b) $F_B(k)$ within surface layer for runs B40-B5.

Transfer, Dissipation, & Pressure

The remaining terms in the spectral kinetic energy budget for the base case experiments are plotted in Figure 3.12, while the budgets for the highest resolution experiments B5, H10, and D20 are shown in Figure 3.13. The transfer, pressure, and dissipation spectra are all plotted on the same axis (along with the heat flux spectra discussed in section 3.2.1) in order to highlight the relative strength, and related large and small scale features, of each term within a statistically stationary CBL. Each term in the budget extends to a maximum horizontal wavenumber of $k_{max} = \pi/\Delta x$, and so with each successive increase in resolution the spectra are extended to smaller scales.

The role of each term in the budget is evident from the evolution equation of the kinetic energy spectrum (1.35). When the time rate of change of the spectral kinetic energy is zero (as is approximately the case for time-averaged spectra in a statistically stationary boundary layer), the heat flux (B_k), transfer (T_k), pressure (P_k), and dissipation (D_k) spectra must balance. In each plot we see that energy is injected over a rather broad range of scales, but most significantly at larger scales, by the heat flux spectra as was previously discussed. Energy is then removed from the relatively large scale region (negative transfer spectra), and injected into the small scales (positive transfer spectra). Once transferred, the energy at small scales is dissipated by the LES model through the eddy viscosity parameterization of the SGS fluxes at large wavenumbers (negative dissipation spectra), as expected for a downscale energy cascade.

We have also included plots showing the transfer and dissipation spectra at different heights

60

Figure 3.12: Time averaged terms in the spectral budget, averaged in *z* over the boundary layer depth, for runs (a) B40, (b) B20, (c) B10, and (d) B5.
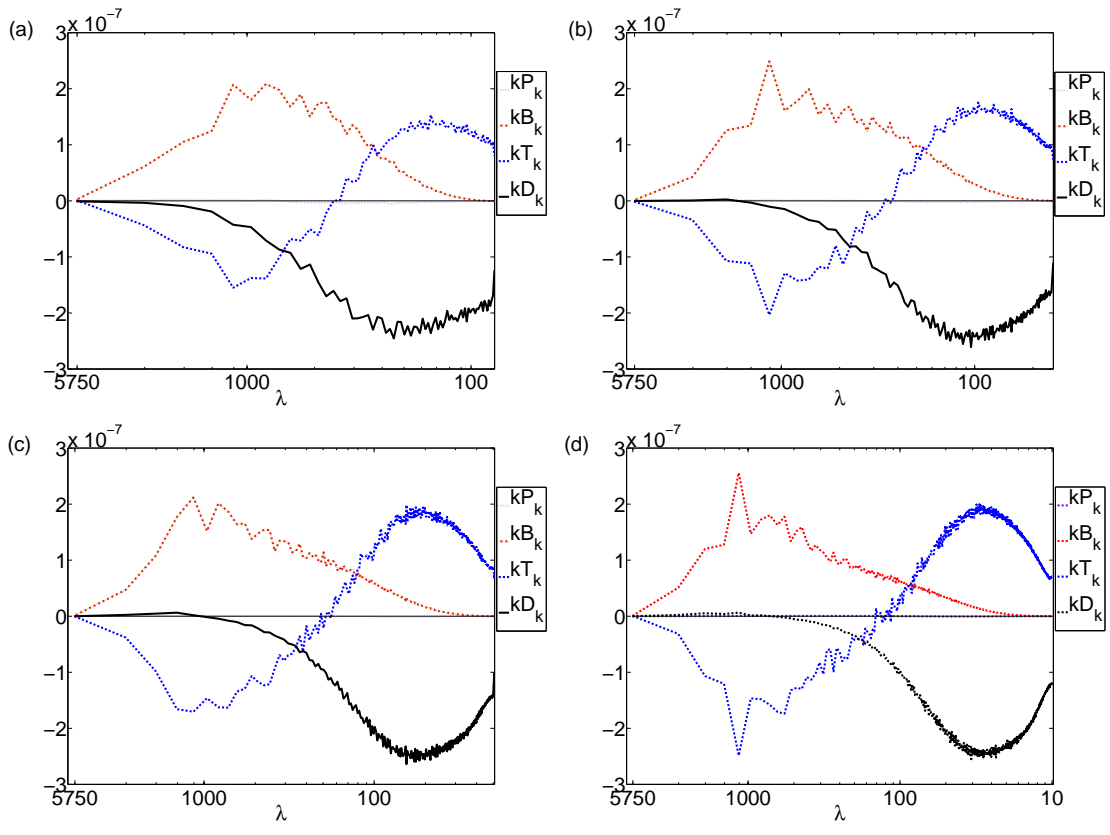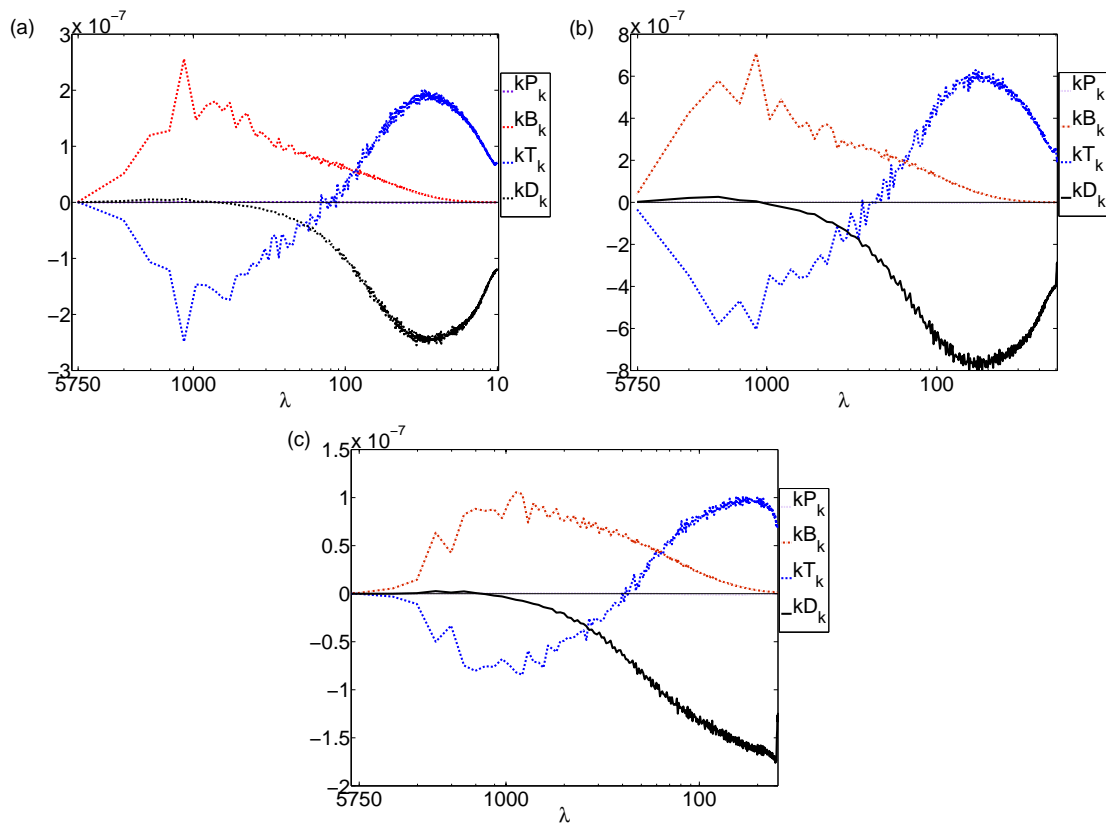
Figure 3.13: Time averaged terms in the spectral KE budget, averaged in z over the boundary layer depth, for runs (a) B5, (b) H10, and (c) D20. For the larger domain run we have restricted the λ axis to 5750 m for better comparison with the base case experiments.
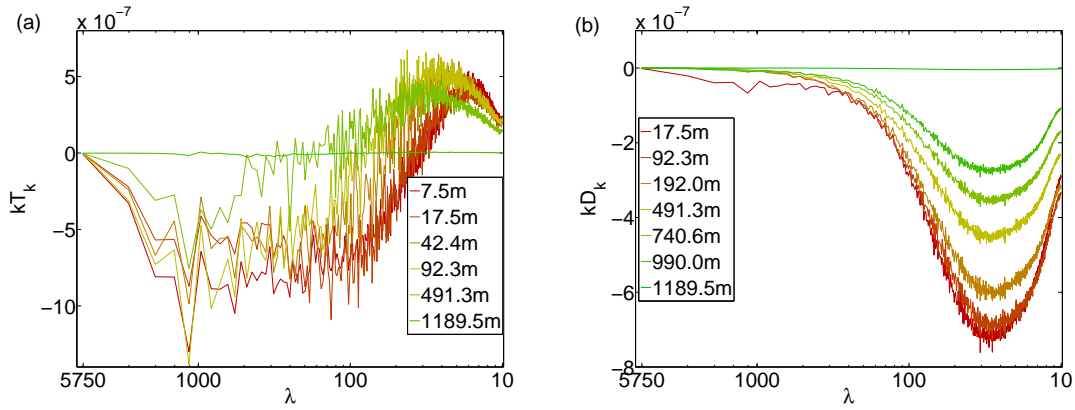
Figure 3.14: (a) Time averaged horizontal transfer spectra at different levels for run B5. (b) Time averaged horizontal dissipation spectra at different levels for run B5. Spectra have been multiplied by k_h to preserve area on the log-linear plot.

(Figure 3.14). The transfer generally shows a cascade from large scales to small scales consistent with the domain averaged spectra. The dissipation spectra also show a similar profile to the domain averaged plots, except that we can see that this spectra is strongest within the first 500 m where the thermal plumes are developing. As we move through the mixing layer the strength of the dissipation decreases until we reach the boundary layer height at which point the dissipation turns off. This is consistent with the fact that the eddy viscosity becomes zero within the stable layer for the Smagorinsky model.

The vertically integrated pressure spectrum is approximately zero in all cases, as expected since $w = 0$ at the upper and lower boundaries (1.36). The small deviations from 0 arise as a result of the interpolation of variables to the thermal points which results in small errors. We have confirmed that these small errors decrease as resolution is increased. The pressure perturbation spectrum at a given horizontal slice is not zero, and in fact may be rather large near the surface where strong surface heating and large vertical w velocity gradients exist (not shown).

In all cases, the large-scale transfer spectra and heat flux spectra are in balance, consistent with the statistical stationarity of the boundary layer over the averaging interval. The higher surface heat flux experiments (Figure 3.13 b) have large-scale heat flux and transfer spectra with magnitudes approximately twice that of their lower surface heat flux counterparts, in line with the stronger forcing of these runs. In the case of the larger domain (Figure 3.13 c) the wavenumber axis extends further to the left (larger-scales); however the heat flux and transfer spectra remain approximately unchanged from the smaller domain case, implying that the budget is insensitive to domain size. Thus increasing the domain size does not result in the organization of larger-
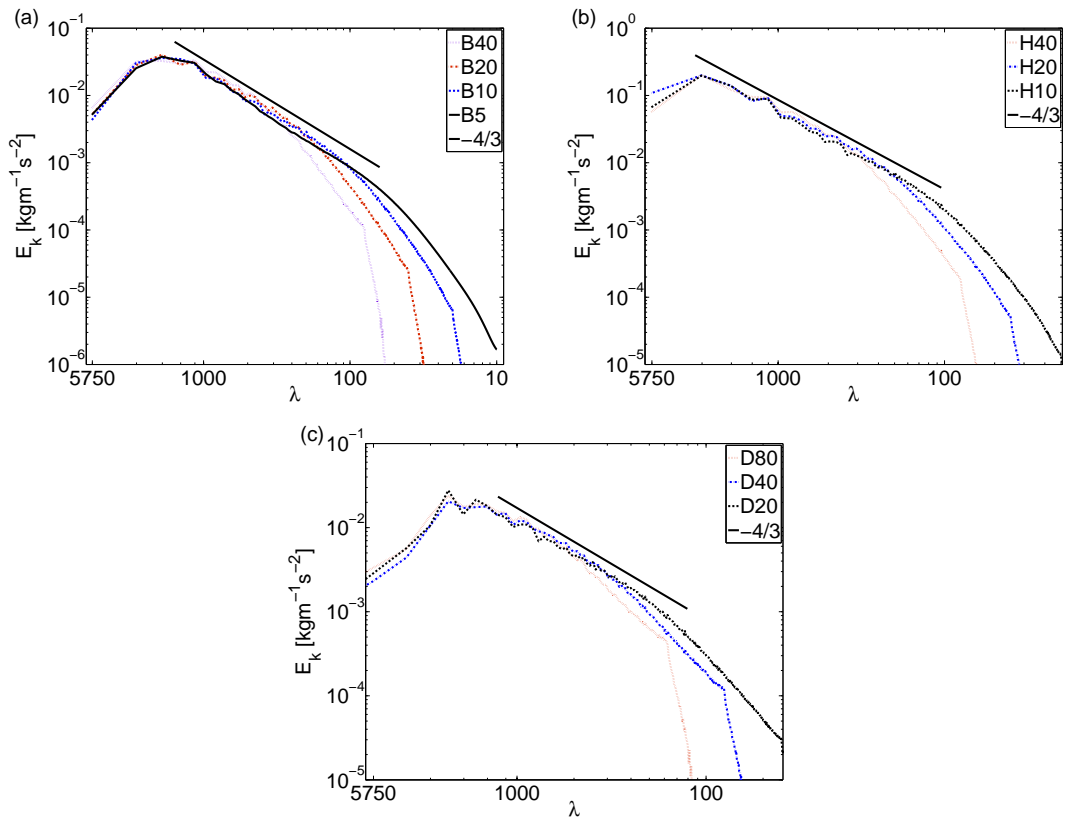
63

Figure 3.15: Time averaged KE spectra, averaged in *z* over the depth of the boundary layer, for (a) the base runs, (b) the enhanced surface heat flux runs, and (c) the larger domain runs, all at different resolutions.

scale features within the flow in a significant way as might be expected in simulations with strong background rotation (e.g. [26]) or as has been seen in temperature spectra (e.g. [29]) and experiments involving moisture (e.g. [62]).

The spectral budget at small scales is dominated by the dissipation; however, it is significant that in all experiments there is broad overlap between the heat flux and dissipation spectra. This overlap follows from the fact that, as discussed above, the heat flux spectrum is very broad and extends to smaller scales as resolution is increased. Only in the highest resolution case (Figure 3.12 d) do we begin to reduce this overlap. As a result none of the experiments show a resolved inertial range of intermediate wavenumbers with approximately zero transfer. For more insight into the existence (or not) of an inertial range in these simulations, we compute the spectral flux:

$$\Pi_k = -\int_0^k T_k(k')dk'.$$

An inertial range corresponds to a range of k with constant spectral flux, and is a fundamental assumption in the derivation of the Kolmogorov -5/3 spectrum [11]. The spectral flux for experiments B40-B5 are shown in Figure 3.16. No inertial range emerges as resolution is increased; instead, the maximum spectral flux increases and shifts to smaller scales. This increase and shift is perhaps caused by the small-scale heat flux that develops as resolution increases and by the fact that increased resolution results in the dissipation spectra also moving to smaller and smaller scales. Thus the transfer spectra must make up the difference in the budget.

The kinetic energy spectra for each experiment are shown in Figure 3.15. Assuming KE spectra of the form:

$$y = e^a k_h^m,$$

we can use least squares to find a and m for regions where the spectra have approximately constant slope in the log-log plots (Table 3.1). All the experiments have KE spectra with slopes slightly shallower than $-5/3$. For the base case experiments and the higher surface heating experiments the KE slopes appear to be closer to $-4/3$. For the larger domain experiments the slopes appear to be slightly shallower then $-4/3$. For the experiments with higher surface heat flux, the spectra have a larger magnitude, in line with the stronger surface forcing. In all cases, the spectra peak at wavenumbers related to the boundary layer depth. In the SGS dissipation range at large k_h, the spectra become shallower as resolution is increased which indicates that the model becomes less dissipative as resolution is increased. In the previous section we saw that the heat flux spectrum injects significant energy over a wide range of scales throughout all

65
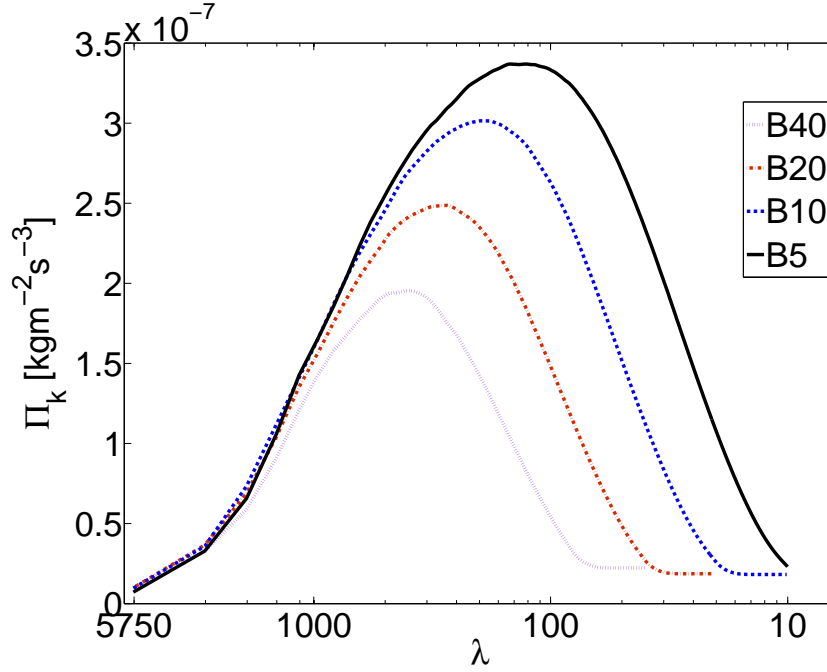
Figure 3.16: Spectral flux for experiments B40-B5.

Run	m	a	λ range
B40	-1.4549	-10.9464	$1150 < \lambda < 302.6$
B20	-1.3503	-10.6660	$1150 < \lambda < 198.3$
B10	-1.3410	-10.6494	$1150 < \lambda < 130.7$
B5	-1.4088	-11.0234	$1150 < \lambda < 83.3$
H40	-1.5837	-10.5009	$1150 < \lambda < 302.6$
H20	-1.4150	-9.9946	$1150 < \lambda < 198.3$
H10	-1.3697	-9.8427	$1150 < \lambda < 130.7$
D80	-1.3222	-10.6365	$1150 < \lambda < 575$
D40	-1.2931	-10.4577	$1150 < \lambda < 338.2$
D20	-1.2678	-10.8854	$1150 < \lambda < 250$
BTKE40	-1.3740	-10.9435	$1150 < \lambda < 302.6$
BTKE20	-1.3657	-10.9097	$1150 < \lambda < 198.3$

Table 3.1: Values of *a* and *m* computed by least squares assuming KE spectra have the form $y = e^a k_h^m$.

Figure 3.17: (a) Time averaged KE spectra at different levels for run B5. (b) Time averaged spectra of vertical KE at different levels for run B5.

the CBL layers. It is possible that this broad-scale forcing is responsible for these spectra being consistently shallower than the theoretic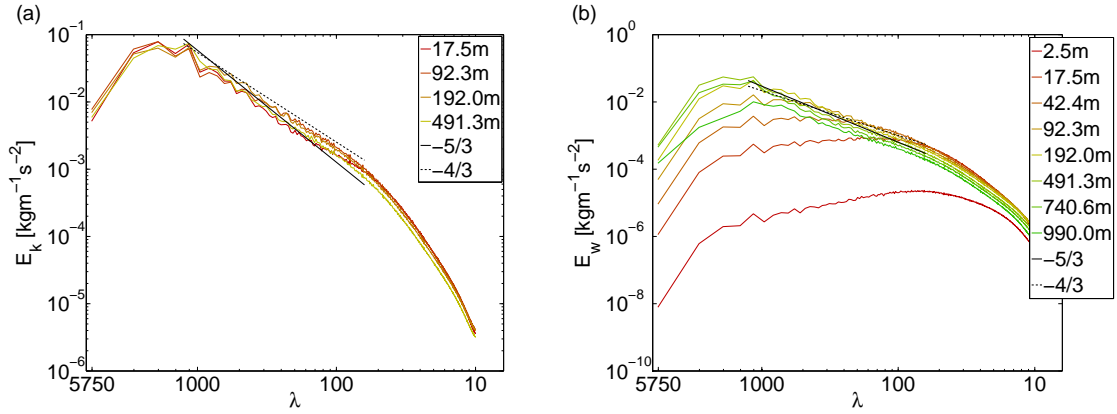al $-5/3$ power law. Surface layer effects may also be important here. In Figure 3.17 we show the KE spectra and the spectrum of vertical KE at different levels. For example, in computing the spectrum of vertical kinetic energy within the mixing layer we found that the slope more closely resembled a $-5/3$ scaling, consistent with [68], while the full KE spectra remain closer to $-4/3$.

The energy spectra in Figure 3.15 are clearly shallower than what we would expect for isotropic 3D turbulence. To investigate this discrepancy further, we consider whether local isotropy is emerging at small scales in the highest resolution cases. In isotropic turbulence, the ratio of one-dimensional transverse and longitudinal energy spectra (e.g. k_x spectra of KE in w and u) will attain a constant value near $4/3$ when local isotropy is reached [75]. Because we compute two-dimensional horizontal wavenumber spectra however, a modification of the $4/3$ isotropy condition is required. Defining the horizontal wavenumber spectra of horizontal and vertical KE over cylindrical wavenumber shells results in an isotropic vertical-to-horizontal ratio of approximately 0.57 (see Appendix). Of course, this theoretical ratio assumes a $-5/3$ spectrum; isotropic turbulence with a $-4/3$ spectrum would likely correspond to a slightly smaller ratio. We plot this ratio for experiments B40-B5 in Figure 3.18 (a). At large scales this ratio is larger than 1 and progressively moves lower as we transition to small scales indicating that within the large-scales the vertical motions are more energetic than the horizontal. In fact, increased resolution results in higher ratios at large-scales, suggesting that lower resolution simulations suppress the relative strength of the vertical KE. While the low resolution experiment B40 takes on a ratio that is roughly a constant value near 1 over all wavenumbers (although it
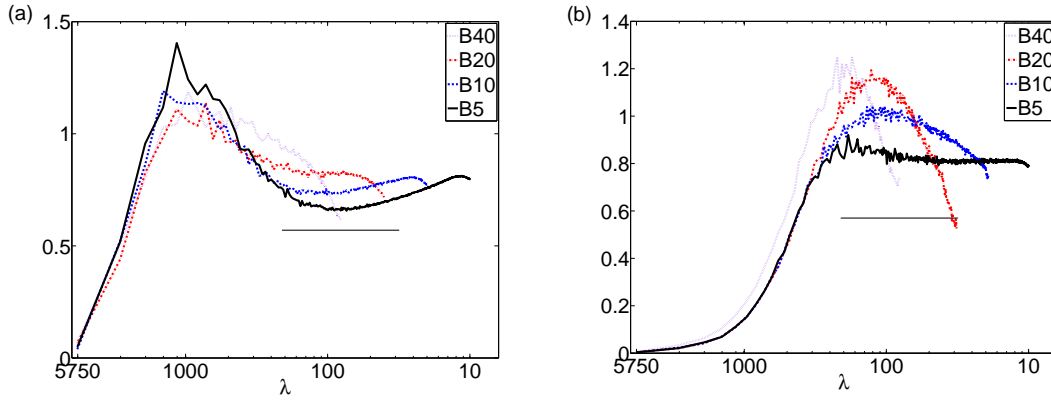
Figure 3.18: a) Ratio of vertical to horizontal kinetic energy spectra averaged in the vertical over whole domain, b) vertical-to-horizontal ratio of energy spectra averaged in the surface layer ($z = 0 - 100$ m)

does decrease below 1 as we move to smaller scales), the higher resolution experiments seem to form plateaus at successively smaller values below 1 as resolution is increased. For the highest resolution experiment this ratio is approximately equal to $0.65 - 0.70$ for λ in the range $30 - 160$ m. Thus with increasing resolution, the ratio might be approaching 0.57 from above. The finding that this ratio is generally larger than the theoretical value for isotropic turbulence agrees with previous results [51, 54, 64]. Finding spectral ratios of 0.57 is only a necessary condition of local isotropy, however these results suggest that local isotropy, if it emerges, would require grid spacings $< O(1)$ m.

In order to further investigate the effect of the surface heating on the energy spectra, we compare the spectral ratios restricted within the surface layer ($z = 0 - 100$ m). These results are shown in Figure 3.18 (b). Unlike in the domain-averaged case, the vertical-to-horizontal ratio does not show peaks in the large-scales indicating that the vertical energy spectra is much weaker than the horizontal energy spectra at these scales. This confirms that within the surface layer the vertical spectra remain energetic primarily in the small-scales and this property can also be seen in Figure 3.17. We have confirmed however that the horizontal spectra do peak at large scales. Thus within the surface layer the horizontal and vertical energy spectra differ significantly in the large-scales. Even for the highest resolution case, the ratio of vertical to horizontal KE is around 0.8, suggesting that the surface layer turbulence remains much more anisotropic than the mixed layer.

68

Sensitivity to SGS Parameterization

We have seen that the dissipation spectrum is shifted to small-scales as resolution is increased. An important question then is what effect do alternative subgrid-scale parameterizations have on the spectral KE budget; in particular do more sophisticated parameterizations result in less dissipation in the large scales and a greater shift in the peak dissipation to small scales for a given resolution? Previous studies (e.g. [23, 30]) have found that both physical space statistics and energy spectra were relatively robust to changes in the SGS parameterization. To investigate the SGS sensitivity of the current study, we re-run some of our experiments using the TKE model [17]. We solve the same equations as before (1.11), except that now the eddy-viscosity is changed to:

$$K_m = 0.1 l_m \sqrt{e}, \quad K_h = (1 + \frac{2 l_m}{l_n}) K_m,$$

where e is the turbulent kinetic energy and is found by solving an additional prognostic equation [17]. The subgrid-scale mixing length l_m, and the grid-scale l_n, are defined as:

$$l_m = \min{(0.82 \sqrt{\frac{e}{max(\varepsilon, N^2)}}, l_n)} \quad l_n = \sqrt{\frac{1}{(\frac{1}{\Delta x})^2 + (\frac{0.23}{z\kappa})^2}},$$

where $\varepsilon = 10^{-12}$. Thus K_h/K_m ranges between 1 and 3 and the SGS mixing length l_m is at most l_n, but can be much smaller in stably stratified regions. We run this model only for the experiments B40 and B20 and refer to the TKE runs as BTKE40 and BTKE20. The resulting spectral budget and KE spectra are shown in Figure 3.19(a,b).

A number of important conclusions can be derived from these results. Firstly, the dissipation spectrum is seen to peak at smaller scales with the TKE model than it did with the Smagorinsky model for a fixed resolution. In fact for the experiment BTKE20, the dissipation spectrum peaks at wavenumber close to where the highest resolution (B5) Smagorinsky dissipation spectrum peaked despite being a quarter of the resolution. Nevertheless, even for the TKE runs the heat flux spectrum remains quite broad and the transfer spectra still does not show any region of constant spectral flux (not shown). The decreased dissipation does however have an effect on the KE spectra by decreasing the slope within the SGS dissipation range. The approximately $-4/3$ slope for the KE spectra observed in the Smagorinsky model appear to remain unchanged when the TKE model is used indicating that this result is robust to changes in the SGS parameterization.
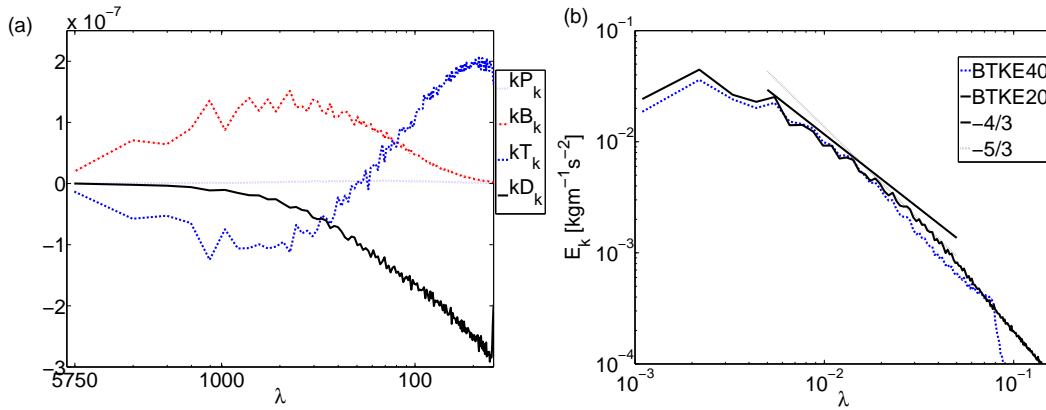
Figure 3.19: a) Spectral KE budget for BTKE20. b) KE spectra for BTKE40 and BTKE20.

3.2 Moist Boundary Layer Results

3.2.1 Overview

The moisture experiments closely resemble the setup of [22] which use subsidence, radiative cooling, surface heat and moisture fluxes, and an initial temperature profile that correspond to different atmospheric conditions from the dry experiment setup. Unlike the dry case however, the boundary layer does not reach stationarity as shown in Figure 3.20. We thus choose to run the moist simulations much longer (up to 30000 s instead of 12000 s) in order to ensure a fully developed boundary layer simulation that is not significantly affected by the initial conditions. Because of the added moisture and the subsequent cloud formation, we also include a time series plot showing the total cloud cover in Figure 3.20. Interestingly this total cloud cover does appear to stabilize after a few thousand seconds, despite the systematic increase in KE over longer times.

Physical space profiles of potential temperature, velocity variances, and heat flux are computed following the dry results (Figure 3.21). In addition we also compute the cloud cover fraction, total mixing ratio, and liquid water mixing ratio as shown in Figure 3.22. All of these results are consistent with [22, 1], however the addition of water vapour results in significant differences from the purely dry experiments. Firstly, while the profiles shown in Figure 3.21 generally match the qualitative features of the dry experiments (Figure 3.2) within the surface layer and mixing layer, there does appear to be an entirely new region between the mixing layer and stable layer, which we call the cloud forming region. This region appears to occupy a rather extended depth from around 500 m all the way up to 1800 m, although cloud formation is most active between 700 m and 1300 m. Despite averaging, there exists rather significant variation in
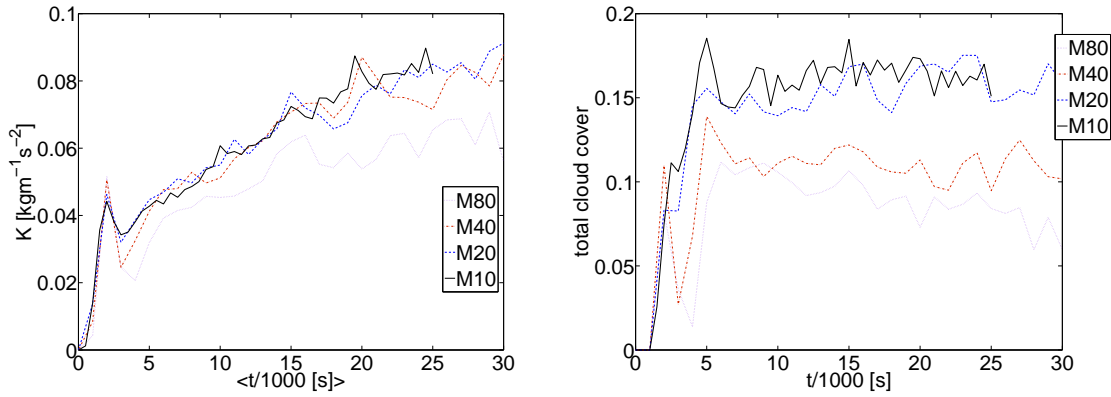
70

Figure 3.20: (a) Time series of volume mean kinetic energy for experiments M80-M10. (b) Time series of total cloud cover for experiments M80-M10.

the profiles between successive resolutions. In fact, it appears that the most variation between resolutions is seen within this cloud forming region in all profiles except the temperature and total mixing ratio. Based on the time series of cloud cover (Figure 3.20) and the plots of cloud fraction and liquid water mixing ratio (Figure 3.22), it appears that increased resolution results in more clouds forming. This generally seems to correspond to increased horizontal and vertical velocity variances where clouds are present. The fact that the physical space profiles have not converged with increasing resolution in regions where clouds form is not surprising because these clouds are not even close to being resolved. For example, looking at horizontal slices of the liquid water mixing ratio shown in Figure 3.23, the clouds have a diameter at most 400 m and frequently may be under 100 m in diameter. This means that even for the 20 m grid spacings, a cloud contains at most $10 - 20$ grid points and frequently may contain only 5 grid points. It is also evident from the cloud cover fraction that increased resolution results in more clouds penetrating higher up into the atmosphere, examples of which can be seen in the vertical slices of liquid water mixing ratio in Figure 3.24.

The plot of buoyancy flux [1] versus height is shown in Figure 3.21. As previously noted, the cloud forming region between $600 - 1500$ m shows significant positive buoyancy flux. Remember that in the dry simulations (Figure 3.2) the heat flux became negative at the top of the mixing layer corresponding to entrainment and then became roughly zero as we moved up through the stable layer. Now with the addition of moisture we still get some negative entrainment buoyancy flux at the top of the boundary layer, but we then get a large increase in positive buoyancy flux above corresponding to cloud formation. This makes sense since cloud formation results from

---

[1]We no longer refer to this as heat flux as water vapour alone can result in buoyancy in addition to temperature.
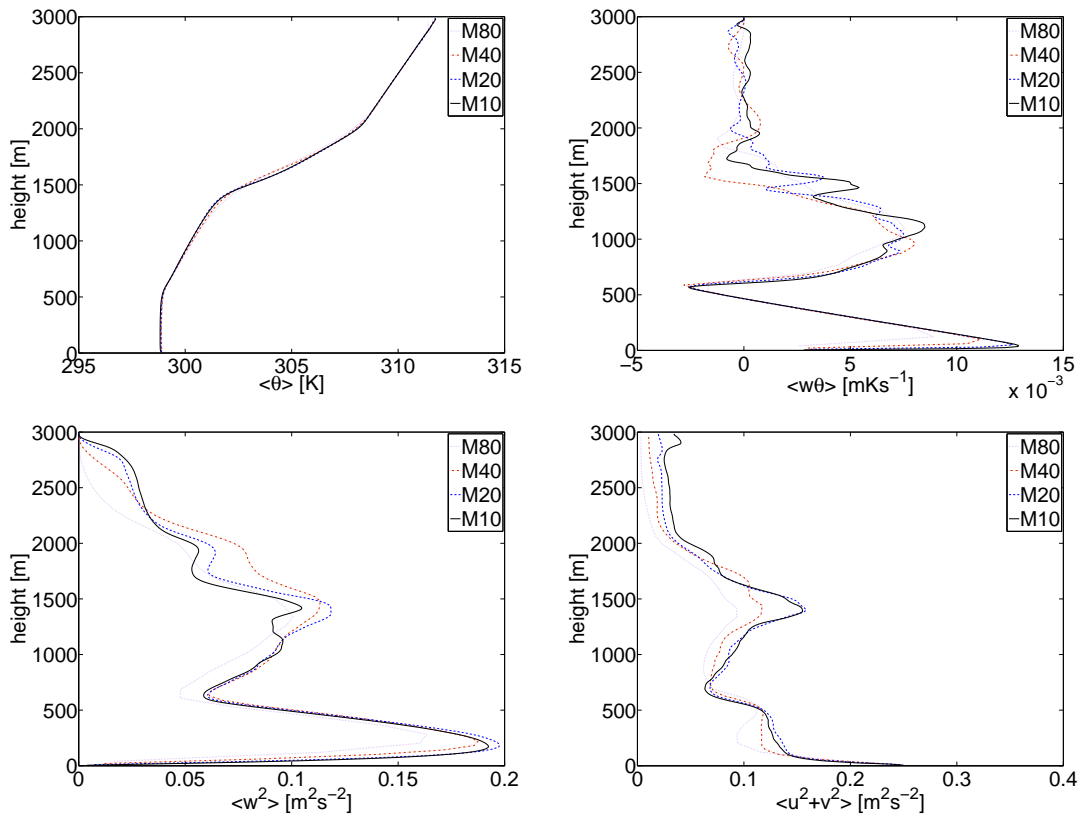
Figure 3.21: Horizontally and time averaged (a) potential temperature, (b) buoyancy flux, (c) vertical velocity variance, and (d) horizontal velocity variance for experiments M80-M10.
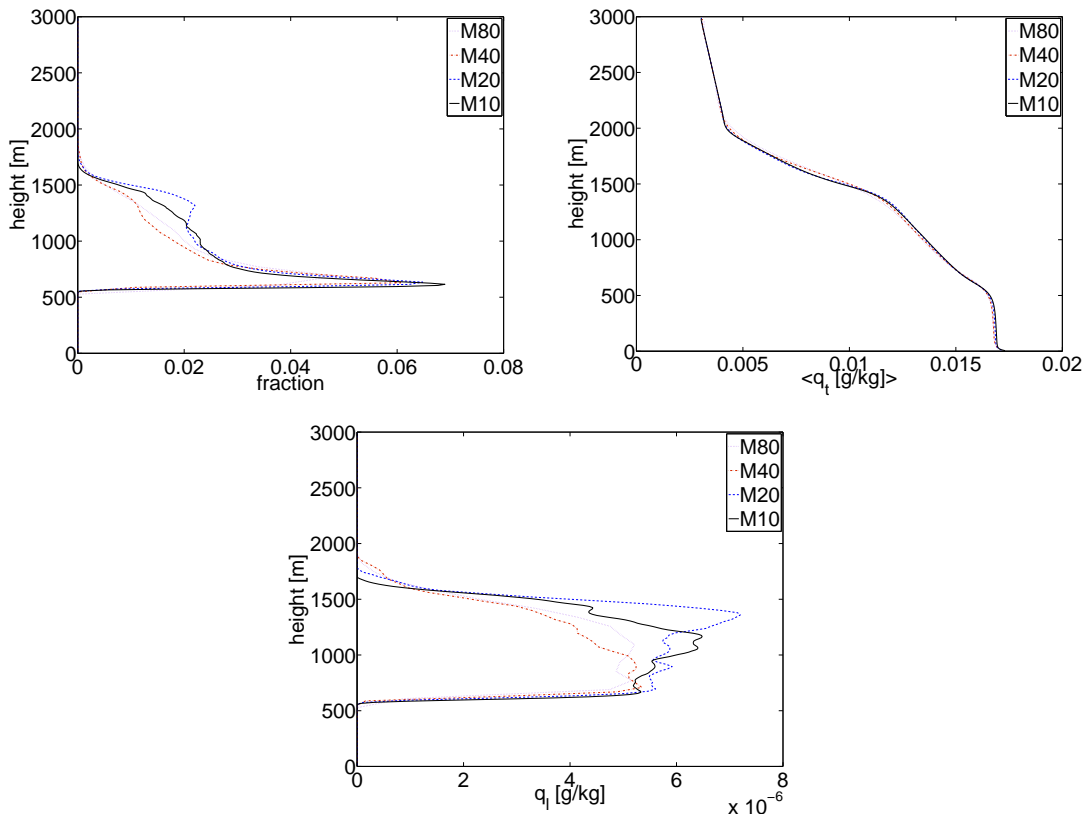
Figure 3.22: Horizontally and time averaged (a) Cloud cover fraction (liquid water mixing ratio), (b) Total mixing ratio, (c) liquid water mixing ratio for experiments M80-M10.
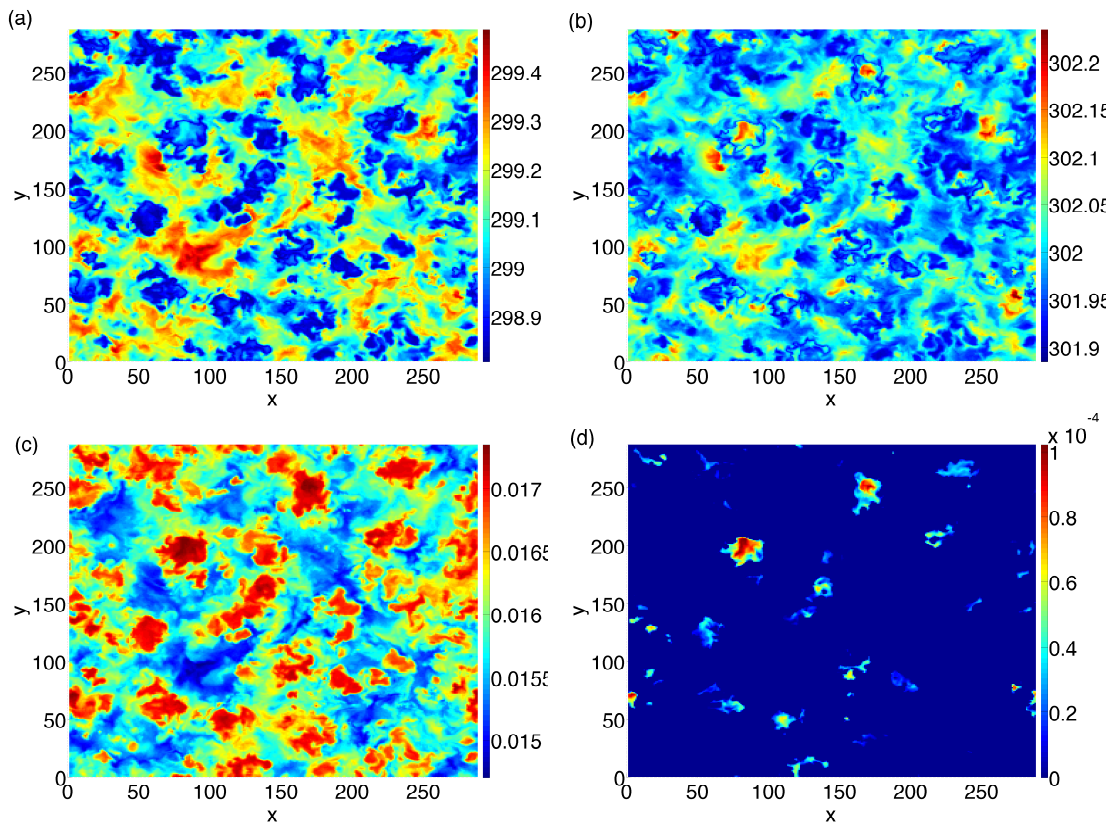
Figure 3.23: Horizontally and time averaged (a) potential temperature, (b) virtual potential temperature, (c) total mixing ratio, and (d) liquid water mixing ratio for experiment M10 at $z = 600$ m.

water vapour condensing into suspended liquid and this change of state from gas to liquid releases latent heat which then results in increased buoyancy. We underscore here that this source of buoyancy flux is significant. In fact looking at the buoyancy flux plot in Figure 3.21 the peak positive buoyancy flux within the cloud forming region is only surpassed near the ground. Thus cloud formation can be an important source of buoyancy flux, comparable to the heating from the ground, in the convective boundary layer.

Figure 3.24: Vertical (*x-z*) slices of (a) θ_v, (b) q_l, taken at time 25000 s for experiment M10.

3.2.2   Spectral Budget

Buoyancy Flux

The buoyancy flux spectra are shown at different vertical levels in Figure 3.25. We can see that like the dry simulations, the buoyancy flux peaks at small 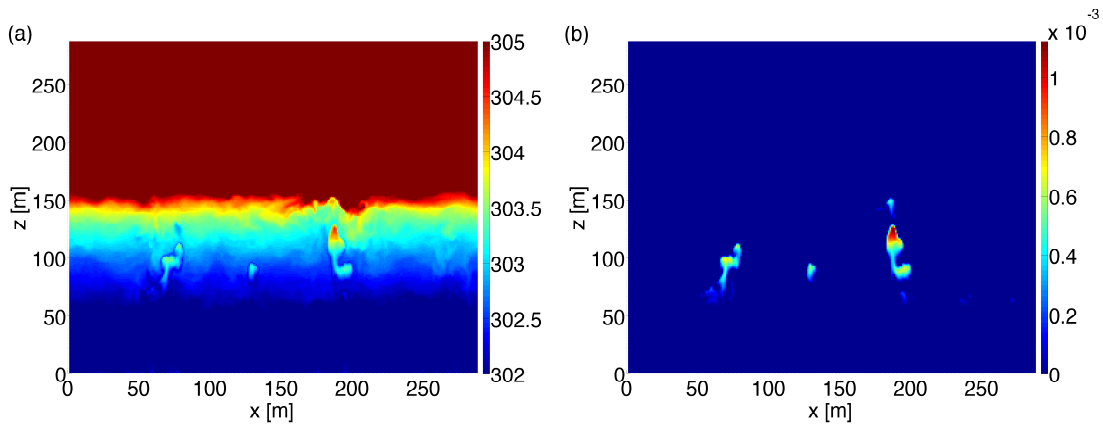scales at the surface and then rapidly moves to large scales as we move up through the mixing layer. At the top of the mixing layer a transition to negative flux corresponding to entrainment occurs. Unlike the dry experiments though, the formation of clouds results in a transition back to positive buoyancy flux. This is consistent with the physical space profiles shown in Figure 3.21. In Figure 3.26(a) we plot the domain averaged buoyancy flux and in Figure 3.26(b) the buoyancy flux restricted to the mixing layer ($200 - 500$ m) and cloud forming layer ($900 - 1200$ m). Similar to the dry experiments, the domain averaged spectra peaks at relatively large scales. The peak appears to remain approximately unchanged as resolution increases, consistent with the fact that the peak scales as the boundary layer depth, however energy is injected at increasingly smaller scales. It is clear that the buoyancy spectra within the cloud layer is shifted to smaller scales than the buoyancy spectra restricted to the mixing layer. This presumably corresponds to smaller eddies associated with the cloud formation than the eddies of the mixing layer, which scale as the boundary layer depth.

Transfer, Dissipation, & Pressure

The spectral kinetic energy budgets for experiments M80, M40, and M20, are shown in Figure 3.27. These budgets have a number of similarities to their dry counterparts. Firstly, we see that there is broad overlap between all terms. In fact this overlap is probably more pronounced
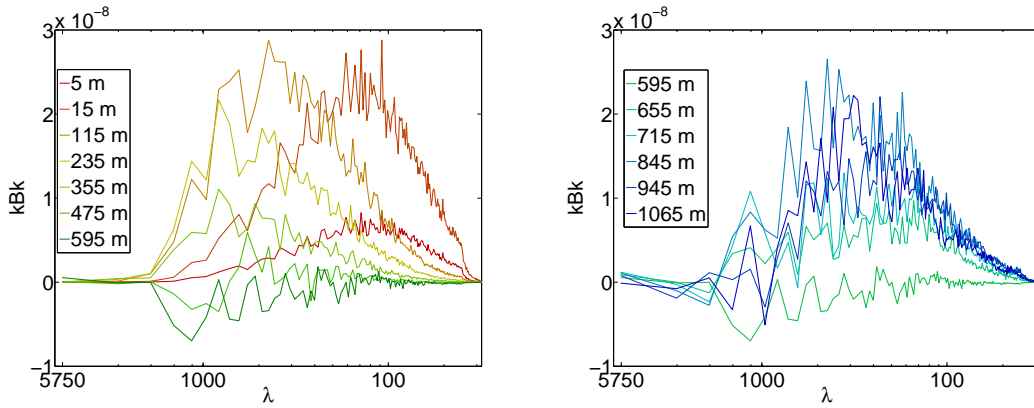
Figure 3.25: Time averaged horizontal buoyancy flux spectra at different height levels for run M10. Spectra have been multiplied by k_h to preserve area on the log-linear plot.

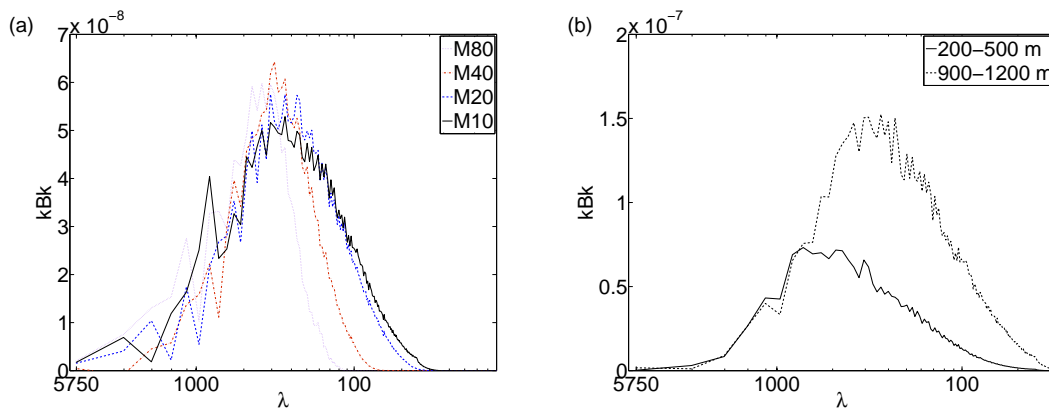Figure 3.26: (a) Time averaged buoyancy flux spectra averaged over the boundary layer depth for runs M80-M10. (b) Time averaged buoyancy flux spectra averaged over the mixing layer and cloud forming layer for run M10. Spectra have been multiplied by k_h to preserve area on the log-linear plot.

than what was seen in the dry runs. Secondly, the spectra are extended to smaller scales as resolution is increased. We see that at the largest scales (larger than the boundary layer depth) there is very little energy injection, transfer or dissipation. Thus we could have chosen a smaller domain and still captured the peak forcing. The magnitude of the dissipation spectrum is quite large, however appears to decrease as resolution is increased. There are a number of explanations for this. Firstly the coarser runs likely suffer from more pronounced errors associated with the interpolations and derivatives. This would show up strongest in the dissipation term as it is by far the most nonlinear of the budget terms. Secondly, the budget is not stationary, and in fact it is quite possible that the spectrum of dE_k/dt is not zero. We plot the energy spectra for experiments M80, M40, and M20 in Figure 3.28. It is interesting that the KE spectrum, particularly for the lowest resolution experiment M80, does scale as $-5/3$. Each successive experiment experiences less dissipation as can be seen in both Figures 3.27 and 3.28. As we move away from M80 to the finer grid spacing experiments M40 and M20, the scaling of the KE spectrum becomes less clear. In fact moving along the wavenumber axis, the slope appears to first be shallower then $-5/3$ and then becomes steeper than $-5/3$ as we move to where the dissipation is strongest. This is not surprising since all the budgets have such broad overlap between the transfer, buoyancy, and dissipation spectra. All of this evidence points to the need for experiments with significantly increased resolution. This was noted as being important for the dry experiments, but it is likely even more crucial for the cloud experiments which can have significant forcing at scales even smaller than the dry experiments because of latent heating from clouds.
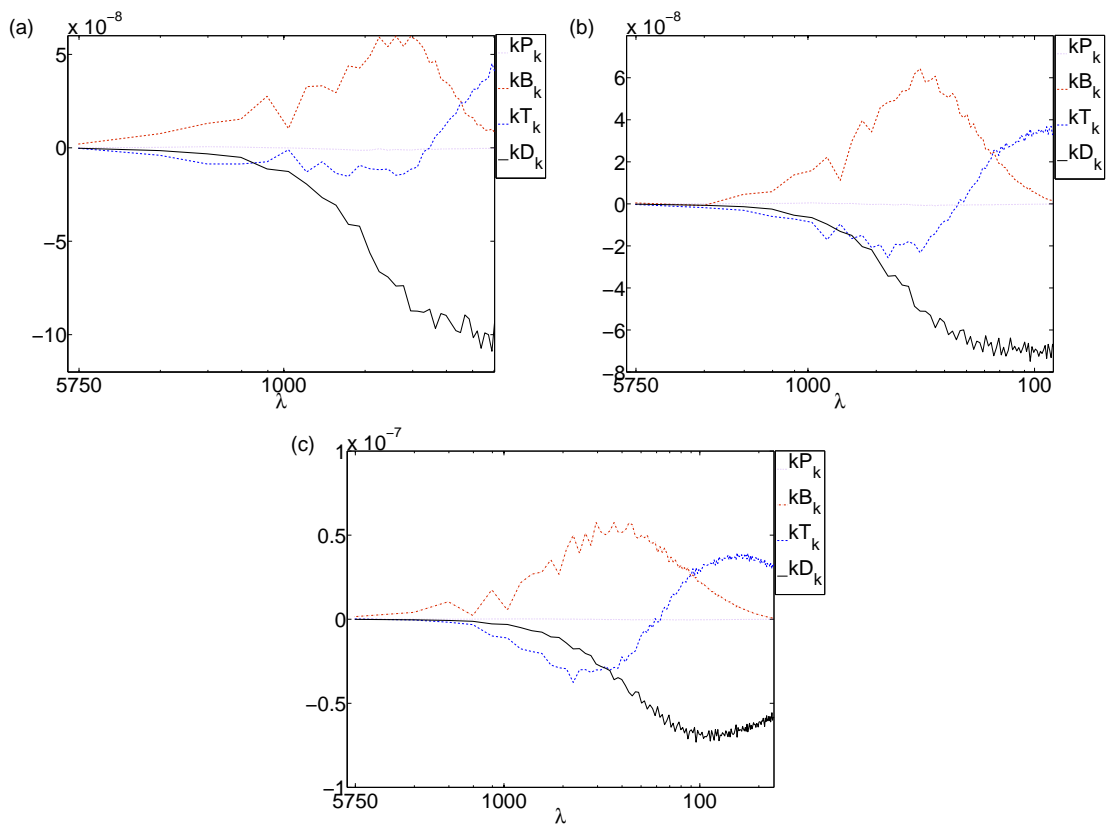
Figure 3.27: Time averaged terms in the spectral KE budget, averaged in z over the boundary layer depth, for runs (a) M80, (b) M40, and (c) M20.
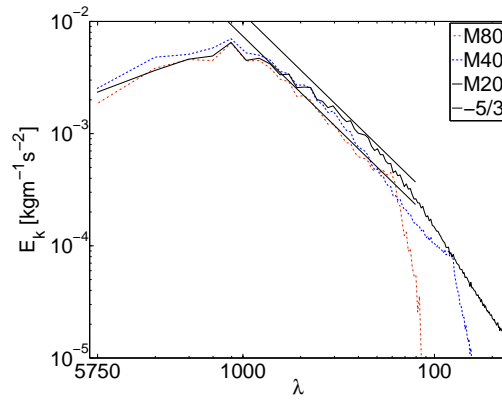
Figure 3.28: Time averaged KE spectra, averaged in z over the depth of the boundary layer for M80, M40, and M20.

Chapter 4

Conclusions

"If at first you don't succeed, try, try, again. Then
quit. No use being a damn fool about it."

—W. C. Fields

In this thesis we have presented large-eddy simulations of both the dry and moist convective
boundary layer. The physical space statistics of the simulations are in good agreement with other
recent high-resolution CBL studies, i.e. [24, 68, 27] for dry CBL and [22, 1] for moist. The
main contribution of this work is the calculation and analysis of the full spectral kinetic energy
budget, which provides insight into the shape of the horizontal wavenumber KE spectrum. KE is
injected via heat flux, the spectrum of which is peaked at large horizontal scales when integrated
over the depth of the boundary layer. At large scales, the heat flux spectrum is balanced by
the nonlinear transfer, which transfers energy to small scales where it is removed by the SGS
dissipation. Increasing the surface heat flux leads to a larger injection of KE and therefore a
stronger cascade to small scales. The domain size of 6 km seems sufficiently large to capture this
cascade; the budget terms are robust to increases in the domain size.

While the convective boundary layer setup does not conform to a traditional triply periodic
isotropic turbulence simulation, boundary-layer and atmospheric turbulence researchers have at-
tempted to explain some of the characteristics of CBL flows using classical turbulence theories
[51, 54, 64]. At first glance, the spectral budget seems to agree with this classic picture of three-
dimensional turbulence with large-scale forcing and small-scale dissipation. However, this inter-
pretation is complicated somewhat by the fact that the heat flux spectrum, which plays the role
of the KE forcing, is quite broad. Indeed, while the heat flux is peaked at scales of around 1 km,
there is a significant injection of kinetic energy from smaller scales that emerges as the resolution

increases. This small-scale heat flux is dominated by small eddies in the surface layer. Indeed, the integrated heat flux spectrum – i.e. the total injection rate of KE – only begins to converge for the dry experiments with very fine grid spacings of $\Delta x = 5$ m. As a result, there is a significant degree of overlap of the heat flux and dissipation spectra, even in the highest-resolution experiments. This overlap raises doubts about the possibility of an inertial range in these simulations. Our suspicions here were confirmed by analysis of the spectral flux. Rather than a wavenumber range of constant spectral flux, which is expected for isotropic three-dimensional turbulence, we find that the flux is peaked at increasingly small scales as the resolution increases.

The kinetic energy spectra for the dry experiments are consistently slightly shallower than what would be expected for isotropic three-dimensional turbulence, with spectral slopes closer to -4/3 rather than -5/3. This discrepancy with the classical theory is not surprising given the overlap between the forcing and dissipation spectra. It seems that the broad heat flux spectrum is injecting energy directly at intermediate and small scales, yielding a shallower energy spectrum than would otherwise be expected with purely large-scale forcing. Local isotropy was investigated by considering the ratio of the vertical and horizontal two-dimensional kinetic energy spectra, which gives a necessary condition for local isotropy. This ratio is larger than the theoretical value of 0.57 for isotropic turbulence, but seems to be approaching 0.57 at the smallest scales in the highest-resolution case of the dry CBL. As a result, grid spacings of $\Delta x = 5$ m seem to be almost sufficient to result in ratios that match the theoretical value. This provides some evidence that higher resolution experiments might result in regions of local small-scale isotropy around scales of 5 m or less.

Overall, using the TKE parameterization resulted in dissipation spectra more restricted to small scales, i.e. peak was shifted further to small scales compared to the Smagorinsky model for a fixed resolution. The heat flux spectra however continued to inject energy at a broad range of wavenumbers and the transfer spectra did not show any range of constant spectral flux. Both of these results are consistent with the Smagorinsky model results. It is difficult to say whether the TKE model was more computationally efficient in terms of moving the dissipation spectra to small scales as compared with the Smagorinsky model since the TKE model required an additional equation for e to be integrated and thus naturally took longer to run. Precise timing results are not available because dedicated nodes were not used.

The moist experiments were shown to have many similarities with their dry counterparts. In particular, the moist budgets showed broad overlap between the forcing, transfer, and dissipation. Like the dry experiments, the buoyancy spectra peaked a relatively large scales for all resolutions, but was also found to inject energy at increasingly smaller scales as resolution was increased. Significant differences between the dry and moist experiments were found however. With the addition of water vapour, the moist runs showed a significant source of buoyancy flux above the entrainment zone corresponding to the formation of clouds which release latent heat

during condensation. This cloud cover was shown to increase with resolution. In comparing the buoyancy flux within the mixing layer and the cloud forming layer, it was shown that buoyancy associated with cloud formation peaks at smaller scales than buoyancy associated with surface heating.

Despite the simple set-up, there remain a number of avenues for future work on this problem. First, it would be interesting to see whether higher resolution would yield an inertial range and a -5/3 spectrum at very small scales. Second, this work employs the Smagorinsky-Lilly SGS model (and some preliminary work with the TKE model), which is quite dissipative. Another choice of model, such as the dynamic Smagorinsky model [47], [30], might yield a wider range of undamped scales. Finally, it would be of significant interest to run moisture experiments with greatly increased resolution as clouds in the current study are clearly under-resolved. Further work incorporating precipitation would also be of interest.

References

[1] K-M. Xu A. Cheng and B. Stevens. Effects of resolution on the simulation of boundary-layer clouds and the partition of kinetic energy to subgrid scales. *Journal of Advances in Modeling Earth Systems*, 2010.

[2] U. M. Ascher. Numerical methods for evolutionary differential equations. *SIAM*, 2008.

[3] C-H Moeng B. Stevens and P. Sullivan. Entrainment and subgrid lengthscales in large-eddy simulations of atmospheric boundary-layer flows. *Proceedings of the IUTAM Symposium on Developments in Geophysical Turbulence*, 2000.

[4] C-H. Moeng B. Stevens and P. P. Sullivan. Large-eddy simulations of radiatively driven convection: Sensitivities to the representation of small scales. *J. Atmos. Sci*, 56, 1999.

[5] G. K. Batchelor. Small-scale variation of convected quantities like temperature in turbulent fluid part 1: General discussion and the case of small conductivity. *J. Fluid Mech.*, 5, 1959.

[6] G. K. Batchelor. Small-scale variation of convected quantities like temperature in turbulent fluid part 2: The case of large conductivity. *J. Fluid Mech.*, 5, 1959.

[7] G. K. Batchelor. An introduction to fluid dynamics. *Cambridge University Press*, 2000.

[8] J. A. Businger. Turbulent transfer in the atmosphere surface layer. *Workshop on Micrometeorology*, 1973.

[9] S. J. Caughey and S. G. Palmer. Some aspects of turbulence through the depth of the convective boundary layer. *Quart. J. R. Met. Soc*, 105, 1979.

[10] A. J. Chorin. Numerical solution of the navier-stokes equations. *Math. Comp.*, 22, 1968.

[11] P. A. Davidson. Turbulence: An introduction for scientists and engineers. *Oxford University Press*, 2004.

[12] S. M. de Bruyn Kops. Classical turbulence scaling and intermittency in stably stratified boussinesq turbulence. *J. Fluid Mech. (submitted)*, 2014.

[13] J. W. Deardorff. On the magnitude of the subgrid scale eddy coefficient. *J. Comp Phys*, 7, 1971.

[14] J. W. Deardorff. Numerical investigation of neutral and unstable planetary boundary layers. *J. Atmos. Sci*, 29, 1972.

[15] J. W. Deardorff. The use of subgrid transport equations in a three-dimensional model of atmospheric turbulence. *J. Fluids Eng*, 95, 1973.

[16] J. W. Deardorff. Three dimensional numerical study of turbulence in an entraining mixed layer. *Bound-Layer Meteor*, 7, 1974.

[17] J. W. Deardorff. Stratocumulus-capped mixed layers derived from a three-dimensional model. *Bound-Layer Meteor*, 18, 1980.

[18] J. W. Deardorff and G. E. Willis. Further results from a laboratory model of the convective planetary boundary layer. *Boundary-Layer Meteor*, 32, 1985.

[19] R. V. Driel and H. J. J. Jonker. Convective boundary layers driven by nonstationary surface heat fluxes. *J. Atmos. Sci*, 60, 2011.

[20] D. R. Durran. Numerical methods for fluid dynamics: With applications to geophysics 2nd edition. *Springer*, 2010.

[21] K. A. Emanuel. Atmospheric convection. *Oxford University Press*, 1994.

[22] A. P. Siebesma et. al. A large eddy simulation intercomparison study of shallow cumulus convection. *J. Atmos. Sci*, 60, 2002.

[23] C-H. Moeng F. T. M. Niewstadt, P. J. Mason and U. Schumann. Large-eddy simulation of the convective boundary layer: A comparison of four computer codes. *Durst et al. (eds.), Turbulent Shear Flows*, 8, 1993.

[24] E. Fedorovich. Entrainment into sheared convective boundary layers as predicted by different large eddy simulation codes. *Preprints, 16th Symp. on Boundary Layers and Turbulence, Portland, ME, Amer. Meteor. Soc*, 2004.

[25] U. Frisch. Turbulence. *Cambridge University Press*, 1995.

[26] G. J. Shutts G. K. Vallis and M. E. B. Gray. Balanced mesoscale motion and stratified turbulence forced by convection. *Q. J. R. Meteor. Soc*, 123, 1996.

[27] J. A. Gibbs and E. Fedorovich. Comparison of convective boundary layer velocity spectra retrieved from large-eddy-simulation and weather research and forecasting model data. *J. Atmos. Sci*, 53, 2014.

[28] R. J. Grossman. An analysis of vertical velocity spectra obtained in the bomex fair-weather, trade-wind boundary layer. *Boundary-Layer Meteor*, 23, 1982.

[29] P. G. Duynkerke H. J. J. Jonker and J. W. M. Cuijpers. Mesoscale fluctuations in scalars generated by boundary layer convection. *J. Atmos. Sci*, 56, 1999.

[30] B. Stevens H-Y. Huang and S. A. Margulis. Application of dynamic subgrid-scale models for large-eddy simulation of the daytime convective boundary layer over heterogeneous surfaces. *Bound-Layer Meteor*, 2008.

[31] Y. Izumi. Kansas 1968 field program data report. *Enviromental Research Papers No 369*, 1968.

[32] D. A. Haugen O. R. Cote Y. Izumi S. J. Caughey J. C. Kaimal, J. C. Wyngaard and C. J. Readings. Turbulence structure in the convective boundary layer. *J. Atmos. Sci*, 33, 1976.

[33] J. C. Kaimal and R. A. Eversole. Spectral characteristics of the convective boundary layer over uneven terrain. *J. Atmos. Sci*, 39, 1982.

[34] R. Kaiser and E. Fedorovich. Turbulence spectra and dissipation rates in a wind tunnel model of the atmospheric convective boundary layer. *J. Atmos. Sci*, 55, 1998.

[35] Y. Kaneda and T. Ishihara. High-resolution direct numerical simulation of turbulence. *Journal of Turbulence*, 7, 2006.

[36] A. N. Kolmogorov. The local structure of turbulence in incompressible viscous fluid for very larges reynolds numbers. *Dokl. Akad. Nauk SSSR*, 30, 1941.

[37] A. N. Kolmogorov. On degeneration of isotropic turbulence in an incompressible viscous liquid. *Dokl. Akad. Nauk SSSR*, 31, 1941.

[38] A. N. Kolmogorov. A refinement of previous hypotheses concerning the local structure of turbulence in a viscous incompressible fluid at high reynolds number. *J. Fluid. Mech.*, 12, 1962.

[39] J. N. Koshyk and K. Hamilton. The horizontal kinetic energy spectrum and spectral budget simulated by a high-resolution troposphere-stratosphere-mesoshpere gcm. *J. Atmos. Sci*, 58, 2001.

[40] P. K. Kundu and I. M. Cohen. Fluid mechanics 4th ed. *Academic Press*, 2008.

[41] L. Wittmeyer-Koch L. Elden and H. B. Nielsen. Introduction to numerical computation: Analysis and matlab illustrations. *Studentlitteratur*, 2004.

[42] D. H. Lenschow. Airplane measurements of planetary boundary layer structure. *J. Appl. Meteor*, 9, 1970.

[43] M. Lesieur. Turbulence in fluids. *Kluwer Academic Publishers*, 1990.

[44] R. J. Leveque. Finte volume methods for hyperbolic problems. *Cambridge University Press*, 2002.

[45] D. K. Lilly. On the numerical simulation of buoyant convection. *Tellus*, 14, 1962.

[46] D. K. Lilly. The representation of small-scale turbulence in numerical simulation experiments. *Proc. IBM Scientific Computing Symp on Environmental Sciences*, 1967.

[47] D. E. Stevens M. P. Kirkpatrick, A. S. Ackerman and N. N. Mansour. On the application of the dynamic smagorinsky model to large-eddy simulations of the cloud-topped atmospheric boundary layer. *J. Atmos. Sci*, 63, 2006.

[48] P. J. Mason. Large-eddy simulation of the convective atmospheric boundary layer. *J. Atmos. Sci*, 46, 1989.

[49] P. J. Mason and A. R. Brown. On subgrid models and filter operations in large eddy simulations. *J. Atmos. Sci*, 56, 1999.

[50] J. M. McDonough. Introductory lectures on turbulence: physics, mathematics, and modeling. *Departments of Mechanical Engineering and Mathematics, University of Kentucky*, 2007.

[51] P. Mestayer. Local isotropy and anisotropy in a high-reynolds-number turbulent boundary layer. *J. Fluid Mech*, 125, 1982.

[52] C-H. Moeng. A large-eddy simulation model for the study of planetary boundary-layer turbulence. *J. Atmos. Sci*, 41, 1984.

[53] C-H. Moeng and P. P. Sullivan. A comparison of shear and buoyancy driven planetary boundary layer flows. *J. Atmos. Sci*, 51, 1994.

[54] C-H. Moeng and J. C. Wyngaard. Spectral analysis of large-eddy simulations of the convective boundary layer. *J. Atmos. Sci*, 45, 1988.

[55] Y. Ogura and N. A. Phillips. Scale analysis of deep and shallow convection in the atmosphere. *J. Atmos. Sci.*, 19, 1962.

[56] C-H. Moeng P. P. Sullivan, J. C. McWilliams. A subgrid-scale model for large-eddy simulation of planetary boundary-layer flows. *Boundary-Layer Meteor*, 71, 1994.

[57] S. B. Pope. Turbulent flows. *Cambridge University Press*, 2000.

[58] Z. A. Prandtl. Bericht uber untersuchugen zur ausgebildeten turbulenz. *Zs. Angew. Math. Mech.*, 5, 1925.

[59] D. Randall. The anelastic and boussinesq approximations. *Quick Studies in Atmospheric Sciences*, 2013.

[60] L. F. Richardson. Weather prediction by numerical process. *Cambridge, The University Press*, 1922.

[61] R. R. Rogers and M. K. Yau. A short course in cloud physics 3rd ed. *Pergamon Press*, 1989.

[62] P. G. Duynkerke S. R. De Roode and H. J. J. Jonker. Large-eddy simulation: how large is large enough? *J. Atmos. Sci*, 61, 2004.

[63] J. Sandham and M. L. Waite. Spectral energy balance in dry convective boundary layers. *Journal of Turbulence. (submitted)*, 2014.

[64] H. Schmidt and U. Schumann. Coherent structure of the convective boundary layer derived from large-eddy simulations. *J. Fluid Mech*, 200, 1989.

[65] J. Smagorinsky. General circulation experiments with the primitive equations. *Monthly Weather Review*, 91, 1963.

[66] J. M. Straka. Cloud and precipitation microphysics: Principles and parameterizations. *Cambridge University Press*, 2009.

[67] R. B. Stull. An introduction to boundary layer meteorology. *Springer*, 2009.

[68] P. P. Sullivan and E. G. Patton. The effect of mesh resolution on convective boundary layer statistics and structures generated by large-eddy simulation. *J. Atmos. Sci*, 68, 2011.

[69] T. Takemi and R. Rotunno. The effects of subgrid model mixing and numerical filtering in simulations of mesoscale cloud systems. *Monthly Weather Review*, 131, 2003.

[70] G. I. Taylor. The spectrum of turbulence. *Proc. R. Soc. Lond.*, 164, 1938.

[71] G. K. Vallis. Atmospheric and ocean fluid dynamics. fundamentals and large-scale circulation. *Cambridge University Press*, 2006.

[72] T. von Karman. Some remarks on the statistical theory of turbulence. *Proc. 5th Int. Congr. Appl. Mech. Cambridge*, 1938.

[73] M. L. Waite and C. Snyder. The mesoscale kinetic energy spectrum of a baroclinic life cycle. *J. Atmos. Sci*, 66, 2009.

[74] J. M. Wallace and P. V. Hobbs. Atmospheric science: An introductory survey. *Academic Press*, 1977.

[75] J. C. Wyngaard. Turbulence in the atmosphere. *Cambridge University Press*, 2010.

[76] M. J. Molemaker X. Capet, J. C. McWilliams and A. F. Shchepetkin. Mesoscale to sub-mesoscale transition in the california current system. part iii: Energy balance and flux. *J. Phys. Ocean*, 38, 2008.